



# TECHNICAL JOURNAL

Engineering excellence  
around the globe

Volume 5 | Issue 1 | 2023







## CHRIS HENDY

Editor-in-Chief SNC-Lavalin  
Technical Journal

Atkins Fellow, Professional  
Head of Bridge Engineering  
and Transportation  
Technical Director,  
Engineering Services

## Foreword

Welcome to the ninth edition of our SNC-Lavalin Technical Journal, established to showcase the fantastic depth and breadth of our engineering expertise across a wide range of disciplines and domains and to demonstrate that technical excellence is at the heart of everything we do. This edition highlights the impressive work we have been doing reducing the carbon impact of new and existing infrastructure, whilst adapting and designing for climate resilience.

In designing for climate resilience, we have driven improvements to the assessment of hydroplaning risk for North Carolina Department of Transportation to allow designers to better quantify and manage the risk associated with wide section roadways. We have derived more accurate prediction methods to determine lake levels for both long-term and short-term extreme values for flood and drought conditions, which can be applied to nearly any region globally. We have developed a hydrologic modeling guidance document for NEOM, a planned independent economic zone in Northwest Saudi Arabia with a vision to be the land of the future, with application to other arid areas of the world with limited rainfall data. And we have produced an optimised, resilient and climate-proof solution to address lateral erosion of the River Towy which was threatening the stability of the A40 trunk road in Carmarthenshire, Wales.

In designing to minimise cost and carbon throughout the asset lifecycle, we have optimised the M&E design of new road tunnels through a systematic identification and consideration of the key influencing factors. We have also carried out analysis of jet fan inlet temperatures for two major underground transit projects, highlighting the key considerations with respect to design fire size, active ventilation flow rates, slope of the tunnel and proximity to fire. We have established best practice in the assurance process for electromagnetic compatibility in the context of major rail projects, including application of the Atkins' Traction Modelling Simulator (ATMS) to the design and development of safe, reliable and efficient railways. And we have harnessed technological developments in 3D geophysical investigation methods to improve georesilience and understanding of geohazards, including using 3D electrical resistivity tomography to characterise potential karst features.

The above examples provide only a small insight into the wealth of innovation that SNC-Lavalin creates day to day.

I hope you enjoy the selection of technical papers included in this edition as much as we have enjoyed compiling them.



## Editor-in-chief

## 2023 Editorial Board Members



**Chris Hendy**

FREng MA (Cantab)  
CEng FICE Eur Ing  
Technical Director,  
Atkins Fellow, Professional  
Head of Bridge Engineering  
Engineering Services  
– Transportation UK  
Epsom, UK



**Ramy Azar**

PhD Ing.  
Vice-President, Engineering & Chief  
Technology Officer – Power Grids  
Engineering Services Canada  
– Power & Renewables  
Montreal, Canada



**Vinod Batta**

PhD P.Eng.  
Vice President & General Manager,  
Power Solutions – Western Canada  
Chief Technical Officer – Hydro  
Engineering Services Canada  
– Power & Renewables  
Vancouver, Canada



**Donna Huey**

GISP  
Atkins Fellow & Sr. Vice President,  
Chief Digital Officer  
Engineering Services USA  
– Business Development, Digital  
Orlando, FL, USA



**Tracey Radford**

BSc MSc CGeol FGS  
Practice Manager, Geotech  
Network Chair  
Engineering Services  
– Infrastructure UK  
Epsom, UK



**Dr. Santhosh Kumar M**

PhD CEng MIET  
Technical Director, GDC and Atkins  
Fellow of Digital  
Engineering Services – Global  
Technology Center  
Bangalore, India



**Roger Cruickshank**

BEng  
Senior Director, Strategic  
Transport Planning, Atkins Fellow  
Engineering, Design and  
Consultancy Services  
Engineering Services – Middle East  
Dubai, UAE

## Production Team



**Dorothy Gartner**

MLIS  
Librarian  
Project Performance  
and Risk Oversight  
Montreal, Canada



**Samantha Morley**

CAPM  
Project Controls Analyst I  
Engineering Services USA  
– Operational Services  
Omaha, NE, USA



**Cheryl Law**

MEng CEng MICE  
Associate Director  
Engineering Services  
– Infrastructure UK  
Epsom, UK



## 2023 Editorial Board Members



**Dr. Navil Shetty (Outgoing)**

PhD DIC FIAM

Atkins Fellow and Technical Chair  
for Asset Management

Leader, Centre of Excellence  
for Asset Management  
& Operations (AMOCE)

Bangalore, India



**Tim Milner (Outgoing)**

CSci CChem MRSC

Atkins Fellow and Chief  
Technology Officer

Nuclear

Columbia, SC, USA



**Mufeed Odeh**

PhD PE

Senior Technical Specialist

Engineering Services USA  
– Water TPO

Raleigh, NC, USA



**Jill Hayden**

PhD FIET

Technical Director, Atkins Fellow  
(Intelligent Mobility & Smart  
Technologies)

Engineering Services  
– Transportation UK

Manchester, UK



**Kan Pang**

BEng CEng

Senior Technical Director

Engineering  
Services Asia – Transportation

Hong Kong, China



**Samuel Fradd**

Technology Manager

Engineering Services  
– Transportation UK

Epsom, UK

### About the Cover

The arid landscape of the NEOM region, a planned independent economic zone in Northwest Saudi Arabia. Rainfall data, in the form of Intensity Duration Frequency (IDF) curves, were developed for this data scarce region.









# Contents

## Water Engineering

- |   |    |
|---|----|
| 01. Advancements to Hydroplaning Risk Assessment  | 9  |
| 02. Development of Rainfall Intensity Duration Frequency (IDF) Curves for the NEOM Region, Saudi Arabia | 33 |
| 03. Improving the Estimation of Non-Stationary Trends and Return Frequencies for Lake levels            | 59 |

## Tunnel Engineering

- |  |    |
|--|----|
| 04. Designing Accessible Inverts to Meet the Requirements of Tunnel Owners and Operators | 79 |
| 05. Jet Fan Temperature Rating Based on Fan Inlet Airflow Temperatures                   | 99 |

## Geotechnical Engineering

- |   |     |
|---|-----|
| 06. Protecting Critical Infrastructure through Georesilient Design: A Case Study from the A40 near Llanegwad  | 117 |
| 07. Perspectives on Practical Tools, Best Practice, and Emerging Technologies in the Application of Geophysics for Enhancing Resilience to Geohazards | 135 |

## Rail Engineering

- |   |     |
|---|-----|
| 08. Electromagnetic Compatibility Integration on Major Railway Projects | 153 |
|---|-----|







**Rick Renna**  
Sr Engineer IV  
Engineering Services – USA (Water TPO)  
Tallahassee, FL, USA



**Katey Earp**  
Sr Engineer III  
Engineering Services – USA (Water TPO)  
Tallahassee, FL, USA



**Jeff Reck**  
Sr Engineer IV  
Engineering Services – USA (Water TPO)  
Raleigh, NC, USA



**Rebecca Purvis**  
Sr Engineer I  
Engineering Services – USA (Water TPO)  
Raleigh, NC, USA

## 01. Water Engineering

# Advancements to Hydroplaning Risk Assessment

### Abstract

A cost-effective design preference for widening roadway sections is to expand lanes to the outside with a continuous cross slope, rather than expand and slope lanes to the inside. The resulting wider roadways increase the water film thickness along the cross slope and often raise concern regarding vehicle hydroplaning potential.

The NCDOT Hydraulics Unit employed ATKINS to renovate their approach to managing hydroplaning risk adding robust, new policy language to identify concerns early in the project design process, identify mitigation strategies, and develop a new hydroplaning assessment computer program to better predict hydroplaning potential. Program improvements include a computationally averaged water film thickness approach, regionally specific pavement types, an adjustment for modern tire pressure, a factor to assess the maximum water film thickness in superelevation transitions, and a modified application of the PAVDRN hydroplaning speed formula that adjusts to the specific mean texture depth and eliminates the effects of a formula computational discontinuity. These policy improvements allow designers to better quantify the risk associated with wide section roadways and decide when it would be beneficial to implement a mitigation strategy to decrease risk.

### KEYWORDS

Water film thickness; Hydroplaning; PAVDRN; Superelevation transitions; MPD.

## 1. Introduction

---

Hydroplaning is a major safety concern on highways around the world that will potentially be exacerbated by climate change and increased rainfall. Highways are often constructed or expanded along a continuous slope for constructability and cost. The resulting wider roadways increase the water film thickness along the cross slope, increasing vehicle hydroplaning potential.

The North Carolina Department of Transportation (NCDOT) Hydraulics Unit employed Atkins, a SNC-Lavalin company, to address the challenges with the current hydroplaning practice, develop a new hydroplaning assessment computer program to predict hydroplaning potential more accurately, and identify hydroplaning mitigation strategies. Atkins reviewed available hydroplaning research to evaluate and identify research results that could be developed into a robust, improved policy. During this effort, technical program improvements focused on three main advancements:

- › A modification of the PAVDRN hydroplaning speed formula that reflects the specific pavement mean texture depth and eliminates the effects of a formula computational discontinuity,
- › An adjustment for modern tire pressure and tread patterns, and
- › An approach to quantify the maximum water film thickness in superelevation transitions.

This article outlines the methodology that was employed to achieve the above advancements in hydroplaning design practice applicable to wide section roadways.



## 2. Adjustment of PAVDRN HPS Equation to Eliminate Discontinuity at Transition Between Agrawal and Gallaway Equations

The PAVDRN HPS Equation, as developed by Huebner (1986) and shown below in **Equation 1**, is a combination of two separate equations: the Agrawal Equation and the Gallaway Equation:

$$HPS = \begin{cases} 26.04 \cdot WFT^{-0.259} & \text{if } WFT < 0.094 \text{ in} \\ 3.09 \cdot \text{Max}\left(\frac{10.409}{WFT^{0.06}} + 3.507, \left[\frac{28.952}{WFT^{0.06}} - 7.817\right] \cdot MTD^{0.14}\right) & \text{if } WFT \geq 0.094 \text{ in} \end{cases}$$

(Equation 1)

Where,

HPS = Hydroplaning Speed (mph)

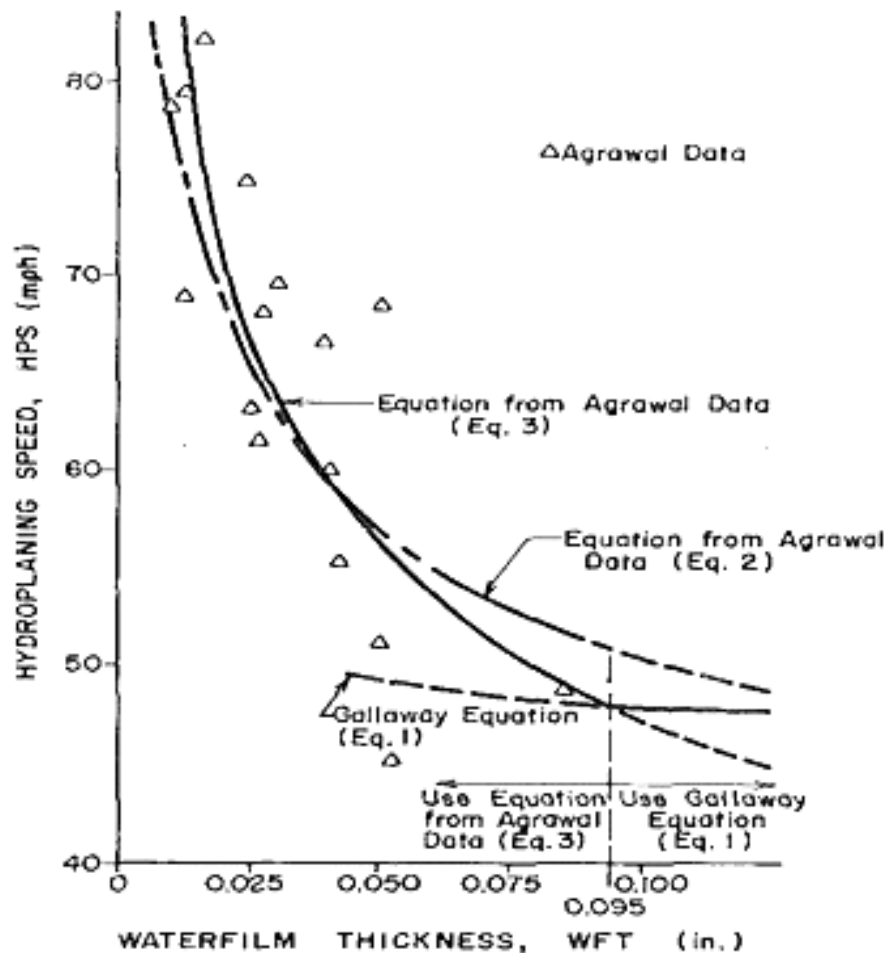
WFT = Water Film Thickness (in)

MTD = Mean Texture Depth (in)

The development of the PAVDRN HPS formula, in Huebner (1986), followed the Agrawal Equation until it intersected the Gallaway Equation, then followed the Gallaway Equation with increasing WFTs, as shown in Figure 1.

FIGURE 1

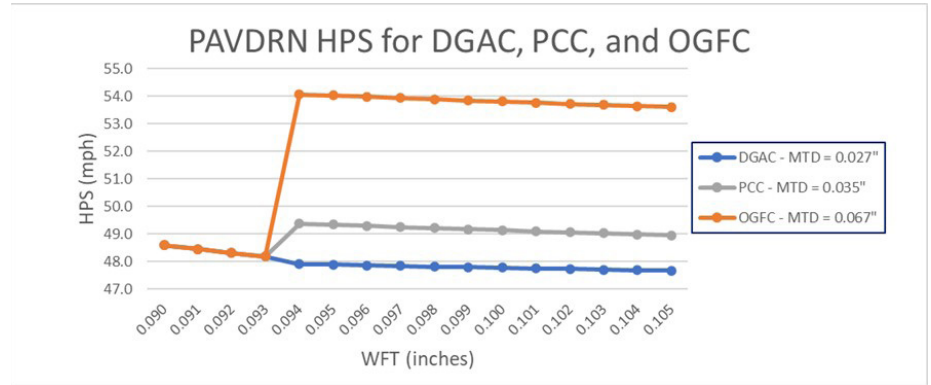
Confluence of Agrawal  
and Gallaway data  
from Huebner (1986)



At the intersection of these two equations, which occurs close to 0.094" WFT, the PAVDRN HPS equation gives inconsistent results, as shown in Figure 2 for three different pavement types: dense graded asphalt (DGAC), concrete (PCC), and open graded friction course (OGFC).

**FIGURE 2**

Water film thickness vs.  
hydroplaning speed for  
DGAC, PCC, and OGFC



From the graphs in **Figure 2**, the discontinuity, occurring at the boundary between the Agrawal and Gallaway equations, increases as the pavement MTD increases. Solving for the MTD at the common point between the Agrawal and Gallaway Equations at WFT = 0.95" (as cited by Huebner, 1986), yields an MTD of 0.028"; if one uses a WFT of 0.094" (2.4mm, as cited in the 1998 PAVDRN Report), the equations join at MTD=0.029". Thus, the PAVDRN Equation, in its current form, is accurate for only a single MTD defined by the constrained equation break at WFT = 0.094".

To allow for continuity in the HPS computational results for multiple MTDs, the PAVDRN Equation was modified (**Equation 2**), after the approach of Huebner (1986), to follow the Agrawal Equation until it intersects the Gallaway Equation at any feasible MTD, rather than forcing the change in equations to occur at WFT = 0.094".

$$HPS = \begin{cases} 26.04 \cdot WFT^{-0.259} & \text{if } WFT < 0.094 \text{ in} \\ 3.09 \cdot \text{Max} \left( \frac{10.409}{WFT^{0.06}} + 3.507, \left[ \frac{28.952}{WFT^{0.06}} - 7.817 \right] \cdot MTD^{0.14} \right) & \text{if } WFT \geq 0.094 \text{ in} \end{cases}$$

(Equation 2)

Where,

HPS = Hydroplaning Speed (mph)

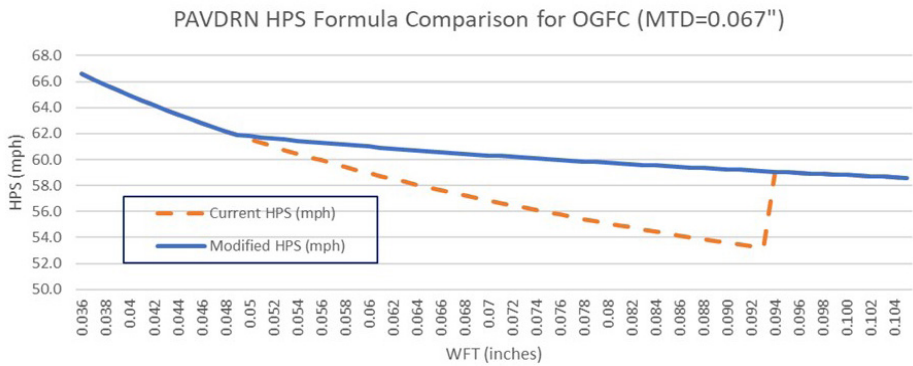
WFT = Water Film Thickness (in)

MTD = Mean Texture Depth (in)



Figure 3 shows a comparison between the current form of the PAVDRN Equation and the Modified PAVDRN Equation, as previously discussed, for OGFC.

**FIGURE 3**  
Comparison of current  
and modified PAVDRN  
equations for OGFC



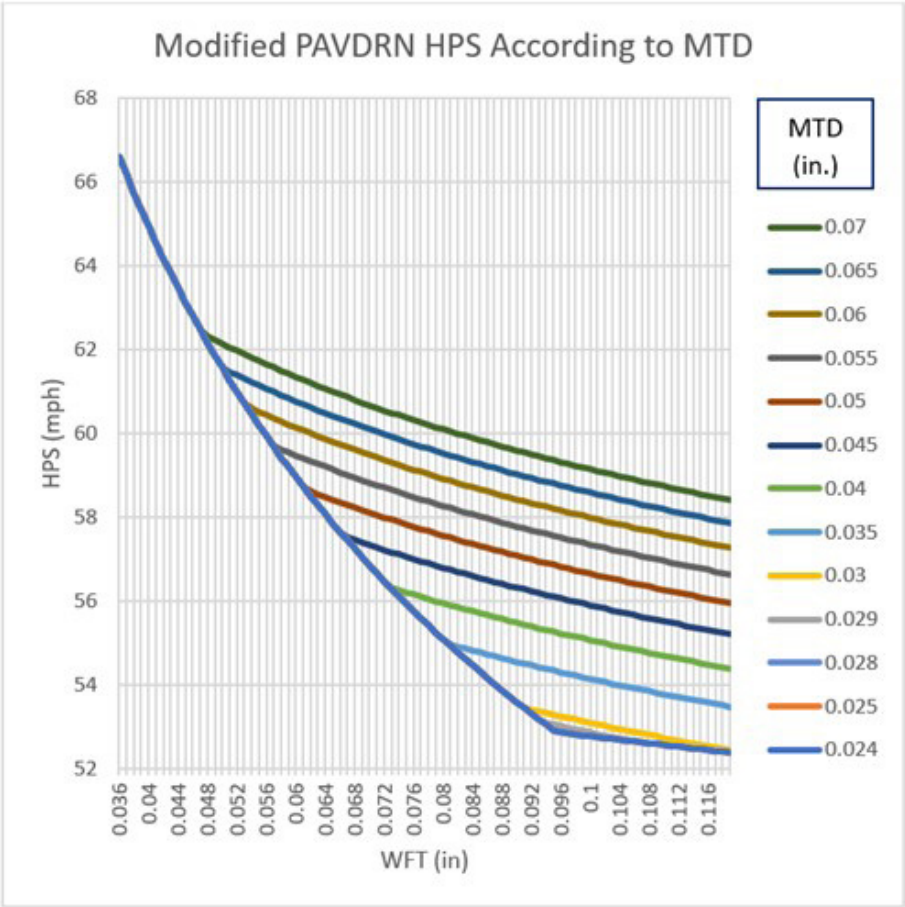
Note that the movement of the confluence of the two equations extends the usage of the Gallaway Equation into smaller WFTs. The Gallaway data covers this region, quoting Gallaway (1979), p. 128:

*“Rainfall rates were adjusted to produce water depths in the outside wheel path of the outside lane in the range of about 0.06in (1.5mm) above the asperity peaks to 0.05in (1.3mm) below the asperity peaks.”*

The resulting computations yield a family of curves with a moving transition point between the Agrawal and Gallaway portions of the equation, as shown in Figure 4.

FIGURE 4

Modified PAVDRN equation  
with varying MTDs



### 3. Predicted Hydroplaning Speed Adjustment for Modern Car Tire Pressure & Tread Patterns

---

This section outlines the justification for increasing the PAVDRN hydroplaning speed prediction by 5mph to account for modern target tire pressure standards and tread patterns.

#### 3.1 CHANGES IN MODERN TIRE PRESSURE TARGETS

In the late 1970s, when the physical hydroplaning testing was performed that was later used to develop the PAVDRN model, tire inflation was not monitored with dashboard warning alerts for low pressure. Since 2008, the National Highway Safety Administration (NHTSA) requires that the low tire pressure light indicator (LTPLI) must come on when the tire pressure drops 25% below the listed recommended inflation pressure. In practice, according to the American Automobile Association, NHTSA's requirement is well below a safe operating tire pressure. No data is readily available on the warning inflation targets used on modern cars. Though there are very few cars with target tire pressures of 29 or 30psi (such as some options of the 2017 Volkswagen Beetle, Type S), and from anecdotal experience, most modern cars alert the driver when tire pressure drops below 30psi. Therefore, assuming a tire inflation pressure of 29psi, a value measured in the available data, seems to be a reasonable target for expected user tire pressure maintenance on cars.

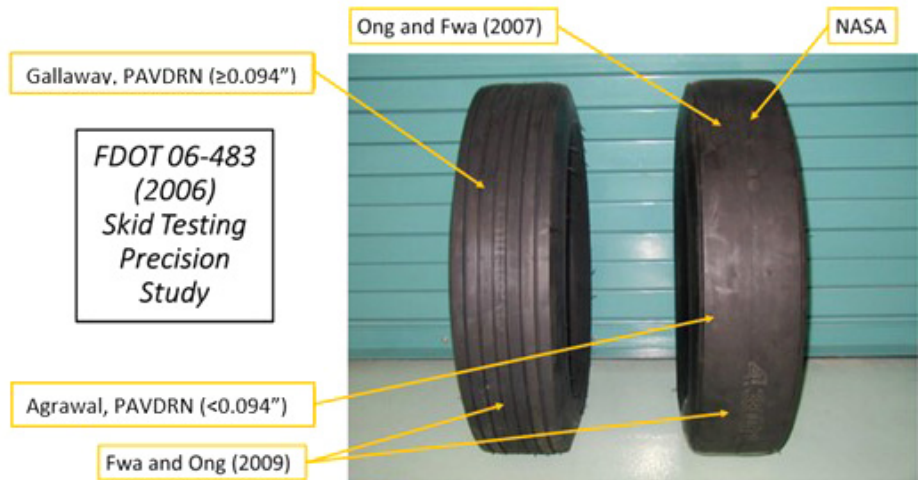
#### 3.2 PAVDRN BACKGROUND AND VALIDATION OF ONG & FWA (2007)

Several widely accepted hydroplaning formulas, including NASA, PAVDRN (via Gallaway testing), and Texas Department of Transportation (TXDOT) are empirical in nature and developed under specific experimental conditions, including the use of different standard ASTM tires. The current NCDOT hydroplaning potential assessment is based on PAVDRN, which does not consider the effect of tire pressure because testing was performed using ASTM E501 *ribbed* and ASTM E524 *smooth* tires, both of which use 24psi as the standard tire inflation pressure (**Figure 5**).



**FIGURE 5**

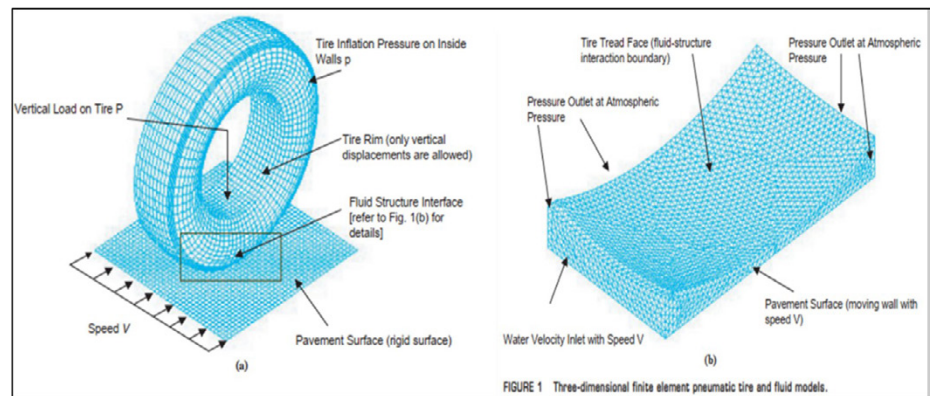
ASTM E501 Ribbed  
and ASTM E524  
smooth tires



The PAVDRN-predicted hydroplaning speed (HPS) algorithm is a combination of Agrawal (1977) data and Gallaway (1979) data, and was paired by Huebner (1986), as shown in **Figure 1**. Conversely, Ong and Fwa (2007) is based on a robust finite element model that considers the mechanics for relevant hydroplaning variables:

**FIGURE 6**

Diagram of FEM  
mesh used by Ong  
and Fwa (2007)



Based on the Ong and Fwa model, researchers at the University of South Florida (Gunaratne 2012) developed relationships between hydroplaning potential, tire inflation pressure, and Water Film Thickness (WFT) (**Equation 3**).

$$v_p = \frac{4.27 (P_t)^{0.5001}}{t_w^{0.06}} + 2.58 (P_t)^{0.4989}$$

(Equation 3)

Where,

$V_p$  = hydroplaning speed (km/hr)

$P_t$  = tire pressure (KPa)

$t_w$  = WFT (mm)

and ultimately, the following equation that included the vehicle wheel load:

$$V_p = (WL)^{0.2} (P_t)^{0.5} \left[ \frac{0.82}{t_w^{0.06}} + 0.49 \right]$$

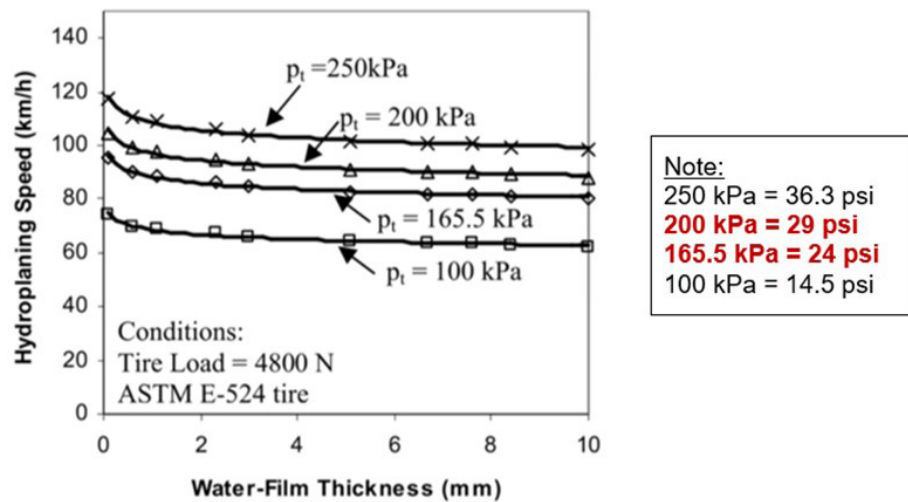
(Equation 4)

### 3.3 ONG & FWA (2007) FINDINGS ON TIRE PRESSURE

Ong & Fwa developed plots to isolate a specific variable and show the dependency of the hydroplaning speed. **Figure 7**, shows the variation of hydroplaning speed in relation to water film thickness (WFT) and tire inflation pressures.

**FIGURE 7**

From Ong and Fwa (2007b), the dependency of the hydroplaning speed on WFT and tire inflation pressure



The validation efforts performed by Gunaratne (USF) to confirm the Ong and Fwa (2007b) equation results to the NASA and PAVDRN equations provides confidence in using Ong and Fwa to quantify the effects of tire pressure on the predicted hydroplaning speed. Using Equation 3 from Gunaratne (2012), and targeting a responsible tire pressure of 29psi, the difference between 24psi and 29psi, using a WFT of 2mm, is 5.2mph. Using the work by Gunaratne, and targeting a responsible tire pressure of 29psi, the predicted hydroplaning speed of the PAVDRN equations may be increased by 5mph.

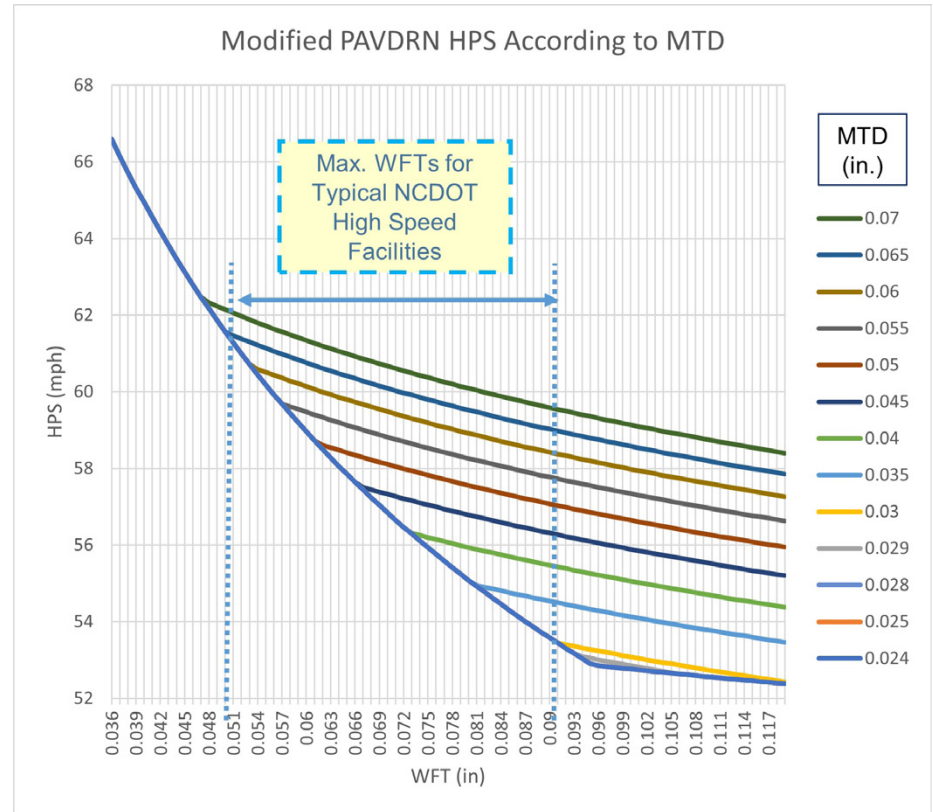


### 3.4 EFFECTS OF MODERN TIRE TREAD PATTERNS

The maximum WFTs for roadway sections fall within the range where PAVDRN utilizes the Gallaway data set, as shown in **Figure 8**, which is based on the ASTM E-501 (ribbed) tires.

**FIGURE 8**

Family of curves from modified PAVDRN equation



Tire tread patterns on modern tires are far superior to the E-501 treads (See **Figure 5**) in shedding pavement runoff, though no published testing is available to quantify their increased performance.

### 3.5 FWA AND ONG (2009) FINDINGS ON THE HPS BENEFITS OF PAVEMENT GROOVING

In 2009, Fwa and Ong published a research paper entitled, Relative Effectiveness of Grooves in Tire and Pavement in Reducing Vehicle Hydroplaning Risk, wherein they used their 2007 finite element model to examine the effects of both longitudinal and transverse grooves in both pavement and tires. They concluded that, "Overall, the analysis shows that transverse grooves perform better than longitudinal grooves in raising hydroplaning speed (i.e., reducing hydroplaning risk), and that pavement grooving is a more effective measure than grooving tire tread in reducing hydroplaning risk."

Fwa and Ong conducted their studies based on the following:

- › ASTM E 501 Ribbed tire (inflated to 27psi and with a constant wheel load of 2.41kN)
- › WFT of 7.62mm (0.3 inch)
- › Grooves – 5.08mm wide @ 21.8mm center-to-center spacing, depths 0, 2.0, 5.0, 9.8mm

Two tire-road conditions occur in typical roadway design that are important to quantify from the Fwa and Ong study:

- › Condition 1: Longitudinally grooved tires on non-grooved pavement.
- › Common car tire tread patterns are longitudinal grooves, 2/32 inch (1.6mm) deep.
- › Condition 2: Longitudinally grooved tires on transversely grooved pavement.
- › NCDOT Specification Article 420-14 requires concrete bridge decks be rectangular grooves 1/8 inch-wide and 3/16 inch (4.76mm) deep, with grooves spaced 3/4 inch center to center.

Noting that the 0mm groove depth is the smooth condition, hydroplaning speeds for the above conditions can be interpolated (highlighted in italics) from **Table 1** in Fwa and Ong's 2009 research results.

**TABLE 1**

Data from Fwa and Ong (2009) for hydroplaning speed (km/h) for longitudinally grooved tires on transversely grooved pavement

Longitudinal Tire Groove Depth (mm)	Transverse Pavement Groove Depth (mm)				
	0.00	2.00	4.76	5.00	9.80
9.80	102.8	180.3	<i>201.4</i>	203.2	226.3
5.00	94.7	175.2	<i>190.9</i>	192.3	220.1
2.00	89.0	170.2	<i>185.0</i>	186.3	216.5
<i>1.60</i>	<i>88.5</i>	<i>169.0</i>	<i>183.8</i>	<i>185.1</i>	<i>215.6</i>
0.00	86.3	164.2	<i>179.1</i>	180.4	212.2



From **Table 1** and converting units,

- › **Base Condition:** Hydroplaning Speed - smooth tire (0mm tire groove depth) with no pavement grooves (0mm pavement groove depth) = 86.3km/h (53.8mph)
- › **Condition 1:** Hydroplaning Speed - longitudinal tire grooves = 1.6mm (2/32 inch) with no pavement grooves = 88.5km/h (55.0mph)
- › **Condition 2:** Hydroplaning Speed - longitudinal tire grooves = 1.6mm (2/32 inch) with pavement grooves per NCDOT specs 4.76mm (3/16 inch) = 183.8km/h (114.2mph)

There is a 1.2mph increase in hydroplaning speed from Base Condition to Condition 1, indicating an increase in hydroplaning speeds associated with 2/32" tire treads. **The additional water shedding capacity from modern tire treads and tread patterns (not quantified here) adds additional conservatism to the recommended increase in predicted hydroplaning speed to account for the 29psi tire pressure.**

There is an 108% increase (Base Condition to Condition 2) in hydroplaning speed results for transverse pavement grooving for cars with standard tire treads. **Noting the significant contribution of transverse grooving on concrete pavement, hydroplaning may be dismissed as a concern for concrete bridge decks using transverse grooving.**

The Fwa and Ong (2009) research was performed using a WFT of 0.3 inch. This thickness value is approximately three times larger than that commonly seen on roadway typical sections. This highlights the need for further research on the effects of tire tread on more commonly seen WFTs, less than 0.1 inch.



#### 4. Analysis of Hydroplaning Potential in Superelevation Transitions

The geometric configuration of a superelevation transition makes these unique areas of concern for hydroplaning and, in most cases, necessitate further analysis. A plan and profile view of this is shown in Figure 9. Long flow paths may result near the zero-cross-slope locations, as shown in Figure 10.

FIGURE 9

Lateral alignment at superelevation transition with superelevation cross slope = 4% (Charbeneau 2008)

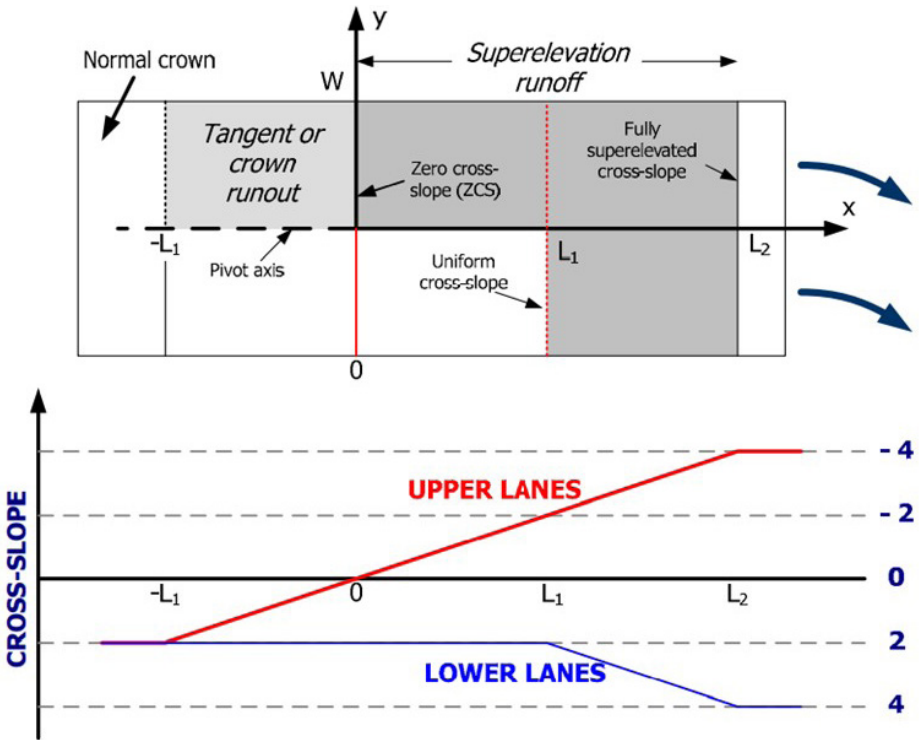
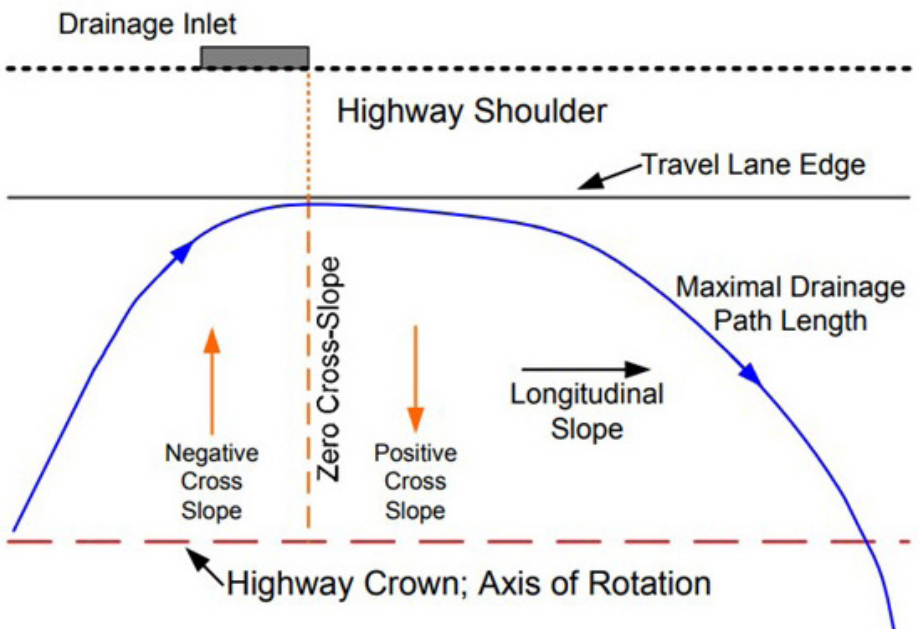



FIGURE 10

Schematic plan view of pavement cross and longitudinal alignment near superelevation transition showing the drainage path with maximal length (Charbeneau 2008)





Empirically derived formulas, such as those used in PAVDRN, are developed for continuously tangent roadway section whose cross slopes and longitudinal slopes are not varying. Therefore, such equations cannot be applied directly to predict the water film depths at superelevation transitions. Charbeneau (2008), however, analyzes WFTs in superelevation transitions using a diffusion wave model.

#### 4.1 NUMERICAL EXPERIMENTS FROM CHARBENEAU (2008)

Charbeneau (2008) conducted 270 numerical experiments using a diffusion wave numerical model, which was developed to simulate stormwater runoff at superelevation transitions to test the sensitivity of WFT depths. He characterizes those experiments as follows:

- › 2 lanes, 3 lanes, and 4-lanes in one direction with 3-meter (10ft.) outside shoulder.
- › 15 longitudinal slopes 0.1%, 0.2%, 0.3%, ..., 0.9%, 1.0%, 2.0%, ..., 5.0%, 6.0%.
- › Rainfall intensity of 100mm/hr (4in/hr), 150mm/hr (6in/hr), 200mm/hr (8in/hr), and 250mm/hr (10in/hr).

The numerical experiment parameters use a normal crown cross slope of 2% and a Manning's  $n$  of 0.015, which correlates to DGAC. While not explicitly stated, Charbeneau's roadway plan/profile layout, shown as **Figure 9** in this article, shows that Charbeneau's numerical modeling was based on a crowned roadway with no median separation, and a maximum superelevation rate of 4%.

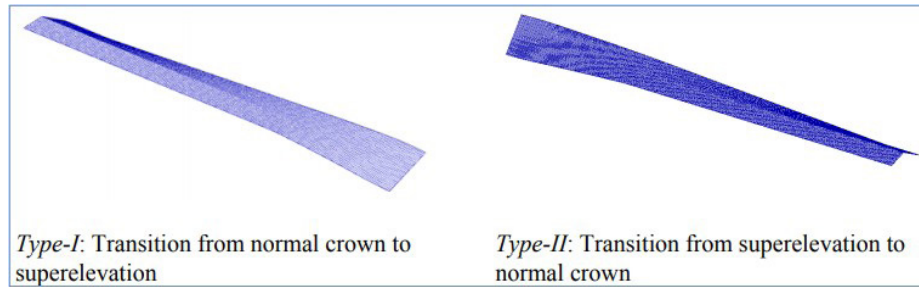
Charbeneau (2008) defines two regimes of superelevation transitions shown in **Figure 11**.

- › Type-I starts with the normal crown on the upstream end and finishes with full superelevation on the downstream end.
- › Type-II starts with full superelevation and finishes with the normal crown.

Simply stated, Type-I is entering superelevation and Type-II is exiting superelevation. Charbeneau then explains, *"From the geometric point of view, Type-I and Type-II roads comprise a curved section, so the two sections face each other at full superelevation. Even though they can be treated as a whole section combined, their geometries induce different sheet flow behaviors and they need to be analyzed separately."*

**FIGURE 11**

Types of the roadway surfaces used in the numerical experiments (Charbeneau 2008)

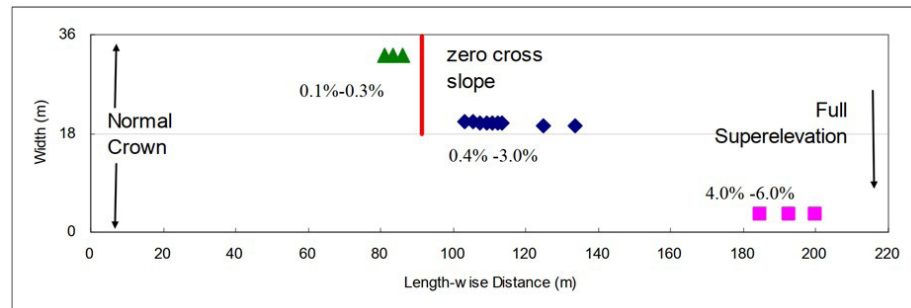


#### 4.2 LOCATION OF MAXIMUM WFT WITHIN SUPERELEVATION TRANSITIONS

Unlike tangent sections where the outside lane always has the longer flow path and greatest WFT, in superelevation transitions, the location of the maximum WFT within the superelevation transition changes with respect to longitudinal slope. In **Figure 12**, Charbeneau (2008) provides expected locations of the maximum WFTs within superelevation transitions for differing longitudinal slopes.

**FIGURE 12**

Locations of peak depth for steady state conditions on various longitudinal slope surfaces (Type-I roads)

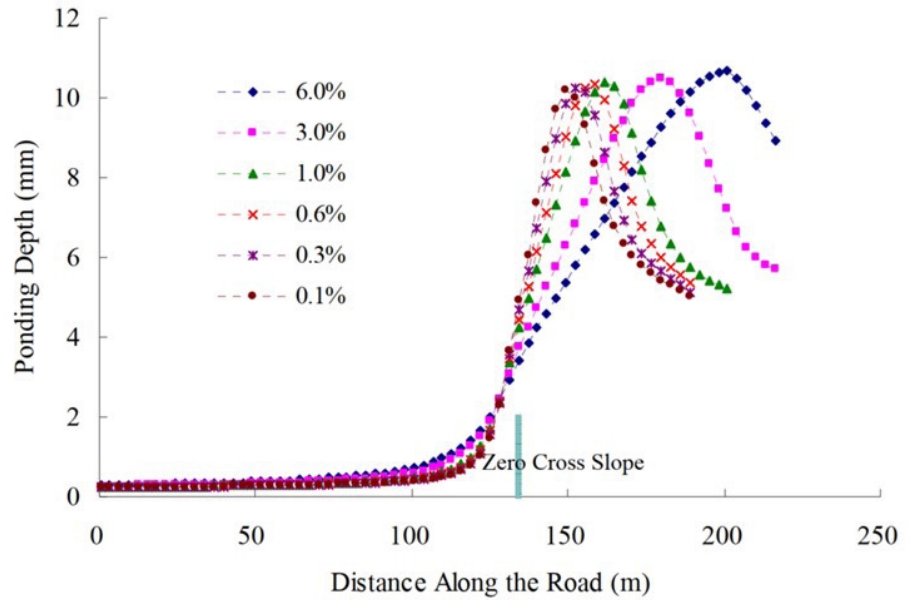


As a matter of practical application, the highest WFT from Charbeneau's model should be assumed to apply anywhere within the superelevation transition. This is similar to the assumption that the predicted driver speed reduction is applied throughout the roadway section.

Noting the spatial extent of the maximum WFT curves shown in **Figure 13**, the *maximum* WFTs are not considerably different for varying longitudinal slopes but the *lane-distance for which the maximum occurs* is greater for steeper longitudinal slopes. Steeper longitudinal slopes result in larger regions with ponded water on the roadway surface, therefore, **flattening longitudinal slope when possible is recommended to reduce hydroplaning potential within superelevation transitions.**

**FIGURE 13**

Longitudinal profile of  
ponding depth at the inside  
end of 4-Lanes in one  
direction under 250mm/  
hr rainfall (Type-II roads)



#### 4.3 MAGNITUDE OF WFT WITHIN SUPERELEVATION TRANSITIONS

##### 4.3.1 COMMUNICATIONS WITH DR. CHARBENEAU IN 2022

Recognizing that the linear regression equations for rainfall intensity from Charbeneau (2008) was incorrect, Atkins contacted Dr. Randy Charbeneau, who graciously located and provided most of the original data for the project, along with a sample polynomial corrected regression equation for one longitudinal slope. Revised regression equations were developed for all longitudinal slopes and lane widths used in the original research.

##### 4.3.2 DETERMINATION OF SE TRANSITION WFT FACTORS

To estimate the WFT through a superelevation transition of a roadway section, the Charbeneau superelevation transition WFTs was normalized by the Charbeneau (2008) base tangent sections, creating a superelevation factor, and then multiplied by the tangent WFT of the section being assessed:

$$\text{Section SEWFT} = \text{Section Tangent WFT} \times \underbrace{\left( \frac{\text{Charbeneau Superelevation WFT}}{\text{Charbeneau Tangent WFT}} \right)}_{\text{Superelevation Factor}}$$

(Equation 5)

SE transition WFT factors were developed for the full range of Charbeneau (2008) numerical experiments, but with the addition of 2in/hr values:

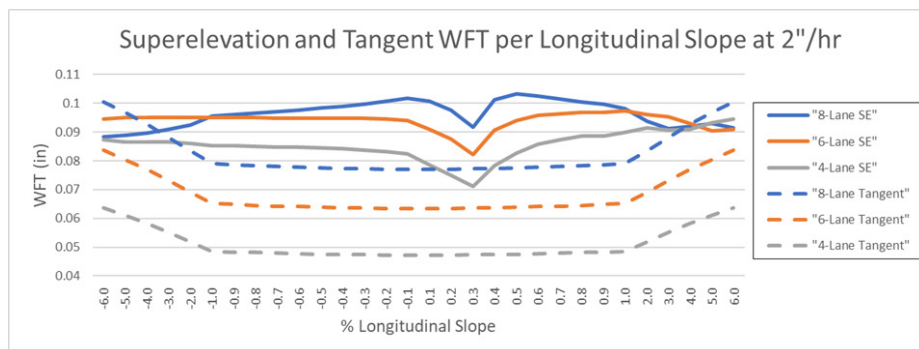
- › 2 lanes, 3 lanes, and 4-lanes in one direction with 10 ft. outside shoulder.
- › 15 longitudinal slopes 0.1%, 0.2%, 0.3%, ..., 0.9%, 1.0%, 2.0%, ..., 5.0%, 6.0%.
- › Rainfall intensity of 2in/hr, 4in/hr, 6in/hr, 8in/hr, and 10in/hr.

Both Type-I and Type-II transitions were evaluated.

For the SE WFT, the data provided by Dr. Charbeneau was used and missing data was extrapolated using curve fit equations from available data. The tangent WFT was calculated using the spreadsheet used for the numerical verification of the Hydroplaning Assessment Tool. Results are plotted in **Figure 14**, along with a brief discussion.

**FIGURE 14**

SE and tangent  
WFT at 2in/hr



Note that for slopes steeper than 1%, the computed SE WFT results are questionable for the 6- and 8-lane sections. In personal correspondence, Dr. Charbeneau speculated that, *"It could be that the diffusion wave model (gravity and pressure gradients) becomes inadequate as the longitudinal slope becomes too large because inertial forces become important. I am sure this has been looked at in the general literature, but I am not aware of any specific studies involving sheet flow."*

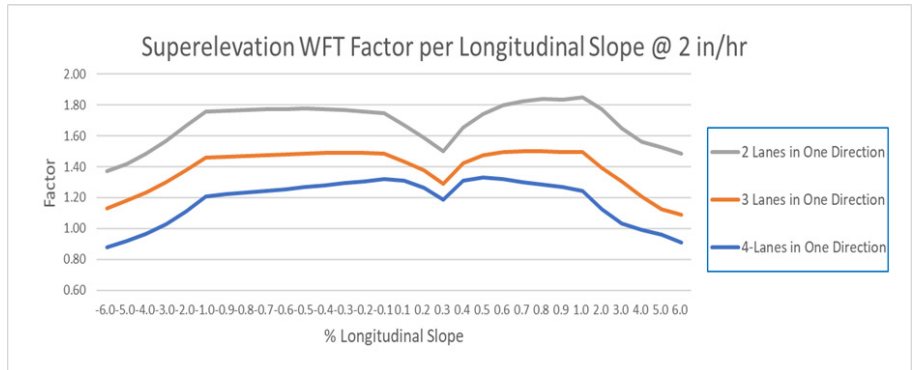




Figure 15 examines the SE factors for the 2in/hr rainfall.

FIGURE 15

SE factors for  
2in/hr rainfall



To be conservative, the largest SE factor for each roadway section will be used regardless of the longitudinal roadway slope through the transition area. This approach yields the factors tabulated below in **Table 2**. The 2-lane SE factor was chosen to be 1.8, even though a single point is at 1.85, since 1.8 is more representative of the values in that area of the 2-lane curve. Noting that SE factors are reducing with increased number of lanes, the 4-lane SE factor of 1.3 will conservatively be used for roadways with greater than 4 lanes in one direction.

TABLE 2

Summary of superelevation  
WFT factors

Superelevation WFT Factors for Divided Highways:  
Longitudinal Slopes 0.1% - 6.0%,  $e \geq 2\%$

Lanes in One Direction	Superelevation WFT Factor
2-lanes	1.8
3-lanes	1.5
4-lanes	1.3
> 4-lanes	1.3

## 5. Conclusions

---

The programmatic improvements developed by Atkins for NCDOT advance the state of hydroplaning practice using sound, yet conservative, methodologies for determining potential risk. Hydroplaning research advancements are needed in the field of water film thickness measurements using non-contact devices, added safety from modern tire tread patterns and advanced vehicle testing on wet pavement surfaces to further validate existing models and verify the hydroplaning risk assessment process. We believe the results are applicable to DOTs across the US and other regions of the world and are robust in a variety of future scenarios.



## References

---

- › Choubane, Bouzid, Charles Holzschuher, and Salil Gokhale (2006), Precision of Smooth and Ribbed Tire Locked Wheel Testers for Measurement of Roadway Surface Friction Characteristics, **Research Report 06-483**
- › Gunaratne, M. et al., (2012), "Hydroplaning on Multi Lane facilities." **Project No. BDK84 977-14.**
- › Lee, Hyung S., Dinesh Ayyala (2020), "Enhanced Hydroplaning Prediction Tool." **Project No. BE570**
- › Huebner, R. Scott, Joseph R. Reed, and John J. Henry. "Criteria for Predicting Hydroplaning Potential." *Journal of Transportation Engineering*, Vol 112, No. 5, September 1986.
- › Flintsch, G. et al., (2020), "Guidance to Predict and Mitigate Dynamic Hydroplaning on Roadways", *NCHRP Project 15-55.*
- › Charbeneau, Randall J., Jaehak Jeong, and Michael E. Barrett. (2008) "Highway Drainage at Superelevation Transitions." *Report No. FHWA/TX-08/0-4875-1.*
- › Fwa, T.F., Kumar Anupam and G. P. Ong. (2010) "Relative Effectiveness of Grooves in Tire and Pavement in Reducing Vehicle Hydroplaning Risk." *Transportation Research Board.*
- › Horne, W. B. and Dreher, R. C. (1963). *Phenomena of Pneumatic Tire Hydroplaning*, NASA TN D-2-56, NASA Langley Research Center, NASA, Hampton, VA.
- › Anderson, David A., R. Scott Huebner, Joseph R. Reed, John C. Warner, and John J. Henry. (1997) "Improved Surface Drainage of Pavements." *NCHRP Project 1-29.*
- › Huebner R. Scott, J. C. Warner, D. A. Anderson, and J. R. Reed. "PAVDRN: A Computer Model for Predicting Water Film Thickness and the Potential for Hydroplaning on New and Reconditioned Pavements." *Transportation Research Record Journal of the Transportation Research Board*, January 1997.
- › Gallaway et al, (1979). "Pavement and Geometric Design Criteria for Minimizing Hydroplaning", FHWA RD-79-31.

- › Agrawal, S. K., Meyer, W. E., and Henry, J. J., "Measurement of Hydroplaning Potential," Report No. FHWA-PA-72-6, Final Report to Pennsylvania Department of Transportation, Pennsylvania Transportation Institute, Pennsylvania State Univ., 1977 (NTIS No. PB 265061).
- › Ong, G. P. and Fwa, T. F. (2007). "Prediction of Wet-Pavement Skid Resistance and Hydroplaning Potential." *Transportation Research Record: Journal of the Transportation Research Board*, No. 2005, Transportation Research Board of the National Academies, Washington, D.C., 2007.
- › Fwa, T. F and Ong, G. P. (2009). "Relative Effectiveness of Grooves in Tire and Pavement in Reducing Vehicle Hydroplaning Risk." *TRB 2010 Annual Meeting, Transportation Research Board of the National Academies, Washington, D.C., 2010.*













**Ken Hunu, PE, DWRE, PMP, CFM**  
Technical Manager II  
Engineering Services – Water TPO USA  
Raleigh, NC, USA



**Mike Walters, PE, PG, PH**  
Sr. Engineer IV  
Engineering Services – Water TPO USA  
Tampa, FL, USA



**Khaled Pordel, PE, Ph.D., CFM**  
Sr. Engineer I  
Engineering Services – Water TPO USA  
Raleigh, NC, USA

## 02. Water Engineering

# Development of Rainfall Intensity Duration Frequency (IDF) Curves for the NEOM Region, Saudi Arabia

## Abstract

NEOM is a planned independent economic zone in Northwest Saudi Arabia with a vision to be the land of the future where the greatest minds are empowered to embody pioneering ideas. To achieve this vision, a hydrologic modeling guidance document, which includes Intensity Duration Frequency (IDF) curves, has been developed. Innovative approaches were used to develop the IDF curves to overcome regional data limitations. These approaches can be applied in arid areas in other parts of the world. Rainfall magnitudes for durations of 5 minutes, 10 minutes, 15 minutes, 30 minutes, 1 hour, 2 hours, 3 hours, 6 hours, and 24 hours were generated for the 5-year, 10-year, 25-year, 50-year, 100-year, 200-year, 500-year, and 1,000-year return periods for the entire NEOM region. The results show spatial variation and mimic the expected orographic effects of the mountains and moisture obtained from the Red Sea and the Gulf of Aqaba.

## KEYWORDS

Intensity duration frequency curves; Arid areas; Climate change; Data scarcity; Innovation

# 1. Introduction

NEOM is a planned independent economic zone in Northwest Saudi Arabia with a vision to be the land of the future where the greatest minds and best talents are empowered to embody pioneering ideas and exceed boundaries in a world inspired by imagination (NEOM, 2020). The area is bounded by the Red Sea on the south and the Gulf of Aqaba on the west (See **Figure 1A**). An arid climate with rare, high-intensity rainfall events characterizes the NEOM region. The landscape is very dry (See **Figure 1B**).

**FIGURE 1A**  
NEOM's geographic location



**FIGURE 1B**  
NEOM region landscape





To achieve NEOM's vision, a guidance document that defines the most appropriate hydrologic analysis methodology for the NEOM region, recommends innovative hydrologic approaches to overcome data limitations in the region, and establishes baseline hydrologic data and flood-runoff methods for future hydrologic and hydraulic analysis has been developed. The guidance includes the development of Intensity Duration Frequency (IDF) curves.

This paper describes the innovative approaches employed to overcome the data challenges to develop reliable IDF curves for the NEOM region and how those approaches can be applied in arid areas of the United States and other parts of the world.

## **2. Methodology**

---

### **2.1 AVAILABLE DATA AND REVIEW**

The IDF analysis is dependent on short-duration rainfall data availability for many years. Some historical daily rainfall data, spanning mostly from 2015–2021, from rainfall gauge stations is available. The locations of these rainfall stations are shown in **Figure 2**. Nine of these stations are located within the NEOM region. Only 2 stations (Al-qalibah and Aqaba stations) have more than 20 years of data. The record length of the data is not adequate for the estimation of IDF curves for the region. Sub-daily rainfall data, needed to estimate IDF curves for the region was also not available.

In the absence of site-specific climate station data, four different types of gridded products can be considered to provide rainfall estimates, each with its own key strengths and weaknesses. The gridded products include (1) interpolated gridded data based on the network of available rain gauges, (2) satellite products, (3) a blend of satellite and rain gauge data, and (4) re-analysis products. The choice of a dataset depends on its application and geographic location.



FIGURE 2

Rainfall stations



For creating IDF curves or regional frequency analysis, daily or sub-daily rainfall that has adequate spatial resolution and captures extreme events is required. To choose such a dataset for this purpose, a quality assessment is required. Normally a quality assessment would involve evaluating gridded products against available in-situ rain-gauge observations to determine their usefulness. Understanding its quality allows it to be used for detailed climatological assessment spatially and temporally.

The Arabian Peninsula is characterized by quite a varied climate, where Saudi Arabia is characterized by complex topography and has distinct climatic regions. Over large parts of the country, precipitation is infrequent, and temperatures are high and characterized by a desert climate. However, the southwestern portion of the country is classified as semi-arid.



The annual rainfall in most parts of the country is below 150mm throughout the year, except in the southwestern part where the total annual rainfall ranges between 400 to 600mm. Due to the complex interactions between the different dynamic synoptic processes, including mid-latitudes and monsoon influences, rainfall is typically highly variable in space, time, and intensity and can be very localized. Rainfall generally occurs during the cooler months of October to May. Extreme rainfall events have frequently led to flooding with loss of life, evacuations, and extensive damage to infrastructure (De Vries et al., 2016). Extreme precipitation events in Jeddah, Saudi Arabia have been associated with mesoscale convective systems (MCS), the Hijaz mountains to the east of the city, and the land-sea interaction to the west. MCSs are typically associated with intense rainfall and of short duration, initially leading to longer periods of steady rainfall.

The challenges in accurately characterizing rainfall across Saudi Arabia are due to a lack of complete, long-term, geographically distributed, and reliable climate datasets. A lack of regionally consistent datasets can be related to issues with rain-gauge placement, gaps in the temporal record, aging infrastructure, and the costs to redevelop such an observation network (Kenawy and McCabe, 2016).

Based on our assessment of the observed rainfall data, rainfall in the NEOM region can be random in space and discontinuous in time. For small scales, for example, the use of measurements from individual rain gauges may be sufficient; however, when evaluating rainfall across a broader region that is driven by MCSs at scales of 10s to 100s of km, a solution could be gauge-based precipitation dataset such as the Global Precipitation Climatology Centre (GPCC) dataset (Becker et al., 2013). However, their application has significant disadvantages due to their inability to represent extremes. Satellite precipitation datasets potentially constitute an alternative to gridded products based on interpolated rain gauge station data. A combination of gauge-based data and satellite data allows for an enhancement of the dataset quality. One such dataset is the Tropical Rainfall Measurement Mission Project (TRMM 3B42), where the indirect measurements (along with direct rain-gauge measurements) are used as an input to a complex algorithm that provides estimates of surface rain rates on a regular grid in space and time. Another option is to consider re-analysis data such as the ECMWF ERA5 product, which combines inaccurate and incomplete observations with imperfect numerical weather prediction models to provide a global high-resolution dataset.

TRMM 3B42 and ECMWF ERA5 re-analysis data are available for the NEOM region. TRMM 3B42 data is available on a 3-hour temporal scale and 0.25-degree by 0.25-degree spatial scale from 1997 to 2019. ECMWF ERA5 re-analysis product (Hersbach et al., 2018) is available on an hourly temporal scale and 0.25-degree by 0.25-degree spatial scale from 1959 to the present. Re-analysis combines model data with observations from across the world into a globally complete and consistent dataset using the laws of physics. A re-analysis provides a synthesized estimate of the climate state generated from a combination of a numerical model and as many observations as possible of the earth system. Observations can be directly assimilated into the numerical simulation or used indirectly through the forcings of the simulation. The climate estimates can be global or regional, spanning from a few years to almost two centuries. Global Precipitation Measurement (GPM) data is also available for the region. Global Precipitation Measurement (GPM) data is the most updated TRMM data and is available from 2000 to the present. The spatial and temporal resolution of GPM data is 0.1-degree by 0.1-degree (10km x10km) and 30 minutes, respectively. The ECMWF ERA5 hourly data was selected as the most appropriate for our IDF analysis because it had the longest record, a high temporal resolution, and is most consistent with ground data. The advantages and limitations of the ECMWF ERA5 hourly data are shown in **Table 1**.

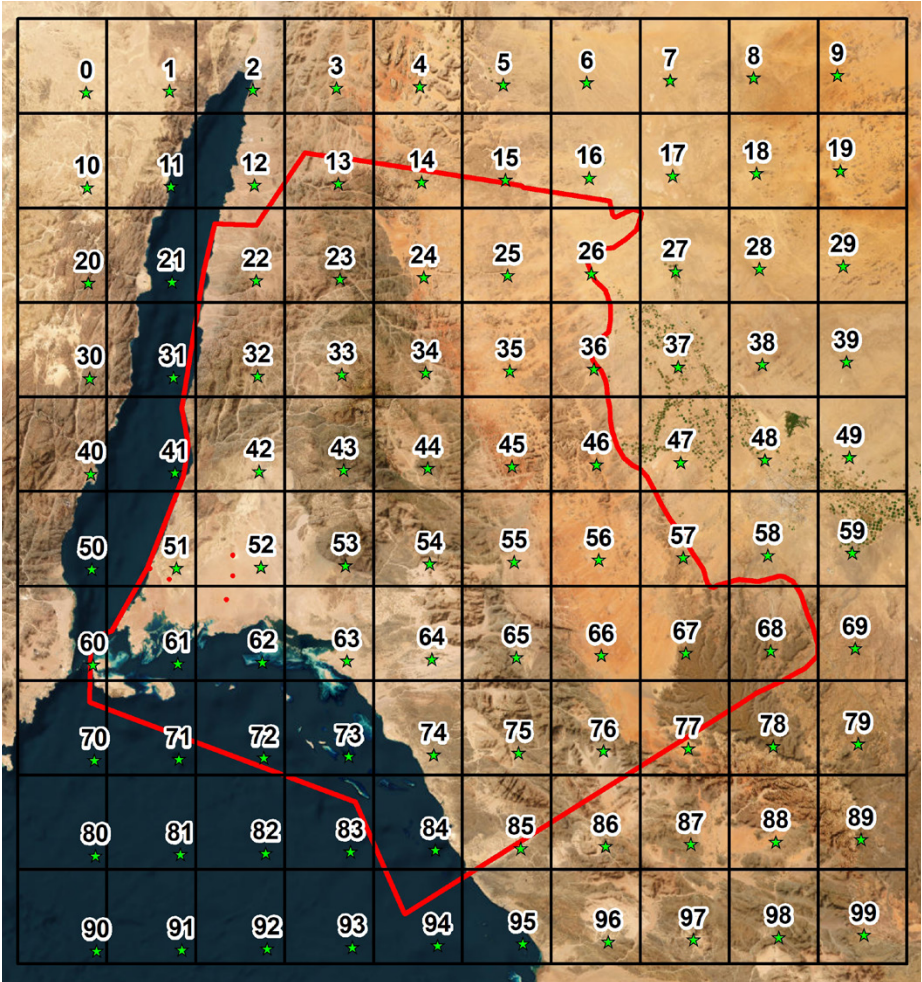
TABLE 1

Properties of ERA5 re-analysis data		
Product	Advantages	Limitations
ERA5 re-analysis data	Offers high spatial and temporal resolution rainfall estimates. Compared to previous coarser resolution versions, it is better able to resolve large convective scale processes of interest to this study.	Global re-analysis will not be able to fully capture very small-scale intense convection; although it may have the correct spatial detail, it can lead to underestimation of rainfall intensities of short-duration events.
Spatial: 0.25 deg x 0.25 deg		
Temporal: hourly	Useful for investigating rainfall frequency and intensity.	This is critical to the type of extreme rainfall experienced across the KSA.
Temporal		
Coverage: 1959 to present	Analysis has shown the "promising applicability of (1) re-analysis data to estimate IDF relationships, and (2) daily rainfall records to estimate sub-daily IDF curves".	

Data accessed from: <https://cds.climate.copernicus.eu/>

FIGURE 3

Re-analysis rainfall grid



The ERA5 re-analysis data were available in the form of hourly measurements for each of the 100 grid cells spanning the NEOM region (Figure 3).



The ECMWF ERA5 data were compared to the available rainfall station data at Albada, Alqalibah, Tabuk, and Neom City rain gauge stations. The comparison indicated that:

1. The date of occurrence for most of the rainfall events (especially the peak rainfall event) on the ground matches the rainfall events in the re-analysis dataset. This means that if there is a rainfall event on the ground on a specific date, it probably has the same event occurrence record in the re-analysis data.
2. There were differences between the peak rainfall depths recorded at the rain gauge stations and those in the re-analysis data. The re-analysis estimate was consistently less than the recorded ground estimates across the NEOM region. This could be because the re-analysis estimate is averaged over a 0.25-degree grid and hence may dilute localized peak estimates.
3. There are many relatively smaller rainfall events within the re-analysis data that are not reported by the ground station (the ground station shows zero rainfall for that date). This could be due to a failure to manually record the rainfall amount at the rain gauge station or errors in the re-analysis estimates. Since the rainfall frequency analysis is based on peak rainfall amounts, the exclusion of the relatively smaller events from the station record is not likely to impact the results of the statistical analysis of the station data.

Due to these observations, the re-analysis data results were adjusted based on the observed rain gauge data as described in the subsequent sections. The upward adjustment accounts for the possible underestimation of localized rainfall peaks in the re-analysis data due to its 0.25-degree (25km) spatial resolution.

The ECMWF ERA5 data were processed to obtain 1-hour, 2-hour, 3-hour, 6-hour, 12-hour, and 24-hour maximum rainfall depths. One main advantage of the re-analysis is that it provides details on spatial variation, which is not provided by ground data within NEOM. The spatial rainfall variation is demonstrated in **Figure 4**, which shows the average, maximum, and minimum of the peak hourly rainfall from 1960 to 2021.

FIGURE 4A

Average of  
peak hourly rainfall  
High: 4.81mm. Low: 2.03mm.

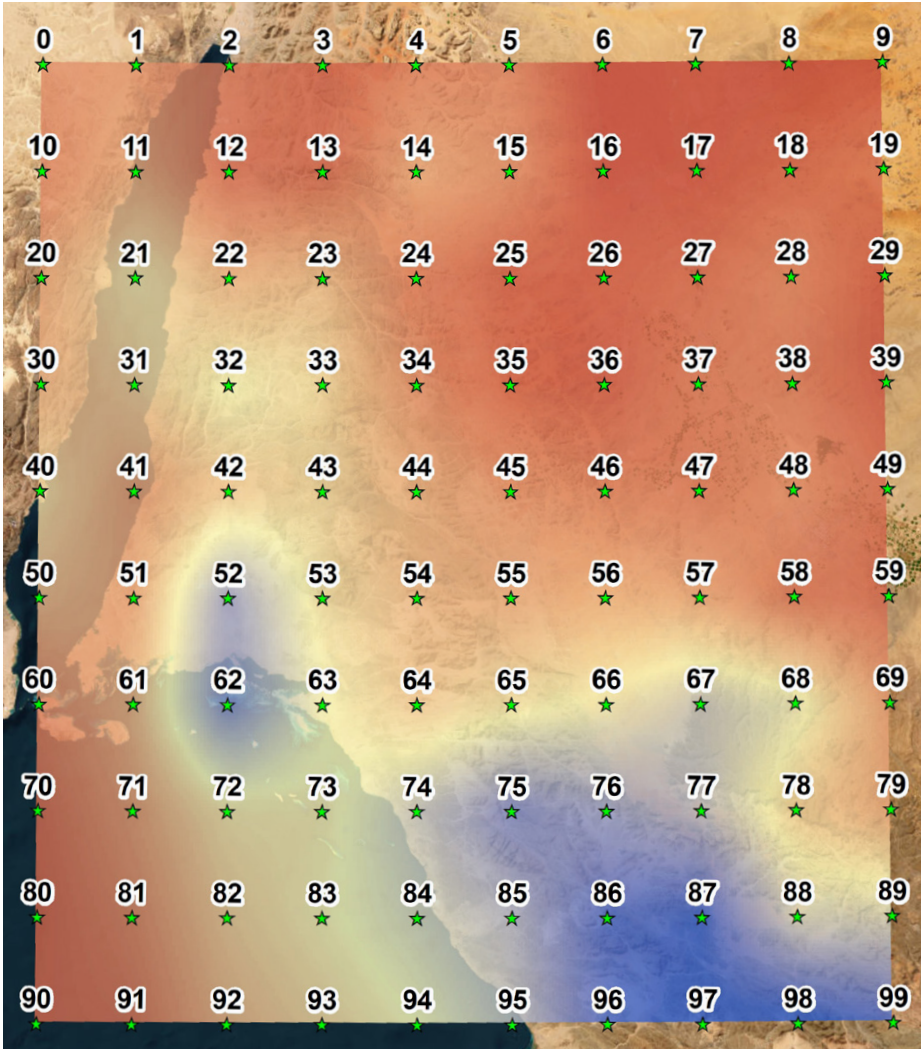


FIGURE 4B

Maximum of peak hourly  
rainfall High: 17.47mm.  
Low: 5.8mm.

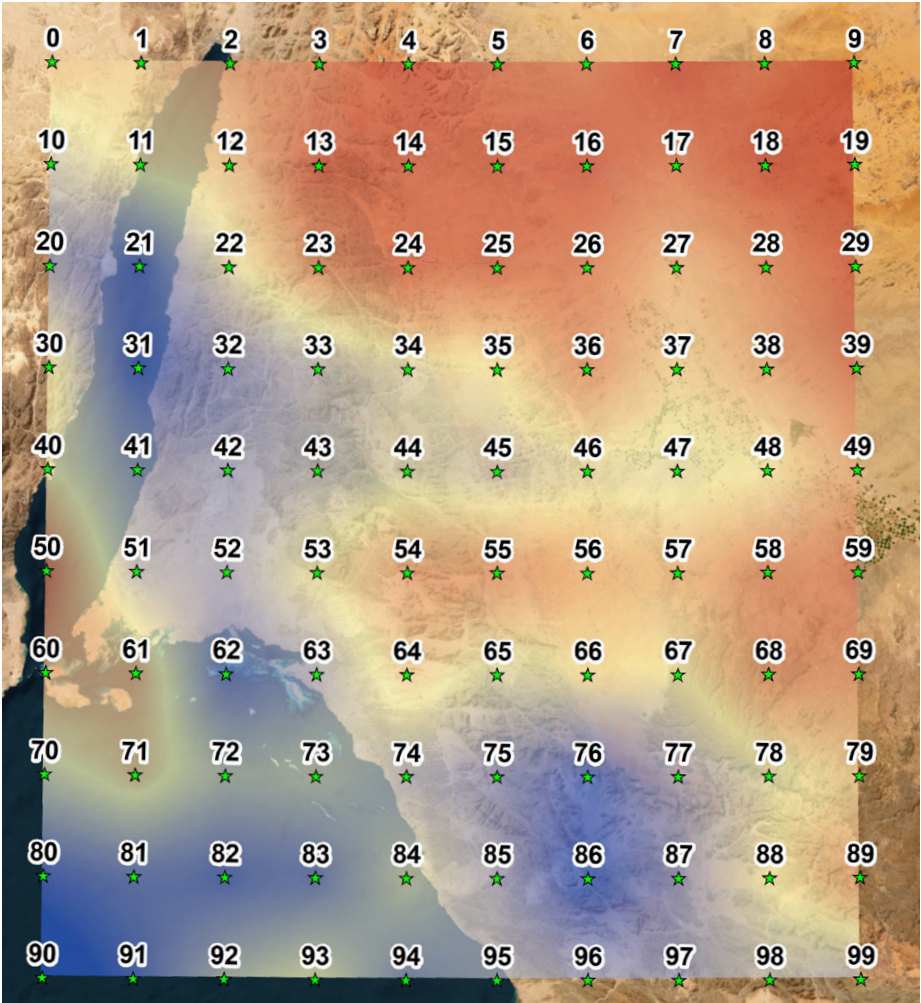
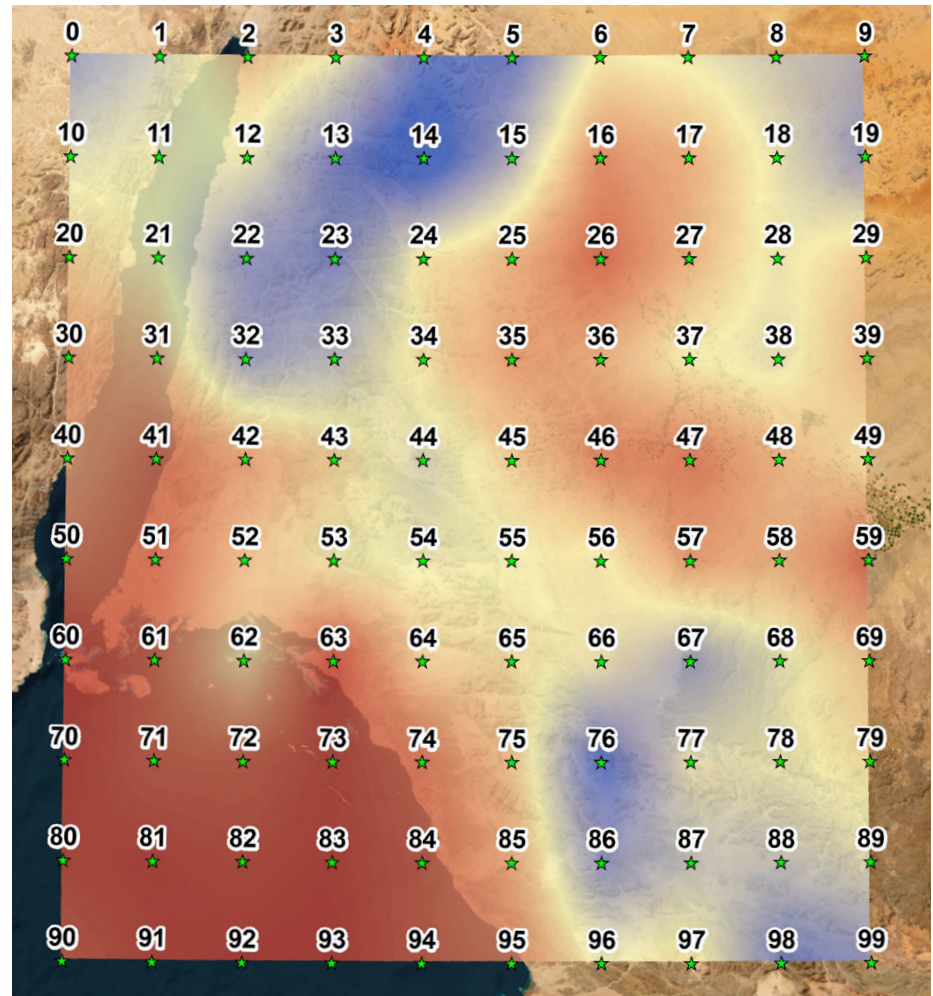


FIGURE 4C

Minimum of peak hourly  
rainfall High: 1.04mm.  
Low: 0.07mm.



The three figures above show significant spatial variation in the dataset. The variations shown are consistent with the available rain gauge data. They also show greater amounts of rainfall to the west of the mountain range. This is expected because the wind direction is towards the east. Consequently, moisture transported by the wind from the Red Sea and Gulf of Aqaba is shed as rainfall on the western side by the orographic effect.



## 2.2 DATA ANALYSIS

Hourly data was analyzed using the US Army Corp of Engineers (USACE) Hydraulic Engineering Center's Statistical Software Package (HEC-SSP) program. Sub-hourly data were not available, but an approach was developed for 5-minute, 10-minute, 15-minute, and 30-minute duration rainfall estimates. The steps taken to develop the IDF curves for NEOM are summarized in **Figure 5**.

The use of two different methodologies for durations greater than 1-hour and those less than 1-hour resulted in inconsistencies in total rainfall estimates at a few locations (e.g., the 1-hour total rainfall being more than the 2-hour rainfall). In such cases, the methodology for the short duration was used to smoothen out the results.

FIGURE 5

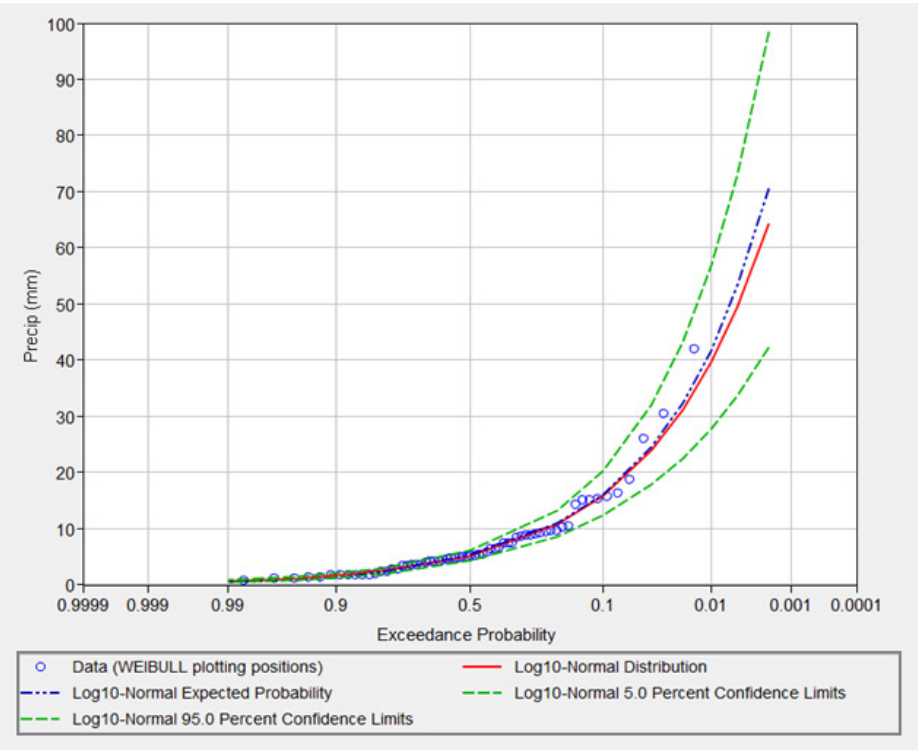
IDF Development Steps



2.2.1 HEC-SSP ANALYSIS

FIGURE 6

HEC-SSP example results



HEC-SSP is a program developed by the USACE and is based on technical procedures documented in the USGS Bulletin 17C (England et al., 2019). Many frequency distributions are available within HEC-SSP, but this project utilized the log-Normal distribution. HEC-SSP utilizes the Kolmogorov-Smirnov (USACE, 2019) Goodness of fit test to determine which distribution best fits the data. The data was tested against the Weibull plotting position. The log-Normal distribution provided convergence for all data sets and provided a good fit to the rainfall data compared to other distributions, as demonstrated by low Kolmogorov-Smirnov test scores. A total of 500 HEC-SSP frequency analyses were performed for each grid (0-99) and for 1-hour, 2-hour, 6-hour, 12-hour, and 24-hour durations using the ECMWF ERA5 data. This information provided the basis for the IDF data for durations of 1, 2, 6, 12, and 24 hours. An example of the information from HEC-SSP is shown in **Figure 6**.

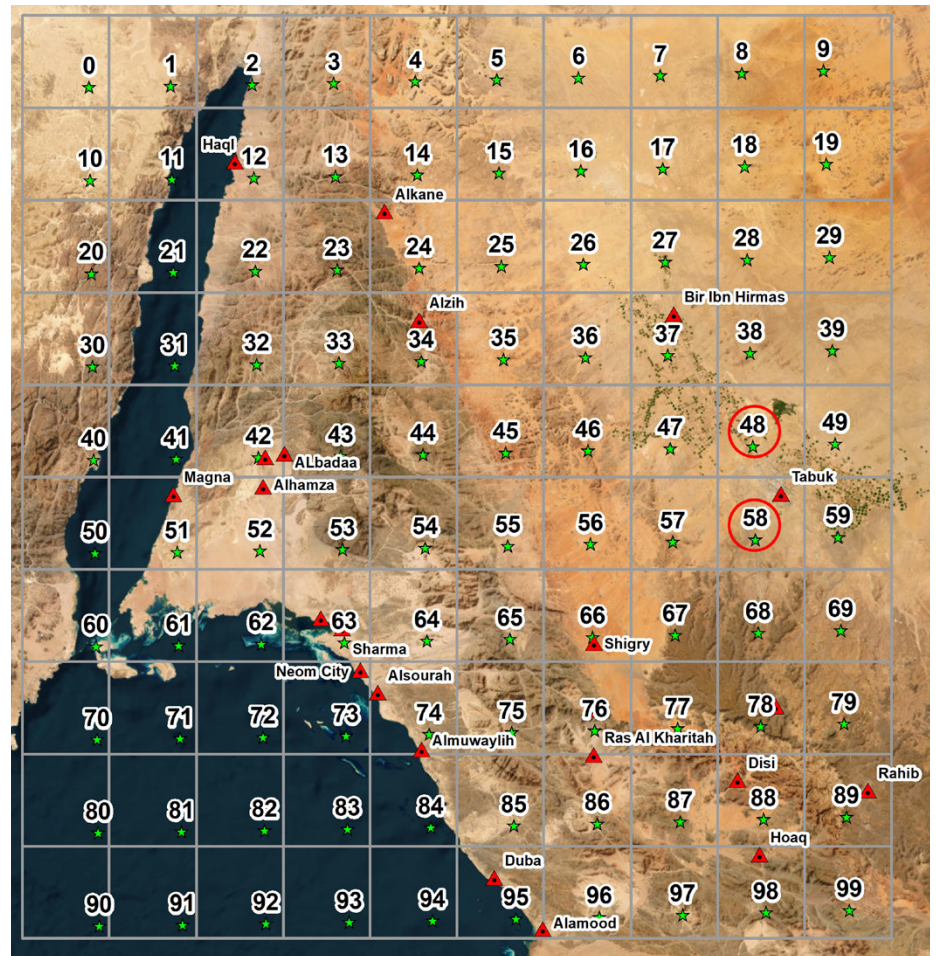


Shown in **Table 2** are ratios expressing the Intensity-duration values derived from the Tabuk rain gauge rainfall divided by those derived from the re-analysis rainfall.

The ratios were derived by dividing the HEC-SSP results based on Tabuk rain gauge data by the results derived from the average of the re-analysis data at grids 48 and 58 (**Figure 7**) near the Tabuk rain gauge. Our investigation shows that the re-analysis data consistently provided uniformly lower values across the NEOM region; thus, applying an adjustment factor based on the Tabuk gauge is reasonable.

**FIGURE 7**

Tabuk rain gauge  
(grid points circled in red)  
used for comparison





The adjustment ratios in **Table 2** were used as multipliers to adjust the results developed based on the re-analysis data.

**TABLE 2**

Return Period* (years)	Duration (Hours)*				
	1	2	6	12	24
Adjustment ratios					
500	2.17	2.17	2.17	2.17	2.17
200	2.05	2.05	2.05	2.05	2.05
100	1.96	1.96	1.96	1.96	1.96
50	1.88	1.88	1.88	1.88	1.88
25	1.78	1.78	1.78	1.78	1.78
10	1.66	1.66	1.66	1.66	1.66
5	1.55	1.55	1.55	1.55	1.55

\*Note that there are no adjustment ratios for the 1000-year return period and 3-hour duration because those values were extrapolated and interpolated, respectively, from the final adjusted values.

#### 2.2.2 APPROACH FOR SUB-HOURLY IDF CURVES AND RATIO TO 24-HOUR RAINFALL

IDF curves were developed for Saudi Arabia by Atkins (2019). The report included the development of IDF curves for Tabuk, just to the east of the NEOM project area. Data were available for 10, 20, and 30 minutes, and for 1, 2, 3, 6, 12, and 24 hours. These data were used to develop regression equations ( $y=ax^b$ ), where  $a$  is the coefficient,  $b$  is the exponent,  $y$  is the rainfall intensity, and  $x$  is the duration in hours, so that estimates could be made of the required 5-, and 15-minutes durations. Regression parameters are shown in **Table 3**.

**TABLE 3**

Return Period (years)	200	100	50	25	10	5
Regression parameters						
R <sup>2</sup>	0.9731	0.9733	0.9776	0.9812	0.9841	0.9864
Coefficient	26.17	20.0510	17.87	15.437	12.066	8.8642
Exponent	-0.59	-0.591	-0.618	-0.646	-0.682	-0.704

\*The above information was derived from the Tabuk (Atkins, 2019) dataset, where there was no analysis for the 500-year, or 1000-year storms or 15-minute duration storms. The 15-minute storms were derived from the above regression parameters.



**Table 4** below shows the results of utilizing the regression equation parametrized in **Table 3**. The rainfall values in **Table 4** were compared to the 24-hour value by dividing the results by the 24-hour rainfall. Results are shown in **Table 5**. The ratios for the sub-hourly durations in **Table 5** were multiplied by the adjusted 24-hour intensities to develop the sub-hourly intensities. Due to the lack of information about the sub-hourly data for the 500-year return period, the ratios for the 200-year return period were conservatively used for the 500-year return period.

**TABLE 4**

Rainfall (mm/hr) for various duration and return period

		T - Return Period (Years)					
		200	100	50	25	10	5
Minutes	5	113.4	87.1	83.0	76.9	65.7	51.0
	10	75.3	57.8	54.1	49.1	41.0	31.3
	15	59.3	45.5	42.1	37.8	31.1	23.5
	30	39.4	30.2	27.4	24.2	19.4	14.4
Hours	1	26.2	20.1	17.9	15.4	12.1	8.9
	2	17.4	13.3	11.6	9.9	7.5	5.4
	6	9.1	7.0	5.9	4.9	3.6	2.5
	12	6.0	4.6	3.8	3.1	2.2	1.5
	24	4.0	3.1	2.5	2.0	1.4	0.9

Spatial variation was accounted for by relating all datasets to the 24-hour rainfall (**Table 5**) derived from the SSP analysis for each of the 100 grids. These 24-hour results included relevant multipliers shown in **Table 2**. Therefore, the spatial variation derived from the ECMWF ERA5 hourly data was transposed to the entire NEOM area.

As indicated in previous sections of the report, the 3-hour intensity and 1000-year return period values were estimated by interpolation and extrapolation with regression techniques.

TABLE 5

TABLE 5		T - Return Period (Years)							
		500	200	100	50	25	10	5	
Ratio to 24-hour rainfall	Minutes	5	28.3	28.3	28.4	33.1	38.8	47.6	53.9
		10	18.8	18.8	18.9	21.6	24.8	29.6	33.1
		15	14.8	14.8	14.8	16.8	19.1	22.5	24.9
		30	9.8	9.8	9.9	10.9	12.2	14.0	15.3
	Hours	1	6.5	6.5	6.5	7.1	7.8	8.7	9.4
		2	4.3	4.3	4.3	4.6	5.0	5.4	5.8
		6	2.3	2.3	2.3	2.4	2.4	2.6	2.7
		12	1.5	1.5	1.5	1.5	1.6	1.6	1.6
		24	1.0	1.0	1.0	1.0	1.0	1.0	1.0



### 3. Results and Discussion

---

#### 3.1 SUMMARY

**Table 6** and **Table 7** show the results of the final IDF curve for Grid 48 (near Tabuk). **Figure 8A** is a plot for the 100 year 6-hour storms and demonstrates the spatial variation of rainfall within the NEOM Region. An example plot of the final IDF curves is shown **Figure 8B**.

The IDF curves and procedure detailed herein will provide an operative and concise methodology for deriving maximum rainfall events expected to occur in the NEOM region. It will also help determine their frequency of occurrence based on typical NEOM region storm durations. Moreover, the rainfall totals and distributions for each grid can be added as an input to the hydrologic models (e.g., HEC-RAS and HEC-HMS) to calculate the expected maximum streamflow (i.e., wadi flows) where streamflow records are not available. The innovative method presented herein can be used to develop rainfall data for other data scarce regions across the globe.



TABLE 6

Example of an  
adjusted IDF table

Grid ID: 48								
Rainfall Intensity (mm/hr) by Duration and Return Period (Year)								
Return Period								
Duration	5	10	25	50	100	200	500	1000
5-min	38.4	52.5	70.0	84.0	95.7	128.0	184.7	219.4
10-min	23.6	32.6	44.7	54.8	63.7	85.0	122.7	150.2
15-min	17.8	24.8	34.5	42.7	49.9	67.0	96.6	120.0
30-min	10.9	15.4	22.0	27.7	33.4	44.5	64.2	82.2
1-hr	6.7	9.6	14.1	18.0	21.9	29.4	42.5	55.8
2-hr	4.0	6.1	9.4	12.7	16.5	21.4	29.0	42.3
3-hr	3.6	5.4	8.4	11.4	14.8	19.2	26.1	38.4
6-hr	2.1	3.3	5.3	7.3	9.7	12.7	17.6	26.6
12-hr	1.2	2.0	3.2	4.6	6.2	8.3	11.7	18.1
24-hr	0.7	1.1	1.8	2.5	3.4	4.5	6.5	9.8

TABLE 7

Example of IDF curve in  
terms of total depths

Grid ID: 48								
Rainfall Totals (mm) by Duration and Return Period (Year)								
Return Period								
Duration	5	10	25	50	100	200	500	1000
5-min	3.2	4.4	5.8	7.0	8.0	10.7	15.4	18.3
10-min	3.9	5.4	7.5	9.1	10.6	14.2	20.5	25.0
15-min	4.4	6.2	8.6	10.7	12.5	16.7	24.2	30.0
30-min	5.5	7.7	11.0	13.8	16.7	22.2	32.1	41.1
1-hr	6.7	9.6	14.1	18.0	21.9	29.4	42.5	55.8
2-hr	8.1	12.2	18.9	25.4	33.1	42.7	58.0	84.6
3-hr	10.7	16.1	25.2	34.1	44.4	57.6	78.4	115.0
6-hr	12.5	19.6	31.7	43.6	58.0	76.2	105.4	159.5
12-hr	14.5	23.6	38.6	54.6	73.9	99.3	140.5	217.4
24-hr	17.1	26.5	43.3	60.9	80.9	108.7	156.9	235.5

FIGURE 8A

Spatial variation  
of 100yr\_6hr\_  
rainfall intensity.  
High: 25.7mm/hr  
Low: 4.54mm/hr

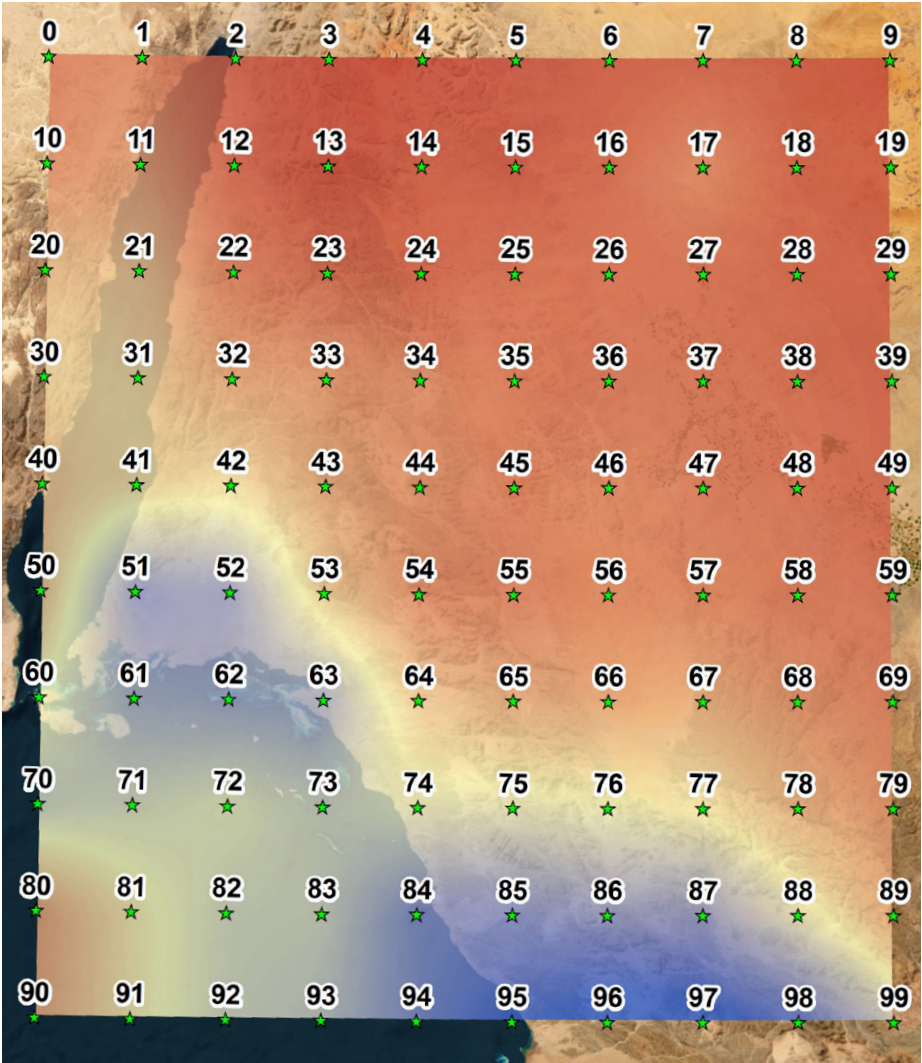
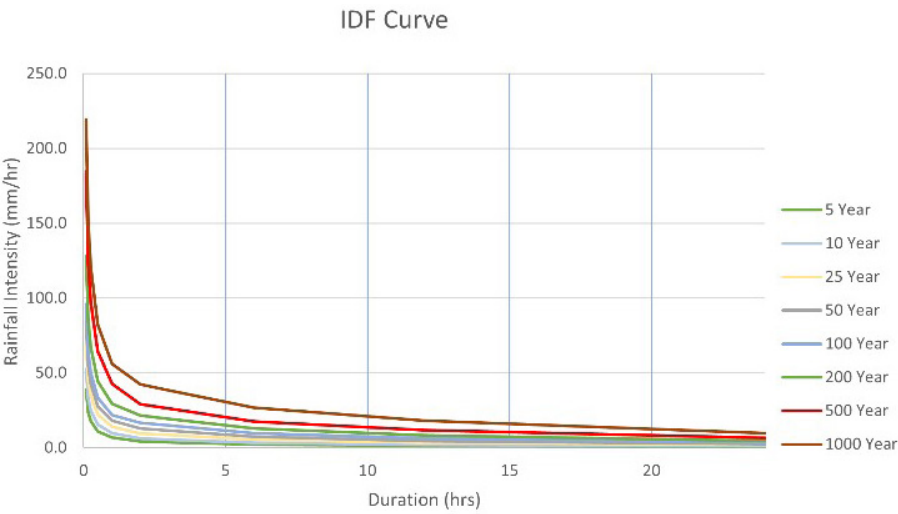


FIGURE 8B

Example of an adjusted  
rainfall totals



## 4. Conclusions

---

This paper presents an innovative method for developing rainfall data in the form of IDF curves for data scarce regions. The innovative method was used to develop rainfall magnitudes for durations of 5 minutes, 10 minutes, 15 minutes, 30 minutes, 1 hour, 2 hours, 3 hours, 6 hours, and 24 hours for the 5-year, 10-year, 25-year, 50-year, 100-year, 200-year, 500-year and 1,000-year return periods for the NEOM Region. The results show spatial variation and mimic the expected orographic effects of the mountains and moisture obtained from the Red Sea and the Gulf of Aqaba.

The IDF data developed for NEOM are subject to the limitations listed in **Section 4.1**. Recommendations to improve the data are listed in **Section 4.2**.

### 4.1 STUDY LIMITATIONS

1. Long records of observed hourly data are not available for the NEOM region, so the project utilized ERA5 Re-analysis data from 1960 to 2021. The ERA5 re-analysis data is by far the longest dataset available and provides spatial variation. However, global re-analysis will not be able to fully capture very small-scale intense convection; although it may have the correct spatial detail, it can lead to underestimation of rainfall intensities of short-duration events. An attempt to overcome this limitation was to conduct the rainfall frequency analysis with the re-analysis data and apply adjustment factors derived from comparing radar data to observed ground data. The resulting analysis provided spatial variation obtained from the re-analysis data.
2. The ERA5 re-analysis data was not available at sub-hourly (5-, 10-, 15-, and 30-minute) durations for the NEOM region. This project, therefore, relied on a previous study of sub-hourly data at Tabuk (Atkins, 2019) to develop regression relationships between the hourly data and sub-hourly data for the region.
3. The record length (61 years) of the ERA5 re-analysis data may not be adequate for estimating rainfall frequencies up to 1000 years. This may negatively impact the accuracy of the estimates for the less frequent events (200 years and higher)



## 4.2 RECOMMENDATIONS FOR IMPROVEMENTS

1. Update the analysis in the future when additional re-analysis data is available. Using a longer length of record will increase the level of accuracy for the less frequent events and will also account for climate change-induced trends.
2. Obtain observed sub-daily rainfall data or gridded data and update the analysis using that data. This will reduce the level of uncertainty resulting from the derivation of the sub-hourly estimates based on another study.
3. Obtain long records of observed ground data at locations other than Tabuk so that adjustment factors can be created for locations across the region. This will increase the level of confidence in the total rainfall estimates across the region.



## References

---

- › Atkins, 2019. Updated Intensity-Frequency-Duration Curves and Storm Drainage Design Guidelines for Saudi Arabia Intensity-Duration-Frequency (IDF) Curves and Design Storm.
- › Becker, A., Finger, P., Meyer-Christoffer, A., Rudolf, B., Schamm, K., Schneider, U., and Ziese, M.: A description of the global land-surface precipitation data products of the Global Precipitation Climatology Centre with sample applications including centennial (trend) analysis from 1901–present, *Earth Syst. Sci. Data*, 5, 71–99, <https://doi.org/10.5194/essd-5-71-2013>, 2013.
- › De Vries et al. (2016) Dynamics of tropical–extratropical interactions and extreme precipitation events in Saudi Arabia in autumn, winter, and spring. *Quarterly Journal of the Royal Meteorological Society*, 142, 1862–1880.
- › Hersbach et al., 2018. ERA5 hourly data on single levels from 1959 to the present. Copernicus Climate Change Service (C3S) Climate Data Store (CDS). (Accessed on 27-Jul-2022), 10.24381/CDs.adbb2d47. <https://cds.climate.copernicus.eu/>
- › Kenawy, A.M., McCabe, M.F. (2016) A multi-decadal assessment of the performance of gauge- and model-based rainfall products over Saudi Arabia: climatology, anomalies, and trends. *International Journal of Climatology*. 36, 2, 656–674.
- › NEOM, 2020. 1.3 Regional Policy Framework: Technical Strategies Report, NEOM Regional Plan, Vol2 by Sherwood and Morphosis, 30 November 2020.
- › USACE, 2019. HEC-SSP Statistical Software Package, User's Manual, Version 2.2. US Army Corps of Engineers Hydrologic Engineering Center, 2019
- › USGS, 2019. Guidelines for Determining Flood Flow Frequency - Bulletin 17C, Version 1.1, England, J.F., Jr., Cohn, T.A., Faber, B.A., Stedinger, J.R., Thomas, W.O., Jr., Veilleux, A.G., Kiang, J.E., and Mason, R.R., Jr., 2019













**Shayne Paynter, PhD, PE, PG**

Water Resources Technical Director, VP,  
Atkins Fellow - Water  
Engineering Services – Water TPO USA  
Tampa, FL, USA

### 03. Water Engineering

---

# Improving the Estimation of Non-Stationary Trends and Return Frequencies for Lake levels

## Abstract

---

One of the most important tools in water management is the accurate forecast of both long-term and short-term extreme values for both flood and drought conditions. Traditional methods of predicting extreme flood and drought frequencies may be highly inaccurate in lake-type systems, especially in the short-term. In the case of lakes, traditional frequency return estimates assume extremes are independent of trending or starting lake stages. However, due to the significant autocorrelation of lake levels, the initial stage can have a significant influence on the severity of a given event. The aim of this research was to accurately identify the direction and magnitude of trends in flood and drought stages and provide more accurate predictions of both long-term and short-term flood and drought stage return frequencies utilizing the generalized extreme value (GEV) distribution with time and starting stage covariates. For all of the lakes studied, significant improvement in the prediction of extremes was obtained with the inclusion of starting lake stage as a covariate. Traditional methods of predicting flood or drought stages significantly overpredict stages when starting lake stages are low and underpredict stages when starting stages are high. The difference between these predictions can be well over one meter, a significant amount in urbanized watersheds in areas of the world with flat topography. Differences of over a meter can mean significant alterations in evacuation or other water management decisions. The methods utilized in this research to determine lake level return period of flood and drought can be applied to nearly any region globally.

## KEYWORDS

Generalized extreme value; Flood frequency; Trend; Lake stage; Drought; Return period



## 1. Introduction

---

One of the most important tools in effective water management is the accurate forecast of both long-term and short-term extreme values for both flood and drought conditions. High water stages associated with flood can cause extensive erosion or property damage while low stages associated with drought affect wildlife, ecology, recreation, and water supply. The vast majority of flood risk evaluation is performed for streams and riverine systems and not lakes. Accurately identifying trends in lake levels can affect long-term decision making, such as forecasting water supply; while improving the prediction of near-term frequency return periods can affect short-term planning, such as the determination of evacuation zones in the face of an approaching hurricane or giving resource managers adequate tools to set annual lake levels. Changes in the general trends of lake, stream, and other surface water bodies have been observed in many parts of the world. These trends may be due to factors such as watershed urbanization, water supply pumping, and morphological changes to the water body itself or climatic changes that impact annual rainfall and distribution and average temperature and evapotranspiration. Paynter and Nachabe (2009) evaluated statistical trends in rainfall distribution across Florida in light of climate change while Paynter et al. (2010) determined that the statistical structure of lakes was altered as lake watersheds become urbanized and groundwater baseflow becomes less of a driver of stage. Traditional methods of trend detection, such as ordinary least squares (OLS) or the Mann-Kendall test, are not aptly suited for hydrologic systems since these systems often exhibit time scale issues, non-normal distributions, seasonality, autocorrelation, inconsistent data collection, missing data, and other complications that render these traditional methods unreliable (Hirsch et al., 1982; Katz et al., 2002). According to Zhang (2004), allowing a GEV parameter covariate significantly outperforms traditional methods of hydrologic trend detection. GEV covariates can also incorporate global trends such as the North Atlantic Oscillation, El Nino/La Nina, and other cycles to improve accuracy.



In a similar fashion to trends, traditional methods of predicting extreme flood and drought frequencies for riverine systems, such as distribution fitting without parameter covariates, may be highly inaccurate in lake-type systems, especially in the short-term. In the case of lakes, traditional frequency return estimates assume extremes are independent of trend or starting lake stages. However, due to the significant autocorrelation of lake levels, the initial stage can have a significant influence on the severity of a given event.

Several studies have analyzed the relation between initial stages, antecedent conditions, and flood return periods in various hydrologic systems. Buchberger (1995) developed near-term flood risk estimates for Lake Erie, United States, based on an autoregressive time series model and the joint occurrence of a normally distributed storm surge and found that conventional frequency analysis underestimates flood risk when starting lake stages are high and overestimates flood risk when starting lake stages are low. Several studies have developed flood return periods dependent upon thresholds of evaporation, rainfall frequency, catchment response time, field capacity storage, catchment storage capacity or lake storage (Struthers and Sivapalan 2007; Kusumastuti et al., 2007; Kusumastuti et al., 2008). Kusumastuti (2008) found that the antecedent lake storage was the dominant control on flood frequency and magnitude.

FIGURE 1

Location map of  
study lakes



Trend identification in lake levels utilizing the GEV distribution as well as the development of variable return periods based on starting lake stages are a practical application of GEV distribution theory that has not yet been applied to lakes. The objectives of this research in regards to lake levels were to 1) accurately identify the direction and magnitude of trends in flood and drought stages, and 2) provide more accurate predictions of both long-term and short-term flood and drought stage return frequencies utilizing GEV with time and starting stage covariates.



## 2. Materials and Methods

---

### 2.1. LAKE INFORMATION AND DATA

Lakes were selected with at least 50 years of data across the southwestern portion of Florida that were mostly anthropogenically unaltered, (i.e., from significant dredging, placement of berms, pumping, installation of major control structures, etc.) in such a way that would significantly change the time series signature and, hence, the underlying distribution. Given the degree of urbanization across Florida, it is not possible to find completely unaltered lakes with sufficient data. However, four lakes, including Lake Arbuckle, Lake Carroll, Lake Trafford, and Lake Weohyakapka (**Figure 1**) that are relatively unaltered were utilized. Lake Trafford is depicted in **Figure 2**.

FIGURE 2

---

Lake Trafford





## 2.2. GEV DISTRIBUTION

Trends in lake levels and return level frequencies were defined utilizing extreme value models. The main variables modeled were the annual maximum and minimum lake levels, and the flood and drought stages. In order to analyze any trends, distribution parameters were allowed to vary with time. Because lake levels exhibit substantial autocorrelation, it is surmised that annual starting lake levels have a significant impact on the distribution of annual extremes; therefore, the GEV parameters were also allowed to vary with initial stage. The starting lake stage was taken as the water level on January 1 of any given year. The time and starting lake stage covariate models were compared to the original distribution model to determine if a statistically significant better fit was achieved. If covariates do significantly improve the fit, the distribution itself is potentially changing as these covariates change. Changing distribution parameters with time or starting stage allows for the distribution to be non-stationary and also gives an estimate on the rate of change.

The GEV is the generalized form of three commonly applied extreme value distributions: the Gumbel, the Frechet, and the Weibull. The GEV is applicable to variables of block maxima, where the blocks are equal divisions of time. The GEV cumulative distribution function is given by:

$$F(x) = \exp \left\{ - \left[ 1 + \xi \left( \frac{x - \mu}{\sigma} \right) \right]^{-1/\xi} \right\} \quad (1)$$

where  $x$  is the random variable,  $\mu$  is the location parameter,  $\sigma$  is the scale parameter, and  $\xi$  is the shape parameter, and  $1 + \xi(x - \mu)/\sigma > 0$ . GEV distribution parameters are determined using maximum likelihood estimation. The log-likelihood for the GEV distribution with parameters that are a function of time  $t$  or starting lake stage  $s$  is given by:

$$l(\mu, \sigma, \xi) = - \sum_{i=1}^m \left\{ \log \sigma(t, s) + (1 + 1/\xi(t, s)) \log \left[ 1 + \xi(t, s) \left( \frac{x_{t,s} - \mu(t, s)}{\sigma(t, s)} \right) \right] + \left[ 1 + \xi(t, s) \left( \frac{x_{t,s} - \mu(t, s)}{\sigma(t, s)} \right) \right]^{-1/\xi(t, s)} \right\}$$

given that  $1 + \xi(t, s) \left( \frac{x_{t,s} - \mu(t, s)}{\sigma(t, s)} \right) > 0$  for all  $t = 1, \dots, m$  (Coles, 2004) (2)



For purposes of this research, model 1 is the GEV distribution with parameters  $\mu$ ,  $\sigma$  and  $\xi$  held constant in a traditional approach. Distribution parameters for model 1 were estimated for each lake and evaluated the goodness-of-fit with the Kolmogorov-Smirnov test statistic at the 95% significance level. For model 2, the location parameter of model 1 was allowed to vary with time or starting stage or both to investigate the presence of trends and determine if model 1 could be improved. It should be noted that covariates could be assigned to any of the three GEV parameters; however, the location parameter is generally most sensitive to non-stationarities and, given the difficulty in estimating the shape parameter, it is impractical to model this parameter as unstationary (Coles 2004). Therefore, the location parameter was the only parameter explicitly modeled with covariates; however, the scale parameter was varied for comparison purposes. Model 2 is therefore a submodel of model 1 with

$$\mu = a + by \quad (3)$$

where  $y$  is either the time in years or the starting lake stage and  $a$  and  $b$  are constants. Model 3 is a submodel of model 2 with

$$\mu = c + dt + es \quad (4)$$

where  $t$  is the time in years,  $s$  is the starting lake stage and  $c$ ,  $d$ , and  $e$  are constants. Once parameters were estimated for all three cases, the models were compared to determine if the time and/or starting lake stage covariate give a statistically significant better fit. In order to test one model against another, the likelihood ratio test was utilized. If  $l_1$  and  $l_2$  represent the maximized log-likelihoods of the models to be compared, then a deviance statistic is given by:

$$D = 2\{l_2 - l_1\} \quad (5)$$

Model 2 will be compared to model 1 while model 3 will be compared to both model 1 and model 2. In cases where a model with parameter covariates demonstrated a significantly better fit, fits were further investigated by examining standard quantile plots for visual confirmation of the fit improvement. However, because model 1 is stationary, and models 2 and 3 are non-stationary, and parameters are varying at each observation, all models were transformed to the standard Gumbel distribution given by (Coles 2004):

$$Z_t = \frac{1}{\xi(t,s)} \log \left\{ 1 + \xi(t,s) \left( \frac{X_t - \mu(t,s)}{\sigma(t,s)} \right) \right\} \quad (6)$$

Quantile-quantile plots were developed for these transformed standardized variables. If models 2 or 3 demonstrate an improved fit, it means estimated frequency return periods are changing with time or starting lake stage. Because low frequency events are of main interest, quantile-quantile plots were utilized to focus on the fit in the extreme end of the distribution. If an adequate fit in this region was not confirmed via the plots, the simplest model that adequately predicted extremes was selected. Return level plots for the most appropriate model for both flood and drought were developed at each lake. Estimates of quantiles for the return level plots are given by:

$$q_{x,p} = \begin{cases} \mu(t,s) + \frac{\sigma}{\gamma} [(-\ln(1-p))^{-\gamma}], & \gamma \neq 0 \\ \mu(t,s) - \sigma \ln(-\ln(1-p)), & \gamma = 0 \end{cases} \quad (7)$$

where  $q$  is the quantile estimate for lake stage  $x$  at frequency  $p$  (Beirlant et al., 2004).

### 3. Results and Discussion

A summary of the data utilized is given in Table 1. Specifically, the number of years of record, maximum, minimum, and average stages and variance are provided. A plot of the maximum, minimum, and starting stage for Lake Weohyakapka is provided in Figure 3. From the table, the standard deviation in lake levels is consistently near 0.3m. The average difference between the maximum and minimum for the lakes analyzed is 2.13m. Given the flat topography of west-central Florida and other similar regions, relatively small differences in water level fluctuations can inundate large areas and impact structures that are routinely set as low as 0.3m above expected high water marks. From inspection of the figures, it appears likely that annual starting stage is correlated with both annual maximum flood and minimum drought stages as the starting stage approximately parallels both the flood and drought stages. The fits of the lake stages for flood and drought are given in Tables 2 and 3, respectively, for all GEV models. The Kolmogorov-Smirnov values were well within the 95% test statistic for the no-covariate fits, indicating the fits are acceptable.

TABLE 1

Lake data summary

Lake	Period of Record	Average (m) (NGVD*)	Maximum (m) (NGVD*)	Minimum (m) (NGVD*)	Standard Deviation (m)
Arbuckle	1942-2008	16.35	17.79	15.59	0.36
Carroll	1946-2003	10.76	12.10	9.41	0.34
Trafford	1941-2007	5.98	6.95	4.85	0.29
Weohyakapka	1958-2008	18.64	19.46	17.95	0.24

\*National Geodetic Vertical Datum

FIGURE 3

Lake Weohyakapka  
stage data

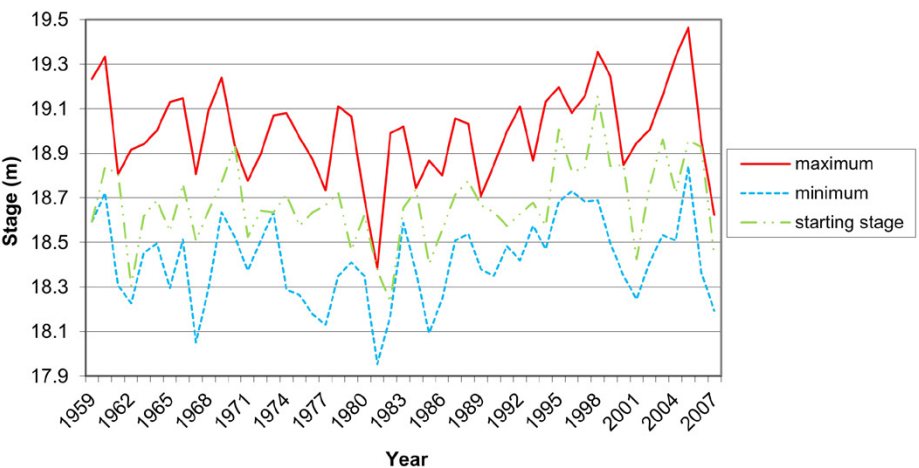




TABLE 2

GEV flood parameter  
summaryy

Lake	Location $\mu$	$\mu$ -time covariate*	$\mu$ -starting stage covariate*	Scale $\sigma$	Shape $\xi$	Likelihood ratio**
No covariate (model 1)						
Arbuckle	16.831	N/A	N/A	0.347	-0.286	
Carroll	10.984	N/A	N/A	0.300	-0.147	
Trafford	6.285	N/A	N/A	0.193	-0.191	
Weohyakapka	18.928	N/A	N/A	0.214	-0.335	
Time covariate (model 2)						Model 2/Model 1
Arbuckle	17.085	-0.007 (0.002)	N/A	0.336	-0.385	10.301
Carroll	11.176	-0.006 (0.002)	N/A	0.282	-0.149	6.567
Trafford	6.301	-0.000 (0.001)	N/A	0.193	-0.192	0.090
Weohyakapka	18.876	0.002 (0.000)	N/A	0.216	-0.386	1.204
Starting stage covariate (model 2)						Model 2/Model 1
Arbuckle	8.954	N/A	0.484 (0.191)	0.343	-0.387	8.203
Carroll	3.299	N/A	0.712 (0.074)	0.165	0.194	45.895
Trafford	4.015	N/A	0.376 (0.198)	0.179	-0.115	4.457
Weohyakapka	5.691	N/A	0.710 (0.015)	0.192	-0.464	
Time and starting stage covariates (model 3)						Model 3/Model 1:Model 3/Model 2
Arbuckle	13.178	-0.007 (0.001)	0.240 (0.019)	0.335	-0.488	16.626/8.422
Carroll	3.470	-0.000 (0.001)	0.697 (0.078)	0.169	0.169	45.782/0.113
Trafford	3.858	-0.001 (0.001)	0.407 (0.204)	0.177	-0.109	4.898/0.441
Weohyakapka	6.341	-0.000 (0.000)	0.676 (0.000)	0.190	-0.449	17.081/0.649

\*Standard Errors of slope parameters are noted in parenthesis.

\*\*At the 95% confidence interval, a maximum likelihood ratio of greater than 3.842 for model 2/model 1 or model 3/model 2 and 5.992 for model 3/model 1 indicates a significantly better fit. The model 2/model 1 and model 3/model 1 ratios were also compared to determine if the additional degree of freedom improves the fit. Selected models are bolded.

TABLE 3

GEV drought parameter  
summary

Lake	Location $\mu$	$\mu$ -time covariate*	$\mu$ -starting stage covariate*	Scale $\sigma$	Shape $\xi$	Likelihood ratio**
No covariate (model 1)						
Arbuckle	15.844	N/A	N/A	0.182	-0.150	
Carroll	10.304	N/A	N/A	0.409	-0.395	
Trafford	5.554	N/A	N/A	0.301	-0.504	
Weohyakapka	18.354	N/A	N/A	0.194	-0.326	
Time covariate (model 2)						Model 2/Model 1
Arbuckle	15.915	-0.002 (0.001)	N/A	0.181	-0.169	2.484
Carroll	10.561	-0.008 (0.002)	N/A	0.380	-0.455	11.005
Trafford	5.498	0.001 (0.002)	N/A	0.295	-0.465	0.549
Weohyakapka	18.293	0.0026 (0.001)	N/A	0.193	-0.363	2.023
Starting stage covariate (model 2)						Model 2/Model 1
Arbuckle	10.414	N/A	0.335 (0.000)	0.154	-0.383	7.536
Carroll	0.117	N/A	0.947 (0.076)	0.200	-0.264	71.923
Trafford	-0.804	N/A	1.055 (0.140)	0.200	-0.323	39.937
Weohyakapka	3.855	N/A	0.778 (0.007)	0.149	-0.445	
Time and starting stage covariates (model 3)						Model 3/Model 1:Model 3/Model 2
Arbuckle	9.441	-0.001 (0.000)	0.396 (0.334)	0.166	-0.276	21.753/14.217
Carroll	0.439	-0.001 (0.002)	0.921 (0.085)	0.198	-0.259	72.413/0.489
Trafford	-1.519	0.000 (0.000)	1.177 (0.096)	0.177	-0.329	34.432/5.505
Weohyakapka	15.839	0.002 (0.000)	0.134 (0.000)	0.176	-0.430	8.160/23.884

\*Standard Errors of parameters are noted in parenthesis.

\*\*At the 95% confidence interval, a maximum likelihood ratio of greater than 3.842 for model 2/model 1 or model 3/model 2 and 5.992 for model 3/model 1 indicates a significantly better fit. The model 2/model 1 and model 3/model 1 ratios were also compared to determine if the additional degree of freedom improves the fit. Selected models are bolded.

### 3.1. TREND ANALYSIS

For Lake Carroll, the model 2 location parameter for flood stages, which yields an estimate of the relation between lake stage and time  $t$  in years, indexed as 1, 2, 3... etc. years into the future, is given by:

$$11.176 - 0.006t$$

And the model 2 location parameter for drought stages is given by:

$$10.561 - 0.008t$$

Although the maximum likelihood ratio for both trends is substantially larger than the 95% confidence limit threshold, the actual change in flood or drought stage is relatively small, 0.006m and 0.008m of decrease per year that the trend is extended into the future. This slight trend is visually confirmed in **Figure 2**. For Lake Arbuckle, the model 2 location parameter for flood stages is given by:

$$17.085 - 0.007t$$

The trend is again downward and of similar order, a decrease of 0.007m per year. The lakes studied are relatively unaltered in regards to excessive pumping, dredging, management or other mechanisms that may induce dramatic trends. Furthermore, Paynter and Nachabe (2009) determined that the rainfall patterns in the southwest Florida region do not exhibit significant trends that would correlate to changes in lake levels. Lakes Arbuckle, Trafford, and Weohyakapka are fairly undeveloped when compared to Lake Carroll, which is highly urbanized. Although many lakes in Florida have demonstrated significant trends due to pumping or anthropogenic change, it appears lakes left in a fairly natural state such as the four studied for this research exhibit slight but statistically significant trends in the case of Lakes Carroll and Arbuckle or no trends in the cases of Lakes Trafford and Weohyakapka.

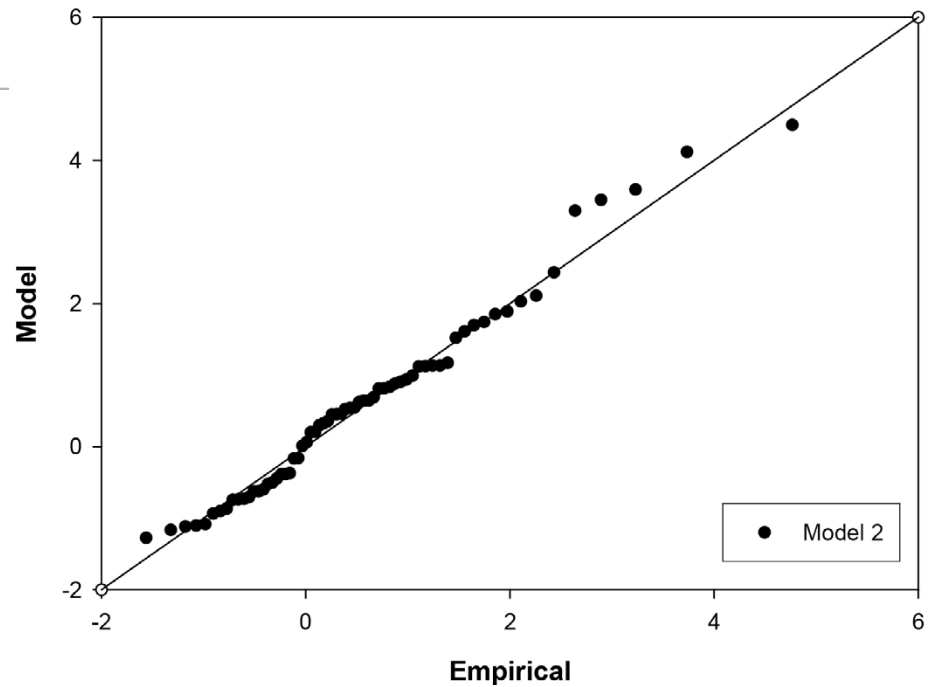
### 3.2. STARTING STAGE ANALYSIS

#### 3.2.1. FLOOD RETURN PERIOD

According to the maximum likelihood ratios, model 2, with a starting stage covariate, is most appropriate for Lakes Carroll, Trafford, and Weohyakapka while model 3 is most appropriate for Lake Arbuckle. It should be noted that the magnitude of the likelihood ratio is proportional to the degree of improvement of the fit; the model 2 ratios are generally high. Only Lake Arbuckle demonstrated a statistically significant improvement in fit when covariates for both time and starting stage are included. However, as the trend component of model 3 is negligible, the simpler model 2 was selected. The Lake Arbuckle (**Figure 4**) quantile-quantile plot demonstrates an adequate fit for model 2. Quantile-quantile plots for Lakes Carroll, Trafford, and Weohyakapka also demonstrated adequate model 2 fits.

FIGURE 4

Lake Arbuckle flood  
stage standardized  
residual quantiles



With the exception of Lake Carroll, in most of the quantile-quantile plots for flood, the fit breaks down at the extreme end for all models. This is partly due to these points representing hurricanes or tropical storms that are not part of the same distribution as normal rainfall events and partly due to extrapolating extreme events with 50 years of data. After evaluating both the maximum likelihood ratios and the quantile-quantile plots, we selected model 2 for all four lakes in terms of flood stage. The location parameter, which yields an estimate of the relation between starting stage and flood stage, is given by the following for Lakes Arbuckle, Carroll, Trafford, and Weohyakapka, respectively, for starting stage  $s$ :

$$8.954 + 0.484s$$

$$3.299 + 0.712s$$

$$4.015 + 0.376s$$

$$5.691 + 0.710s$$

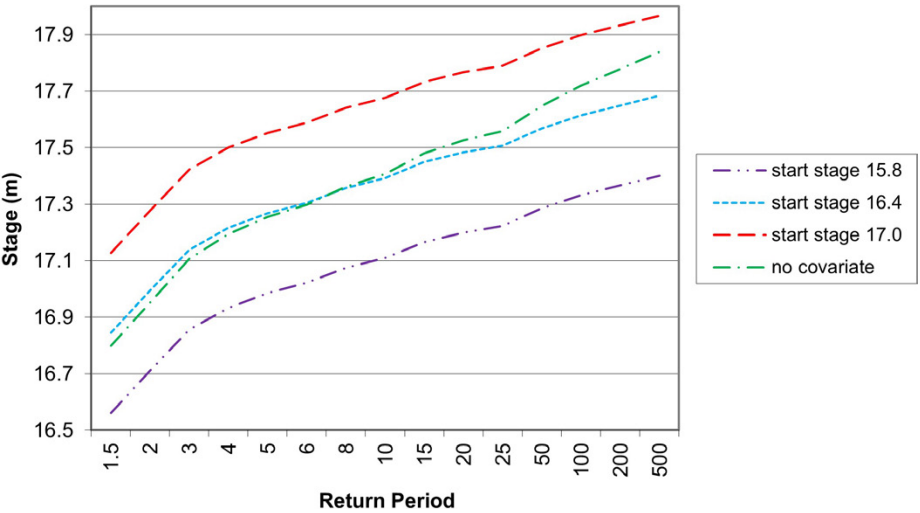
For every unit change in starting stage, there is a substantial change ranging from 0.376 to 0.712m in the flood stage for a given year, indicating a very high degree of correlation. **Figure 5** gives the model 2 flood return period for Lake Arbuckle associated with the maximum, minimum, and average starting stage as well as the return period associated with no covariate. For each lake, the return period associated with the average starting stage is relatively close to the return period associated with no covariate. For Lakes Arbuckle, Carroll, and Weohyakapka, there is some divergence between these two curves towards the larger return periods.



At Lakes Arbuckle and Carroll, this is likely due to the fact that these lakes exhibit some trends and since the starting stage should correlate to any trends, the inclusion of the starting stage covariate improves the fit and causes divergence from the fit without a covariate. The flood return period associated with no covariate is bounded by that associated with the maximum and minimum starting stage. In years with a low starting stage, traditional frequency analysis overpredicts the 100-year flood by 108.3%, 129.4%, 75.9%, and 179.2% of standard deviation for Lakes Arbuckle, Carroll, Trafford, and Weohyakapka, respectively. In years with a high starting stage, traditional frequency analysis underpredicts the 100-year flood by 50%, 232.4%, 69.0%, and 91.7% of standard deviation for the same lakes. As such there is a 0.57m, 1.22m, 0.42m, and 0.65m difference, respectively, between the 100-year return period stage for the maximum and minimum starting lake stage covariate. Given the flat topography in Florida and other similar regions, a difference of as much as 1.22m can mean a substantial increase in the extent of flooding and potential number of structures flooded.

**FIGURE 5**

Lake Arbuckle flood return frequencies with and without starting lake stage covariates





Since more area is available at consistently higher elevations of a lake, it takes more runoff or baseflow volume to cause a unit rise in stage at higher lake elevations. Because of this, it would be expected that in a lake left in its natural stage that return period curves would flatten out at more extreme frequencies. However, once a lake basin is urbanized, the watershed infilled with construction and management structures installed, it is difficult to consistently predict the shape of these curves. Lakes Arbuckle, Trafford, and Weohyakapka are relatively undeveloped and they demonstrate the expected flattening of the return period curves at higher frequencies. Lake Carroll is the most urbanized and it shows some steepening of the return period curves at extreme events.

### 3.3. DROUGHT RETURN PERIOD

According to the maximum likelihood ratios, model 2 (with a starting stage covariate) is most appropriate for Lakes Carroll, Trafford, and Weohyakapka while model 3 is most appropriate for Lake Arbuckle. As in the flood analysis, the trend component is quite small and the simpler model 2 was deemed appropriate. Similar to the flooding case, the likelihood ratios for model 2 are quite high, indicating that model 2 explains substantially more of the variation. The quantile-quantile plots for Lakes Arbuckle, Carroll, Trafford, and Weohyakapka (**Figure 6**) indicate an adequate fit for model 2. As with the flood quantiles, there is divergence between the model and empirical data at the extremes. This is likely due to longer time-scale cycles, such as La Nina, that cause excessively dry years and are not explicitly included in the models; model 2 should capture some, but not all, of these longer cycles with the inclusion of starting stage. Some of the fit breakdown is also due to extrapolating events greater than the 50-year from 50 years of data. After evaluating both the maximum likelihood ratios and the quantile-quantile plots, we selected model 2 for all four lakes. The location parameter associated with the most appropriate model for each lake is given by the following for Lakes Arbuckle, Carroll, Trafford, and Weohyakapka, respectively, for starting stage  $s$ :

$$10.414 + 0.335s$$

$$0.117 + 0.947s$$

$$-0.804 + 1.055s$$

$$3.855 + 0.778s$$

As in the flood case, for every unit change in starting stage, there is a substantial change in the drought stage for that year, in this case ranging from 0.335m to 1.055m. **Figure 7** depicts the drought return period for Lake Carroll associated with the maximum, minimum, and average starting stage as well as the return period associated with no covariate. Similar to the flood return period case, the return period associated with no covariate is bounded by that associated with the maximum and minimum starting stage and approximately parallels the return period associated with the average starting stage covariate. In years with a low starting stage, traditional frequency analysis overpredicts the 100-year drought by 41.4%, 105.9%, 158.6%, and 104.2% of standard deviation for Lakes Arbuckle, Carroll, Trafford, and Weohyakapka, respectively. In years with a high starting stage, traditional frequency analysis underpredicts the 100-year drought by 66.7%, 373.5%, 251.7%, and 191.7% of standard deviation for the same lakes. As such there is a 0.39m, 1.63m, 1.19m, and 0.72m difference, respectively, between the 100-year return period stage for the maximum and minimum starting lake stage covariate. In similar fashion to flood stages, it is expected that drought return period curves would flatten at more extreme return periods since there are more water loss mechanisms at higher lake stages. At lower stages, the only method of water loss may be evapotranspiration or recharge to the ground. All of the four lake drought return curves follow this general pattern.

**FIGURE 6**

---

Lake Weohyakapka drought  
stage standardized  
residual quantiles

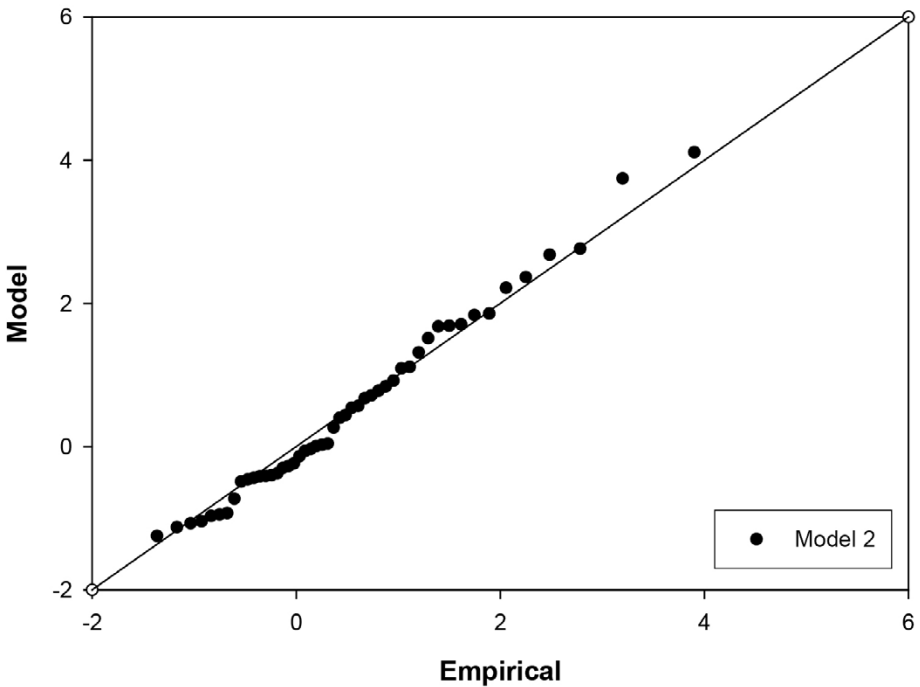
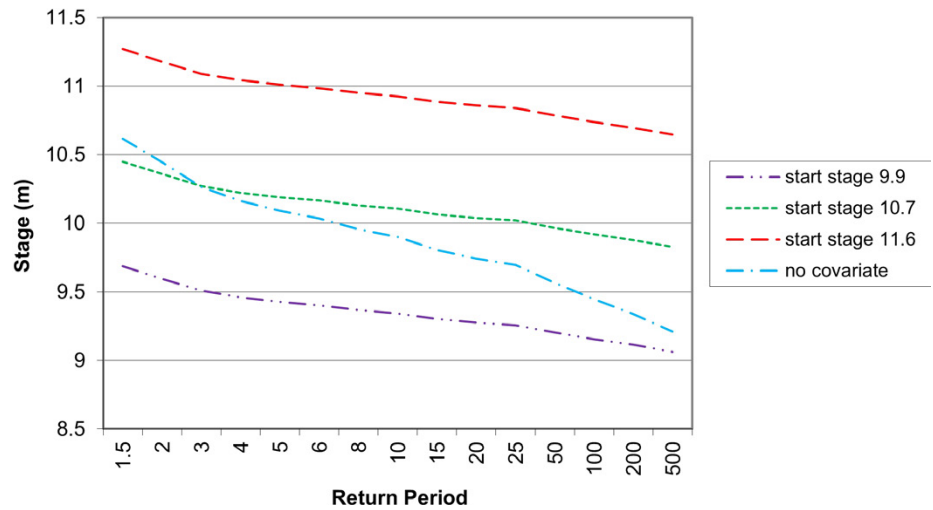


**FIGURE 7**

Lake Carroll drought  
return frequencies with  
and without starting  
lake stage covariates



There appears to be no correlation in the difference between flood stages and drought stages for the minimum and maximum starting lake stages within each lake (i.e., a small difference in the Lake Carroll flood stage associated with the maximum and minimum starting stage does not indicate a small difference in the drought stage associated with the maximum and minimum starting stage). This is likely due to different physical dynamics operating in the flood and drought cases. Flood stages are generally controlled by some management mechanism (i.e., a weir, culvert, gate, etc.) while drought stages are largely uncontrolled other than natural losses such as evapotranspiration or seepage to the ground. Furthermore, at extreme flood stages, the basin morphology may change relative to the lake at lower stages (i.e., higher stages may be flatter than at lower stages, a basin popoff to another basin may be reached or housing construction may have significantly altered the historic basin by infill).

The methodology employed in this research provides a robust means to estimate the direction and magnitude of lake trends that is robust despite the inherent difficulties in determining trends in hydrologic data. The methodology also allows for a more accurate prediction of flood and drought return frequencies that can be applied globally and allows for incorporation of non-stationary trends associated with rapidly changing climate worldwide.



## **Acknowledgements**

---

This paper was adapted and updated from the original publication: Shayne Paynter, Mahmood Nachabe. Use of generalized extreme value covariates to improve estimation of trends and return frequencies for lake levels. Journal of Hydroinformatics, 1 January 2011; 13 (1): 13–24. doi: <https://doi.org/10.2166/hydro.2010.077>.



## References

---

- › EBeirlant J, Goegebeur Y, Segers J, Teugels J (2004) Statistics of Extremes. John Wiley & Sons, Limited
- › Buchberger S (1995) Conditional frequency analysis of autocorrelated lake levels. Journal of Water Resources Planning and Management 121: 158-170
- › Coles S (2004) An introduction to statistical modeling of extreme values. Springer-Verlag London Limited
- › Hirsch R, Slack J, Smith R (1982) Techniques of trend analysis for monthly water quality data. Water Resources Research 18: 107-121
- › Katz R, Parlange M, Naveau P (2002) Statistics of extremes in hydrology. Advances in Water Resources 25: 1287-1304
- › Kusumastuti D, Struthers I, Sivapalan M, Reynolds D (2007) Threshold effects in catchment storm response and the occurrence and magnitude of flood events: implications for flood frequency. Hydrology and Earth System Sciences 11: 1515-1528
- › Kushumastuti D, Sivapalan M, Struthers I, Reynolds D, Murray K, Turlach B (2008) Thresholds in the storm response of a catchment-lake system and the occurrence and magnitude of lake overflows: implications for flood frequency. Water Resources Research 44: 1-15
- › Paynter S and Nachabe M (2009) Regional scale spatio-temporal consistency of precipitation variables related to water resource management and planning. Meteorological Applications 16: 413-423
- › Paynter S, Nachabe M and Yanev G (2010) Statistical Changes of Lakes in Two Rapidly Changing Watersheds. Water Resources Management 25: 21-39
- › Struthers I and Sivapalan M (2007) A conceptual investigation of process control upon flood frequency: role of thresholds. Hydrology and Earth Systems Science 11 1405-1416
- › Zhang X, Zwiers F, Li G (2004) Monte Carlo experiments on the detection of trends in extreme values. Journal of Climate 17: 1945-1952





**Campbell Minogue**

Chartered Mechanical Engineer,  
Tunnel Ventilation and Fire Life Safety  
Engineering Services – Infrastructure UK  
Epsom, UK



**Gary Clark**

Chief Engineer, Tunnel Ventilation and Fire  
Life Safety  
Engineering Services – Infrastructure UK  
Epsom, UK



**Christian Perez**

Associate Tunnel Ventilation Engineer,  
Tunnel Ventilation and Fire Life Safety  
Engineering Services – Infrastructure UK  
Epsom, UK

## 04. Tunnel Engineering

---

# Designing Accessible Inverts to Meet the Requirements of Tunnel Owners and Operators

### Abstract

---

As new road tunnels are constructed around the world to take the strain off existing over capacity routes, and with the risks of climate change requiring ever greater action, the need to maximise the operational efficiency of assets is greater than ever. Decisions taken during the early stages of design have a significant impact in determining the operational efficiency of an asset. Therefore, understanding the factors which influence operational carbon, and minimising carbon in design are key to reducing operating costs and whole life carbon footprint. This paper aims to provide an approach to considering these factors and makes recommendations for M&E design to meet the requirements of tunnel owners and maximise operational efficiency.

### KEYWORDS

Design; Operational efficiency; Sustainability



## 1. Introduction

---

Accessing and maintaining road tunnel mechanical and electrical (M&E) assets typically requires a night-time tunnel closure as many of the assets are located in places which cannot be safely reached while the tunnel traffic is live. Closing the tunnel results in lost time for road users and, in some cases, lost revenue for tunnel operators; therefore, tunnel owners, and their designers, are continuously looking for ways to improve the access to their assets to enhance the operational efficiency of the tunnel. Relocating M&E equipment outside of the main tunnel bore, into a space which is safely accessible while the tunnel is live, can deliver significant operational cost savings as well as reduce risks to health and safety of the public and maintainers alike.

The lifetime operational cost and the inherent risks associated with maintaining an asset are largely determined by decisions made in the early stages of design. These decisions will determine how, when, and where equipment is accessed and maintained, therefore defining the costs and risk associated. This paper will explore how the tunnel design can be optimised for operation and maintenance ease and cost efficiency, while ensuring risks are minimised and safety assured.



## 2. Requirements of Tunnel Owners and Operators

---

Understanding the requirements of tunnel owners and operators allows us to pay particular focus to certain areas of our design that will support them to deliver against their operational objectives.

### 2.1 KEY REQUIREMENTS

Tunnel owners and operators have several key requirements in mind when procuring or operating their tunnel, these are:

1. Maximised tunnel lane availability
2. Maximised asset resilience
3. Maximised asset reliability
4. Minimised tunnel footprint and cost
5. Maximised ease of accessing/maintaining equipment

These requirements will enable them to achieve the maximum operating efficiency from their tunnel by reducing unplanned closures and maintenance costs, and maximising vehicle throughput. To meet these requirements, tunnel designers must consider these needs from the outset and continually refine and improve their design by working closely with stakeholders who will ultimately own and operate the asset.

#### 2.1.1 TUNNEL LANE AVAILABILITY

Tunnel lane availability is directly linked to the minimum operating requirement (MOR) for a tunnel and is a product of the reliability and resilience of the systems installed within the tunnel. Tunnel lane availability is a key metric for owners and operators who want to ensure tunnel users, some of whom will be toll paying, can use the tunnel as much as is practicable.

#### 2.1.2 ASSET RESILIENCE

Asset resilience may be defined as the ability of an asset to recover its MOR level following a fault/incident. The quicker the MOR can be restored, the shorter any period of tunnel downtime will be, and hence the lesser the impact on the lane availability. Maximising the resilience of an asset will therefore ensure the impact on tunnel availability is minimised can be achieving by reducing the time needed to carry out any maintenance or repair activities.

The resilience of an asset is influenced not only by the design of the tunnel (e.g., by interleaved power supplies, duty/standby PLCs, and fire pumps, etc.) but also by the ability of the tunnel operator to maintain and service equipment within the tunnel.

Regular maintenance and servicing of systems will reduce the likelihood of failures or issues which can result in a breach of the MOR and the tunnel being closed. The outcome of these actions and design choices results in a reliable asset which meets the availability requirements of the owner.

#### **2.1.3 ASSET RELIABILITY**

Asset reliability is the ability of an asset to remain operational without fault (i.e., the more reliable an asset, the less system faults it will experience). By maximising the reliability, you minimise the number of times when a fault will occur which results in a breach of MOR, therefore minimising the number of unplanned tunnel closures/maintenance interventions required.

Reliability is driven by a number of factors, some of which we cannot control (i.e., a random fault can occur at any time irrespective of actions we take). However, we can minimise the likelihood of a fault occurring by selecting high quality components to install and crucially ensuring they are regularly serviced and maintained.

#### **2.1.4 REDUCED TUNNEL FOOTPRINT AND COST**

Tunnel footprint is a key driver of construction costs, as well as having an impact on operating costs, as, generally, a larger tunnel will require more equipment and maintenance to service it. Tunnel footprint is driven primarily by the kinematic vehicle envelope and the evacuation route requirements; however, the need to locate certain M&E equipment around the tunnel walls and in plant rooms/cross passages between the bores can become a driver of the overall footprint.

The design and location of technical systems such as pumped drainage, electrical distribution, fixed fire fighting systems (FFFS), fire mains, and small M&E systems and lighting must be optimised and developed to ensure that the most efficient and compact design is produced.

#### **2.1.5 MAXIMISED EASE OF ACCESSING/MAINTAINING EQUIPMENT**

During operation of the tunnel, faults may arise on equipment whereby the maintenance team needs to attend to the equipment and reset a breaker, replace a fuse or investigate further to determine the cause of the fault. Ensuring access to equipment is as easy as possible will support the speedy recovery of the MOR following a fault, representing a resilient asset with a high level of lane availability.

In addition to the ease of repairing faults during operation, tunnel operators want the maintenance and servicing of equipment to be as easy as possible, minimising risk to the public and workers while maximising reliability and tunnel availability.



### 3. Typical M&E Equipment Locations

---

#### 3.1 CONSIDERATIONS

When constructing a road tunnel, deciding where the M&E equipment is to be located will impact both operating costs and capital equipment renewal costs. The harsh air environment within a tunnel traffic bore will corrode and degrade M&E systems quicker than if they were located away from the pollutants of vehicle exhausts. Hence the systems will require more regular maintenance and repair/replacement when located in an unpleasant/dirty environment versus a cleaner one.

Locating the M&E equipment in a place whereby to safely access it, there must be an interruption to traffic of some kind, reduces the ease and regularity of maintenance, and hence increases costs. There are also increased health and safety risks associated with this approach to both the operator/maintainer and the public.

#### 3.2 WITHIN THE MAIN TRAFFIC BORE

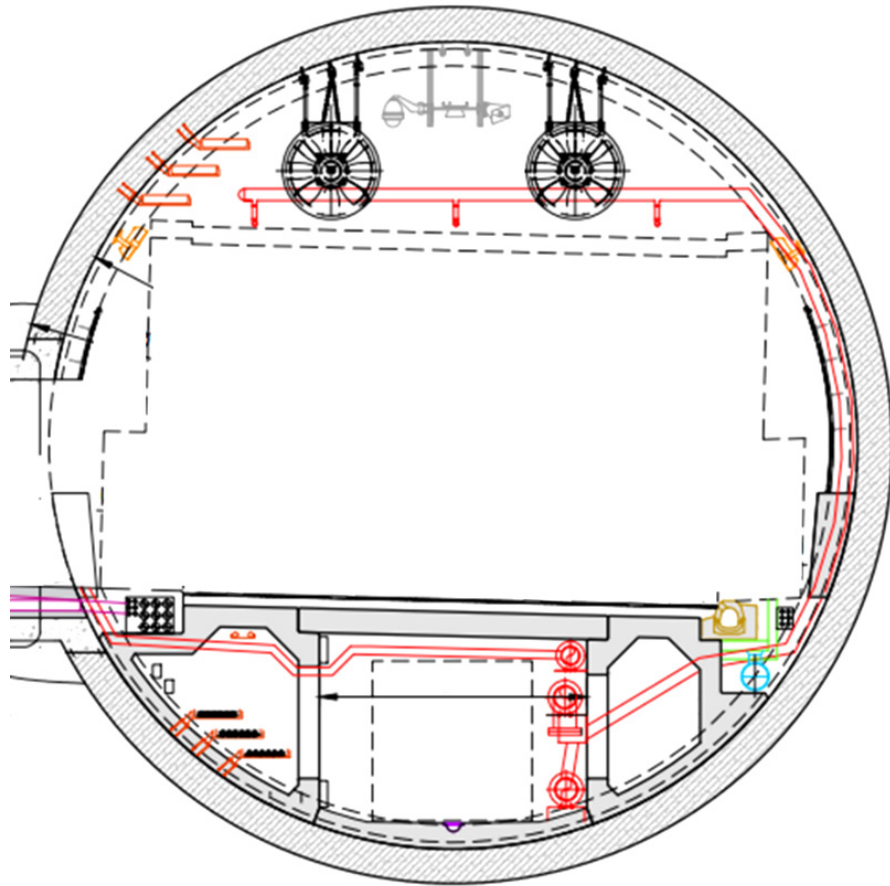
Some M&E equipment must be located within the main traffic bore in order to perform its primary function. Examples of such equipment items includes fire detection systems, air quality monitoring, jet fans, traffic signage, CCTV cameras, and tunnel and emergency lighting. These systems typically provide a safety critical function and rely on transmitting information between the tunnel operator and the tunnel user, or performing a direct action in case of an emergency (e.g., ventilation, FFFS).

The location of these equipment items is largely fixed and cannot be altered to extend the lifespan or reduce the maintenance requirements for these systems. **Figure 1** below shows a typical bored tunnel cross section and the location of some of these M&E systems within the main traffic bore.



**FIGURE 1**

Typical bored tunnel  
cross section including  
accessible invert



### 3.3 WITHIN CROSS PASSAGES

Many tunnels utilise cross passages between the two tunnel bores as part of their design for evacuation in case of an emergency. These spaces also provide a useful area within which to locate M&E equipment which support the systems required to be in the main traffic bore such as lighting drivers, traffic signage controls, CCTV systems, FFFS section valves, jet fan starters, etc. These support systems do not need to be installed within the main traffic bore; hence, locating them elsewhere can extend their lifespan by taking them out of the polluted air and save space within the main bore by utilising the excess space created in the cross passages.

The location of some M&E equipment items is sensitive to their proximity to the component which they are supporting (e.g., LED lighting drivers must be located within a certain distance of the luminaire they are driving, similarly with jet fan starters and traffic signage controls). However, their location within cross passages limits their access for maintenance or servicing as via the main traffic bore only (unless there are additional service tunnels/shafts).



### **3.4 RELOCATING MECHANICAL AND ELECTRICAL EQUIPMENT**

Relocating the equipment items which are located within the cross passages to a place which is accessible via a route other than the main traffic bore enables access and maintenance to these systems at any time, regardless of the traffic conditions in the main bore. This can also provide health and safety benefits by reducing risks to workers and the public, as well as further benefits from extended operating life due to more regular maintenance and servicing of equipment.

## **4. Accessible Tunnel Inverts: Design and Construction**

---

The requirements of tunnel owners and operators, set out in section one, highlight the need for creative and innovative solutions to tunnel design. The construction and use of underdeck spaces within tunnels presents a key opportunity to not only reduce tunnel footprint and construction costs, but to enhance equipment lifetimes, reduce operating costs, and increase tunnel availability, reliability, and resilience.

The design and use of underdeck spaces within tunnels is not a new concept, but the benefit of them is often only taken when the tunnel diameter is sufficient that they can be easily designed, constructed, and operated. Furthermore, we must ensure renewed focus is given to relocating as many M&E systems outside the main tunnel bore and cross passages as possible to support the objectives of owners and operators and to reduce the carbon footprint of our assets.

Due consideration should be given to situations where the inclusion of an accessible invert within the tunnel design does not necessarily appear feasible at the project conception but may become so as the design progresses and work is done to develop a solution. These circumstances are likely to result in generating the largest possible benefits to operational efficiency versus a baseline solution without an accessible invert.

### **4.1 FEASIBILITY OF CONSTRUCTION**

When designing a new road tunnel, dependant on the construction method being used and the location and requirements for the tunnel, it may be possible to consider incorporating an accessible underdeck space into the design. This approach is particularly feasible for bored tunnels as, by the nature of their construction, a large void is created under the road deck once the tube is bored out and additional excavation is not required. Typically, this void is backfilled with muck the TBM has extracted; however, the opportunity to utilise this space and leverage it to improve the tunnel's operating efficiency should not be ignored.

In the case of a cut and cover tunnel, there are additional considerations to be made as once the level of cleared ground reaches that of the intended road deck, excavating significantly further will increase costs and may not be deemed viable. However, in this case, it is important to conduct a cost benefit analysis (CBA) review to better determine the impacts this decision may have, as a larger capital expenditure may be offset over the longer term by the savings in operating cost over the asset's life.



Alternatively, constructing an accessible space above or between the roadways may be possible as this ground will have already been cleared. The feasibility of this will depend on specific project requirements and other factors such as utilities in the ground or the clearance which must be maintained between the ground level and the upper limit of any new works. These options are presented in **Figures 2** and **3** below.

**FIGURE 2**

Schematic of space available between the roadway in a cut and cover construction for plant room(s)/systems

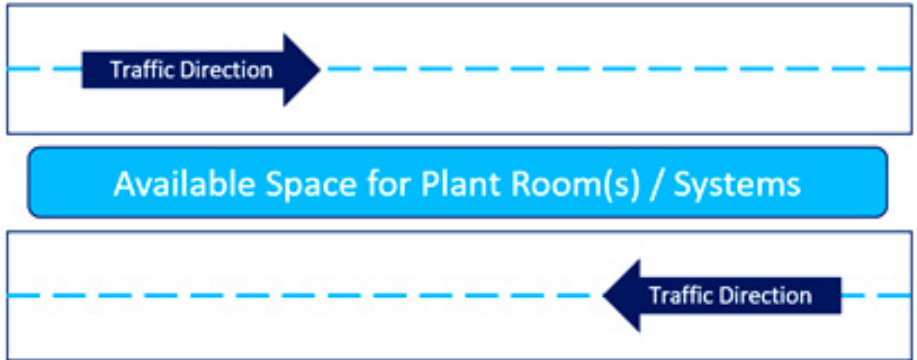
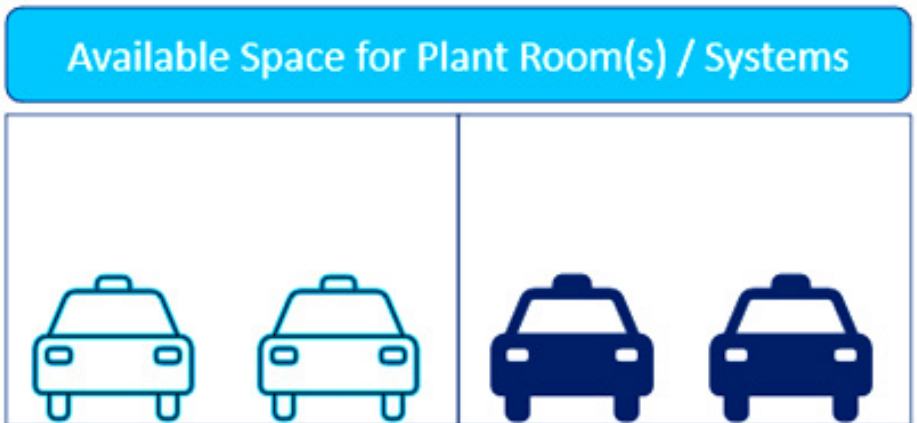


**FIGURE 3**

Schematic of space available above the roadway in a cut and cover construction for plant room(s)/systems



For immersed tube tunnels, the inclusion of an accessible tunnel gallery may be feasible and the value of one can be assessed and validated using a CBA.



## 4.2 DESIGN DECISIONS

When designing an accessible invert or service gallery, the area available within which to locate services and plant will likely have been determined already via the CBA or by virtue of the civils design in the case of a bored tunnel. However, care should be taken to ensure that relocation of all equipment into the invert which is feasible has been considered and that as such the maximum available benefit has been taken from the construction of the accessible invert. If there is benefit still to be taken, then the design can be developed further, and the tunnel diameter reduced.

The benefits offered by an accessible invert in reducing the overall tunnel diameter are readily achievable via the relocation of a wide range of tunnel systems and functions. There are many services which must run along the length of a tunnel including, but not limited to, fire hydrant ring main, FFFS ring main, gravity drainage pipe, pumped drainage sump return pipe, HV ring main, LV distribution, and communication network distribution. In a typical bored tunnel construction, where the invert is backfilled, these services cannot be located in the space which lie vertically beneath the road deck as they will be inaccessible without provision of manhole covers in the roadway which good practice forbids. Therefore, in order to locate these services under the verges and around the tunnel wall, external to the vehicle envelope, requires a widening of the overall tunnel diameter, resulting in significant civils cost increases.

Once these services are located in these places, they can then only be reached for maintenance under a full-bore closure, and by either high level access above the roadway, or within cramped pipe chambers and cable ducts underneath the verges. By relocating these into an accessible invert, the health and safety risks associated with high level working are eliminated and the ability to access and maintain the services while the tunnel is operational is achieved.



#### **4.3 ACCESS/EGRESS REQUIREMENTS**

Obtaining approval for safe access/egress to an invert gallery can be complex and have many requirements which could jeopardise the financial viability of its construction. Depending on the diameter of the tunnel (normally driven by the number of traffic lanes), the cross-sectional space within an invert can be less than we would expect in a typical plant room, for instance.

In addition, access from the invert to the bore/cross passages and the Tunnel Service Buildings (TSBs), is likely to be restricted by construction costs to large distances. These kinds of distances and configurations are not unusual within cable or power tunnels, they however present a range of different challenges within a road tunnel environment.

These challenges are discussed further in section 6.3 where some of the specific design requirements which can be expected are set out.

## **5. Benefits Delivered by an Accessible Invert**

---

An invert which is continually accessible provides benefits against not only the requirements of tunnel owners as set out in section one, but also across other areas which are important to tunnel owners in terms of the increased opportunities to maintain equipment, resulting in longer service life and cost savings. However, there are further benefits offered by the accessible invert.

### **5.1 CONTINUOUS EQUIPMENT ACCESS**

The ability to continually access equipment in case of a fault means issues such as breakers needing resetting, lighting drivers replacing, FFVS valves inspecting, alarm faults investigating, etc, can be attended to 24/7. As such, the tunnel can remain fully available to the public and unplanned closures are not required. This invert solution can be implemented in conjunction with an approach to MORs whereby system mitigations and compensations are utilised to keep the tunnel operating in a safe state above the MOR while the repair is carried out.

This integrated operational approach can result in an increase in tunnel availability as a result of maintaining and inspecting systems to a higher than typical standard due to the ease of access and the zero impact this access has on the tunnel traffic. This means systems which would typically be accessed during a planned closure can be accessed without any impact on tunnel availability, resulting in a more operationally efficient asset.

### **5.2 CONTINUOUS MAINTENANCE**

Being able to constantly access equipment and systems which typically are only accessible under a tunnel closure provides opportunities for continuous maintenance and inspection by tunnel workers which, in turn, can reduce the number of unplanned closures and equipment failures/faults, thus cutting operating costs and improving tunnel availability.

The ability to attend to any faults which occur without closing the tunnel to traffic, be it a planned closure or otherwise, means that not only is the tunnel availability improved, but there is a direct impact on the resilience of the tunnel's MOR. For example, should a system fail which does not result in a breach of the MOR, but reduces the tunnel safety level, it may be attended to and repaired immediately.



Typically, this repair would have to wait until the next planned closure, during which time a further fault could occur which results in a breach of the MOR and forces the tunnel to close. This means the tunnel resilience is enhanced by the ability to rectify any faults immediately and hence the tunnel availability is greater and more robust.

### **5.3 HEALTH AND SAFETY RISKS REDUCED**

In a typical tunnel configuration, the secondary M&E systems which are not located within the main traffic bore are located within the cross passages between the two tunnel bores. This means in order to access this equipment, tunnel staff must implement a lower than normal speed limit within the tunnel and close the outside lane so that a marked vehicle can briefly stop by the cross passage which needs to be accessed and drop off a worker. This must then be done again once the works are complete in order to pick up the worker and return them from the cross passage.

This process carries increased risk with it not only to the worker who must exit from a vehicle in the tunnel with live traffic carrying all their equipment, but also to members of the public who must obey the lane closure and speed limit otherwise they could collide with the stopped vehicle in the outside lane.

By relocating this M&E equipment to an accessible underdeck space, the risks to both the public and the worker from the live traffic are eliminated as the worker can now access the M&E equipment at any time.



## **6. Challenges and Opportunities in the Design and Approval of Accessible Inverts**

---

### **6.1 DESIGN CHALLENGES**

When designing an accessible invert, several considerations must be made, such as how will services be routed into the space from the TSB plant rooms, between the space and the main tunnel bore/cross passages, and the routing of services around pinch points such as intermediate access/egress locations along the tunnel length. These issues are particularly critical when the space available is constrained, such as for a two-lane bored tunnel, or in the case of a cut and cover or immersed tube tunnel with a small footprint restricted by the project requirements.

### **6.2 DESIGN OPPORTUNITIES/SOLUTIONS**

Accessible invert presents many design opportunities to route or locate services which typically would be only accessible during night-time closures, within the space which is continually accessible even when the tunnel is open to live traffic.

Examples of these services and equipment includes:

- › FFFS section valves (typically in Electrical Distribution Panels (EDPs), main bore at high level or within cross passages)
- › Lighting drivers and control (typically in EDPs or within cross passages)
- › CCTV media converters and control (typically in EDPs or within cross passages)
- › Network cards and RIOs (typically in EDPs or within cross passages)



### 6.3 APPROVAL CHALLENGES

Approval for the safe use of the space must be sought from the tunnel owner/operator, fire and rescue service (FRS), and tunnel authorities.

The key concerns of these stakeholders are likely to be as follows:

- › Provision for ventilation within the space;
- › Maximum evacuation distance from the space to a place of relative safety (i.e., cross passage or TSB);
- › Ease of access/egress to the space for the FRS in case of emergency (including rescue equipment);
- › Isolation of the space from the traffic bore above (i.e., fire compartmentation/waterproof to prevent a spillage from flooding the void);
- › Provision of fire detection, alarm and emergency communications; and
- › Longitudinal fire compartmentation.

### 6.4 APPROVAL OPPORTUNITIES/SOLUTIONS

Early engagement with stakeholders is crucial to understand as soon as possible what their appetite for this design approach would be and to determine their expected minimum requirements. This provides time to conduct a proper assessment of the costs of meeting the requirements versus alternative design solutions.

## **7. Challenges of Accessible Inverts in Construction, Operation and Maintenance**

---

While there are clear benefits to accessible invert in terms of possible reduced construction costs and improved access to services 24/7 resulting increased reliability, resilience, and availability, there are some things which need to be considered and factored into the evaluation of the solution.

Installation of services such as drainage pipes and HV cables can be challenging given their heavy weight and large bend radii and so must be considered within the construction phase planning. It is important consideration is given during design to these awkward to install (and renew/refurbish) equipment's and, where possible, provisions should be made to support these activities. This may include things such as incorporating lifting beams within pre-cast invert slabs to install, maintain and replace heavy pumps, and cradles within pre-cast invert slabs to locate and support pipework during the installation.

Additionally, consideration should be given regarding the adaptation and modification of the invert design to better support a modular construction approach, whereby these heavy items can be pre-installed onto the invert slabs externally to the tunnel before being lifted and dropped into place.



## 8. Recommendations for Further Work

---

To quantitatively understand the benefit offered by invert spaces, further investigation is required to better understand the following two main issues and to derive detailed estimations of costs:

- › Tunnel construction savings due to optimised equipment placement
- › Operational cost savings due to:
  - Reduction in tunnel closures
  - Reduction in cost of maintenance/renewal

This necessitates a detailed examination of capital and operational costs for a number of different systems and structures as well as an effective determination of operating assumptions through consultation with tunnel managers and operators.

## **Acknowledgments**

---

Originally presented to and published by the International Symposium on Aerodynamics, Fire and Ventilation in Tunnels, 2022, Brighton, UK.













**Varun Prakash Puneria**  
Mechanical TVS Project Engineer  
Engineering Services  
Canada - Rail & Transit TPO  
Vancouver, BC, Canada



**Somesh Bhatia**  
Tunnel Ventilation EIT  
Engineering Services  
Canada - Rail & Transit TPO  
Vancouver, BC, Canada



**Chandan Sejekan**  
Tunnel Ventilation Engineer  
Engineering Services  
Canada - Rail & Transit TPO  
Vancouver, BC, Canada

## 05. Tunnel Engineering

# Jet Fan Temperature Rating Based on Fan Inlet Airflow Temperatures

### Abstract

A welcome change in temperature requirements from NFPA 130 now implies that the peak heat release rate for the fire source and proximity play a role in determining the inlet airflow temperatures for emergency ventilation equipment. The results presented in this paper are based on inlet temperature analysis conducted for a design-build underground transit project that used a typical fire size of 13.5MW and a refurbishment project for an existing tunnel utilizing a peak fire size of 48MW. The analyses for these projects consider jet fans installed in a tunnel and a proximity train car fire, with passive ventilation scenarios on different tunnel slopes as well as an active ventilation scenario with no slope. Analysis results for passive ventilation cases (0.3% and 5% slope) as well as active ventilation case for the underground transit project suggest that the inlet temperature at the jet fans for an LRT train car fire scenario under the jet fan or within 30m of jet fans does not necessarily exceed the 250°C temperature rating commonly used for projects following NFPA 130 2010 version guideline.

This paper presents the approaches followed to analyse jet fan inlet temperatures for two major underground transit projects and highlights the considerations to be followed with respect to design fire size, active ventilation flow rates, slope of the tunnel, proximity to fire, as well as accounting for default failure of jet fan banks where necessary.

### KEYWORDS

Tunnel ventilation; Computational fluid dynamics; Fire dynamics simulator; Jet fans

## 1. Introduction

---

The paper presents the results of analysis and the corresponding design approach that was followed during the design for two different major Light Rail Transit (LRT) projects. The objective is to highlight the approach taken to procure the jet fans and specify the temperature rating. For the ease of explanation and for better readability, the projects will be referred to as Project A and Project B.

Project A consists of a 19-kilometre corridor that included a 10-kilometre underground portion. The project is a new Design-Build Joint Venture (DBJV) project consisting of multiple underground stations. The design for this project has been performed in compliance with NFPA 130 (2014). This paper presents the inlet temperature analysis of jet fan with one of the underground stations as a baseline model. The geometry for the station and the studied tunnels will be presented in the following sections. The analysis of various emergency scenarios was completed using the CFD software Fire Dynamics Simulator (FDS) version 6.6.0 [5], an industry standard for tunnel ventilation applications.

Project B is an extension of an 8km single-track system presently in operation. The scope of work for the tunnel was to perform the refurbishment of an existing tunnel that is approximately 580m in length. The project required the replacement of existing Tunnel Ventilation System (TVS) that was served by axial fans and had a single point of ventilation for the entire tunnel. The new ventilation system consists of 18 bi-directional jet fans mounted in pairs throughout the tunnel. Similar to Project A, the inlet temperature analysis was performed using FDS.

FDS is a computational fluid dynamics (CFD) solver for fire-driven fluid flow. FDS numerically solves a form of the Navier-Stokes equations appropriate for low-speed ( $Ma < 0.3$ ) thermally driven flow with an emphasis on smoke and heat transport from fires. FDS solves large-eddy simulation (LES) equations on a three-dimensional, orthogonal, multiblock grid. It has been developed and validated specifically for buoyancy-driven flows but has also been validated for jet fans [4].

The CFD simulations were conducted using three-dimensional geometry that was generated from Revit exports and detailed drawings of the structure, equipment, and terrain. The CFD model is simplified by removing small geometrical features such as railings, small signs, etc. from the architectural station Revit models as they have negligible impact on airflow and thus improve model robustness and efficiency.

## 2. Methodology

This section presents the details of the geometry of the Light Rail Vehicles and the tunnel, modelling assumptions, model parameters, and the steps taken in the analysis.

### 2.1 GEOMETRY

As mentioned previously, the work presented in this paper was performed across two LRT projects. The information about the geometry includes the tunnel and the train.

#### 2.1.1 PROJECT A GEOMETRY AND DOMAIN DETAILS

The station chosen for this study is a standalone underground station with the tunnels on both the west and east side of the platform ending as portals to the track section continuing at-grade. The east tunnel which is of length 239.2m and cross-sectional area 20.24m<sup>2</sup> is studied in this paper. The ventilation in this tunnel is served by means of jet fans. The entire underground section, including the station platform of roughly 100m and the east and west tunnels combined, is 513m long. The revenue vehicle used for the analysis consists of three cars. The light rail car used is shown in **Figure 1** consists of five modules and is connected by four gangways. The vehicle is of a low floor design and the entry height is 0.355m from top of rail. The length of each car is 30.8m, width is 2.65m, and height is 3.6m.

**FIGURE 1**

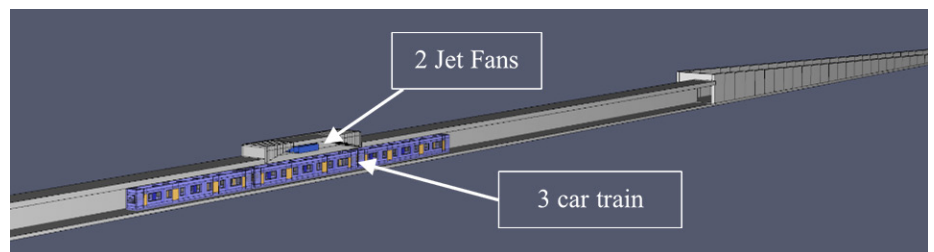
Light rail vehicle  
used in Project A



**Figure 2** shows a snapshot of the geometry of the train and the tunnel in the modelling software PyroSim. In the model, the train is placed directly under the jet fan bank.

**FIGURE 2**

Project A FDS model

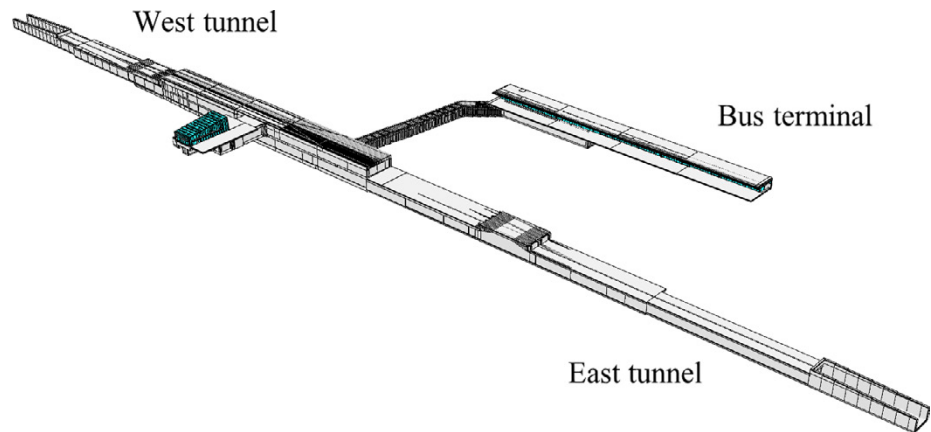




The standalone station is served by four jet fans each in the west and east tunnels for a total of 8 jet fans for the station and tunnel zones. The tunnels are single-box tunnels each for westbound and eastbound directions, and the jet fans are placed in a niche as seen in the above figure in pairs of two per bound. The jet fans used have a thrust of 1800 N and have a rated speed of 1780 RPM. The station model with the east and west tunnels and a connection to a bus terminal is shown in **Figure 3**.

**FIGURE 3**

Project A stand-alone  
station model



### 2.1.2 PROJECT B GEOMETRY AND DOMAIN DETAILS

The tunnel in Project B is 580m in length and has portals on either end. The typical cross-sectional width of the tunnel is 5.4m and the height is 7m. The tunnel is serviced by two different rolling stock and the design has been performed using the more aerodynamically onerous scenario by choosing a light rail vehicle that has a higher frontal cross-section area. The tunnel is equipped with 18 jet fans of thrust 578N and a rated speed of 1765RPM. The equivalent flow rate of the modelled fan was  $15.6\text{m}^3/\text{s}$ .

The results presented in this paper are from a case study performed using a fuel pool fire. The study was performed by modelling for the most onerous ventilation scenario which had the lowest passing margin over critical velocity requirements. The domain in the model is shown in **Figure 4**.

**FIGURE 4**

Project B FDS model

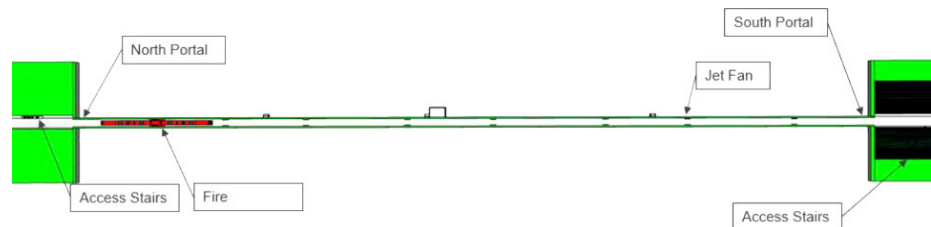
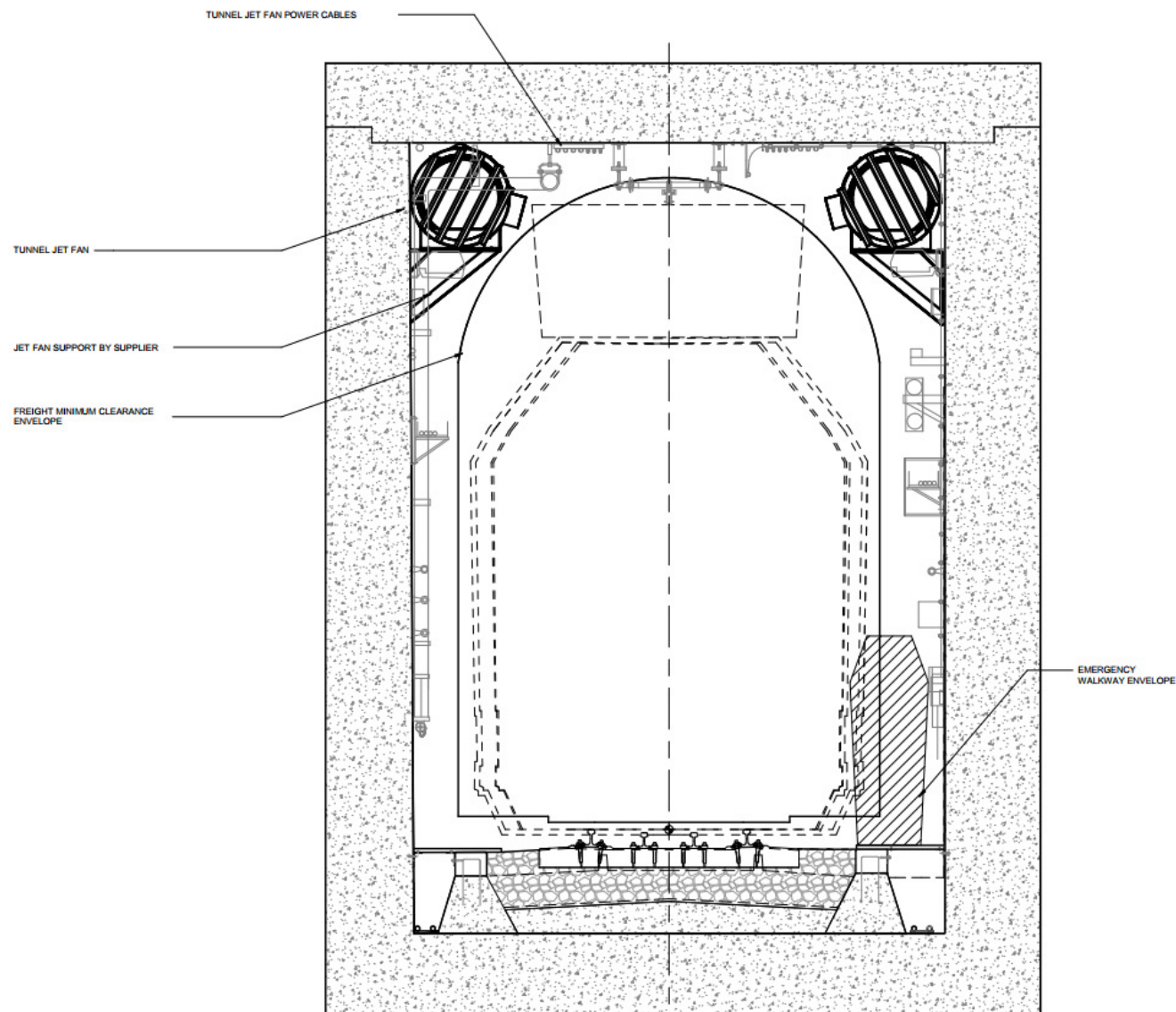


FIGURE 5

Project B tunnel  
cross-section view



## 2.2 CFD TUNNEL FIRE MODELLING ASSUMPTIONS

The following modelling assumptions are made in the development of the model:

1. Train and tunnel features (conduits, FTEs, drip trays, small signs, etc.) that are not expected to impact smoke movement significantly are not incorporated in the model.
2. Train and tunnel geometries are simplified to align with model meshing grid and minimize model complexity, as appropriate.
3. Train operations are assumed to have stopped and the piston effect of the train motion is ignored. Instead, the train is modelled as stationary.

## 2.3 MODEL SETUP

Per NFPA 130 [7], the ventilation system equipment exposed to combustion products must be able to operate for a minimum of one hour. The intent of the models is to study the inlet temperature and any relevant effects of a train car fire in the proximity of the jet fans, which is critical for identifying the temperature rating of the fans.

### 2.3.1 MODELLING IN PROJECT A

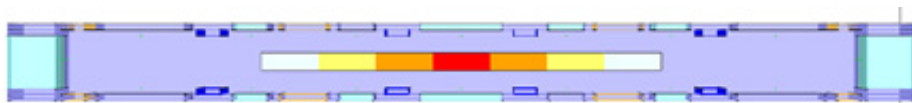
The train design fire is modelled as a series of burner vents within the incident train car with a time dependent  $t^2$  medium growth fire heat release rate reaching an eventual peak heat release rate (HRR) of 13.5MW at steady state. The physical growth of the fire will be simulated using sequential areas, sized and sequenced to correspond with the overall fire growth.

The modelled fire consists of seven surfaces with the fire starting in the middle surface and the adjacent surfaces activating simultaneously after every minute of simulation time to mimic the fire spread. The fire surfaces are modelled 0.6m wide by 2.0m in length and the total fire surface area is 8.4m<sup>2</sup>, as shown in **Figure 6**. The heat release rate of each fire surface is programmed to achieve the overall fire growth rate.

A transient approach is used for Project A to allow for the flow rates to develop, especially for passive ventilation cases. A radiative fraction of 0.35 is used for this project.

**FIGURE 6**

Fire modelling approach  
for Project A





The ambient design conditions were determined from historical climate data for Toronto [2]. The 1% summer dry bulb design temperature is 29.4°C, 1% summer wet bulb design temperature is 22.6°C, and the winter design temperature is 18.8°C. Therefore, the CFD simulations used a mid-range ambient temperature of 12°C.

### 2.3.2 MODELLING IN PROJECT B

In Project B, the train fire is simulated in CFD and modelled as a surface fire at the train PowerPack, representing a fuel pool fire. The fire surface is modelled as a surface of length 17m and width 2.8m. A steady-state modelling approach is used for this project with a radiative fraction of 0.3.

This study was done with the most onerous case from the emergency scenario simulation and adjusted to summer ambient conditions. The temperature was determined from historical climate data for Ottawa [1]. The 1% cooling dry bulb temperature is 29°C, so an ambient design temperature of 30°C is adopted.

### 2.3.3 DESIGN FIRE

A fire releases heat by radiation and convection. Ultimately, a net amount of radiated heat is absorbed by the tunnel walls, floor and ceiling, and the remaining convective fraction drives the thermal plume, which must be controlled by the ventilation system. The below references mention the ranges of convective fraction. Note that a higher convective fraction is a more onerous condition.

- › NFPA 92 [6]:  $f_c = 0.7$
- › Ingason et al [3]:  $0.67 < f_c < 0.7$
- › Heskestad [2]:  $0.6 < f_c < 0.7$

**TABLE 1**

Design fire parameters

Characteristic	Project A	Project B	Equation
Fully Developed Fire Heat Release Rate	13.5MW	48MW	
Convective Fraction ( $f_c$ )	0.65	0.7	
Train Fire Growth Rate	0.011723 kJ/s <sup>3</sup>	N/A	
Train Fire Growth Time to Peak	1073s	N/A	$t = \sqrt{(Q/\alpha)}$
Heat of Combustion ( $\Delta H_c$ )	18MJ/kg	46MJ/kg	
Air-Fuel Ratio (AF)	14	14	



## 2.3.4 Modelling Scenarios

Details	Fire location	Ventilation	Description
Case 1 – Project A	Upstream of jet fan bank	Active ventilation with 36m <sup>3</sup> /s flowrate in the tunnel	A proximity tunnel train car fire of size 13.5MW is used with the train car fire upstream of the jet fan banks. Active ventilation is applied from the station end to push smoke towards portal opening. The jet fan thrust under the fire is not modeled.
Case 2 – Project A	Upstream of jet fan bank	Passive ventilation and approx. Zero tunnel slope (0.3%)	A proximity tunnel train car fire of size 13.5MW is used with the train car fire upstream of the jet fan banks. Passive ventilation is expected with no slope (0.3%). The station and portal opening aerodynamic interaction is monitored. The jet fan bank under the fire is not operational.
Case 3 – Project A	Under the jet fan bank	Passive ventilation and 5% tunnel slope	A proximity tunnel train car fire of size 13.5MW is used with the train car fire under the jet fan banks. Passive ventilation is expected with 5% tunnel slope. The station and portal opening aerodynamic interaction is monitored. The jet fan bank under the fire is not operational.
Case 4 – Project B	Under the jet fan bank but also affects the jet fans downstream.	Active ventilation with lowest passing flowrates for the project.	A pool fire of size 48MW is used with the fire under the jet fan bank. The closest jet fan bank downstream of the fire is studied for inlet temperatures whereas the jet fan bank above the fire is designated as failed irrespective of the temperature results.  Active ventilation is applied in the tunnel.

The results for Case 1 and Case 4 are of prominence for Project A and Project B, respectively, as they determine the inlet temperatures when an emergency ventilation response is activated for a train car fire near the jet fans. Subsequent cases 2 and 3 for Project A explore alternative scenarios where the operator has not activated the ventilation response in a proximity train car fire and inlet temperatures are monitored as the fire grows and reaches steady state at no slope and 5% slope conditions.

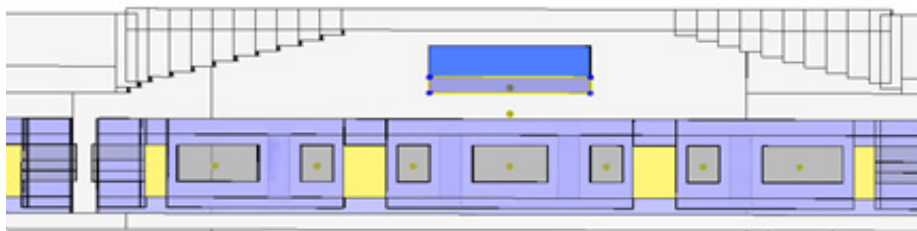
### 3. Results and Discussion

The results of the different cases studied across the two projects are discussed in this section. The simulations were performed until steady state peak HRR is reached and the key parameters such as temperature, HRR, and flowrates stabilized. The primary objective of these analyses is to determine the inlet air temperatures at jet fans.

In the sub-sections below, for Project A, the longitudinal temperature slices are presented. Additionally, the jet fan temperatures that were measured using devices in FDS are tabulated for each case. The measurement locations were in the jet fan bank envelope and a separate zone below the jet fans, extending 0.6m under the fans as shown in **Figure 7**.

**FIGURE 7**

Jet fan temperature  
measurement zone



#### 3.1 CASE 1: PROJECT A, FORCED VENTILATION WITH A FLOW RATE OF 36M<sup>3</sup>/S

In this case, the analysis was performed with active ventilation pushing the smoke towards the portal. The flow rate at the station end of the east tunnel was set as 36m<sup>3</sup>/s in the tunnel with the incident train and the portal end of tunnel was a boundary open to atmosphere. This flow rate was conservatively chosen based on the lowest critical velocity requirement in all tunnel cross-sections (a cross-over tunnel) found across Project A during tunnel fire emergency scenarios involving jet fans. In comparison, the critical velocity required for a train car fire in the modelled tunnel is 2.46m/s, corresponding to the 49m<sup>3</sup>/s flowrate. The emergency ventilation response across the project is designed to exceed the critical velocity; thus, these lower flow rates used for modelling are conservative as higher airflow rate (and air velocity) is expected during a tunnel train car fire emergency ventilation. It was observed that although the surrounding temperatures exceeded 250°C, the inlet temperature at the jet fans as well as temperatures in the jet fan envelope do not exceed 250°C even at the peak HRR, as shown in **Figure 8** and **Figure 9**. In the temperature plots, exceedances over 250°C are represented in black. Both the maximum temperatures in the jet fan bank and average temperatures are found to be below 250°C.

FIGURE 8

Temperature in the domain for case 1

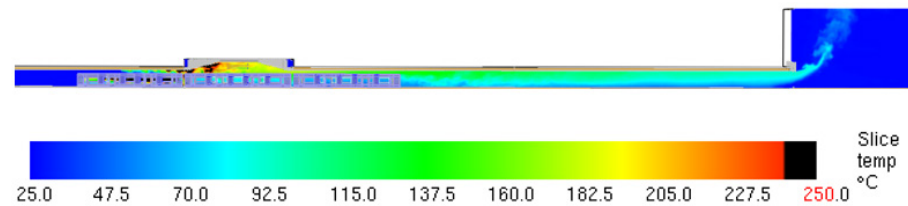
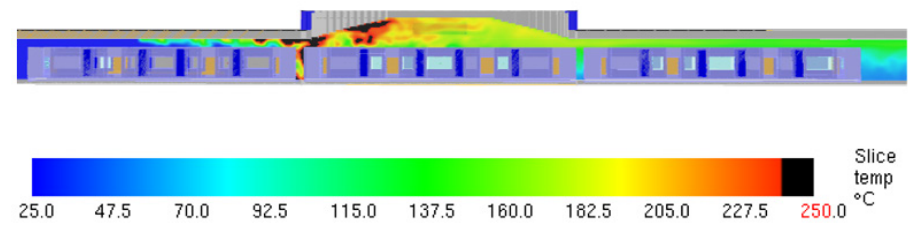


FIGURE 9

Temperature surrounding the jet fans for Case 1



The maximum and average temperatures in the jet fan bank and the zone below the jet fans and extending to a distance of 0.6m under the jet fans are tabulated below.

TABLE 2

Maximum and average temperature for Case 1

Temperature in the zones	Maximum temperature °C	Average Temperature °C
Jet Fan Bank	241.46	201.17
0.6m zone below jet fan	244.27	203.45

The results for Case 1 are of prominence for Project A as they imply that if the emergency ventilation response is activated for a tunnel train car fire in close proximity to the jet fans, the resulting inlet temperatures will be lower than 250°C. The jet fans procured for this project were capable of withstanding temperatures up to 300°C, providing for a safety margin.

The choice of placing the train car fire upstream of the jet fans was strategic as the ventilation would direct the hot smoke towards the jet fan inlets. This case can be contrasted with Case 3 where the train car fire is directly under the jet fans and the region of hot smoke is observed downwind of the jet fans.

The velocity in the proximity of the jet fan niche is as shown in Figure 10. The visibility slice demonstrates that the smoke is exhausted out of the tunnel through the portal.

FIGURE 10

Velocity in the proximity of the jet fans for Case 1

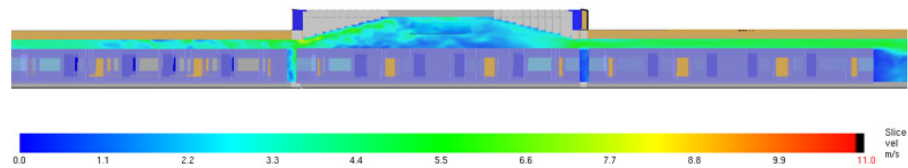
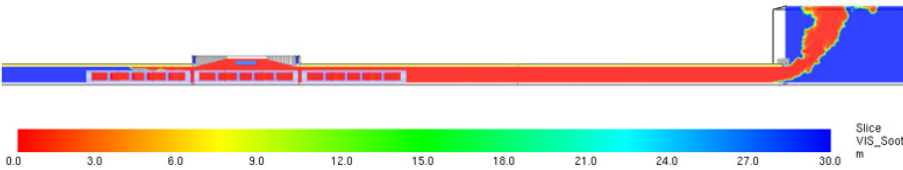


FIGURE 11

Visibility Plots for  
the tunnel Case 1



3.2 CASE 2: PROJECT A, PASSIVE VENTILATION WITH NO SLOPE

In this case, the analysis was performed with a west train car fire with passive ventilation. The tunnel is modelled without any slope (i.e., 0.3% for drainage). The portal end of east tunnel was modelled as a boundary open to ambient conditions. Similarly, the portal opening for tunnel west of the station as well as station entrances are modelled open to ambient conditions. The station side of the east tunnel with train car fire is subjected to resistances to the flow due to the station geometry and the tunnels on station's west end. It was observed that although the surrounding temperatures exceeded 250°C at steady state, the inlet temperature at the jet fans did not exceed 250°C for this scenario, at steady state peak HRR. as shown in Figure 12 and Figure 13.

FIGURE 12

Temperature in the  
domain for Case 2

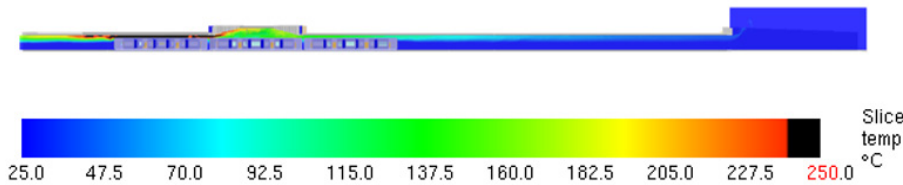
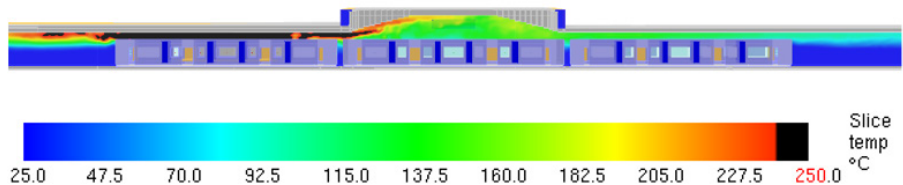


FIGURE 13

Temperature surrounding  
the jet fans for Case 2



The maximum and average temperatures in the jet fan bank and the zone below the jet fans extending to a distance of 0.6m under the jet fans are tabulated below.

TABLE 3

Maximum and average  
temperature for Case 2

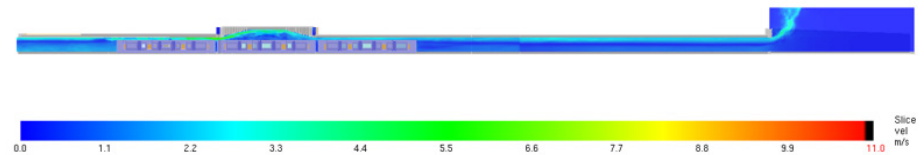
Temperature in the zones	Maximum temperature °C	Average Temperature °C
Jet Fan Bank	220.36	151.17
0.6 m zone below jet fan	202.66	135.85



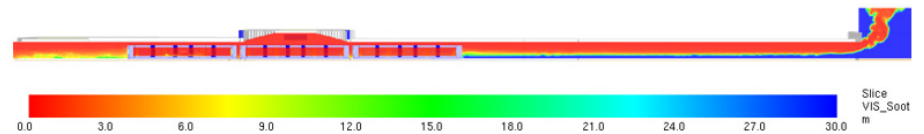
From the velocity slice shown in **Figure 14**, the domain has a low magnitude of airflow. The hot smoke rises to the roof and flows towards the station and the portal. At steady state, the average flow in the tunnel from the portal was towards west (i.e., towards the train car fire) with a magnitude of  $4.76\text{m}^3/\text{s}$ , suggesting that while hot smoke layers up along the tunnel roof and escapes from the tunnel portal, cold air is flowing into the tunnel along the tunnel floor. A similar phenomenon is observed on the station side of the east tunnel, as well. The visibility slice demonstrates that at steady state, in the absence active of ventilation, the visibility in the tunnel is poor on either side of the train. As the hot smoke is localized in this case, further investigation may be required to study the inlet temperatures at jet fans for a zero-sloped passive ventilation case by changing the car fire locations.

**FIGURE 14**

Velocity magnitude in the domain for Case 2

**FIGURE 15**

Visibility Plots for the tunnel Case 2



### 3.3 CASE 3: PROJECT A, PASSIVE VENTILATION WITH 5% SLOPE

In this case, the analysis was performed with a middle train car fire under passive ventilation but with the tunnel sloping up by 5% towards the east end of the tunnel. The portal end of east tunnel was modelled as a boundary open to ambient conditions. Likewise, the portal opening for tunnel west of the station as well as station entrances are modelled open to ambient conditions. The station side of the east tunnel with the train car fire is subjected to resistances to the flow due to the station geometry and the tunnel on station's west end. It was observed that although the surrounding temperatures exceeded  $250^{\circ}\text{C}$  at steady state, the inlet temperature at the jet fans does not exceed  $250^{\circ}\text{C}$  even at the peak HRR, as shown in **Figure 16** and **Figure 17**.

FIGURE 16

Temperature in the domain for Case 3

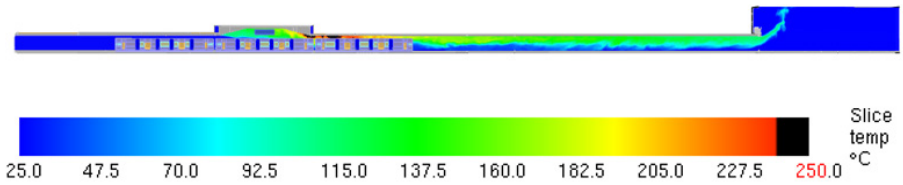
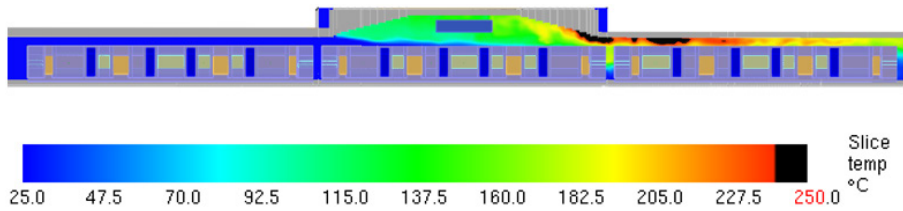


FIGURE 17

Temperature surrounding the jet fans for Case 3



The maximum and average temperatures in the jet fan bank and the zone below the jet fans and extending to a distance of 0.6m under the jet fans are tabulated below.

TABLE 4

Maximum and average temperature for Case 3

Temperature in the zones	Maximum temperature °C	Average Temperature °C
Jet Fan Bank	189.06	128.96
0.6m zone below jet fan	228.87	133.3

From the velocity slice shown in **Figure 18**, the majority of the flow is towards the portal. The cause for this observation is that the 5% slope within the domain is the primary contributor in the development of the buoyancy driven flow. At steady state, the average flow in the tunnel was towards east with a magnitude of 28.6m<sup>3</sup>/s. These results can be contrasted with the results shown in Case 1 as the flow rates are of similar magnitude. It also provides further evidence that in the presence of substantial airflow in the tunnels, the temperatures at the jet fans can stay lower than 250°C. The visibility slice demonstrates that the smoke is passively moving under the influence of buoyancy towards the portal end.

FIGURE 18

Velocity magnitude in the domain for Case 3

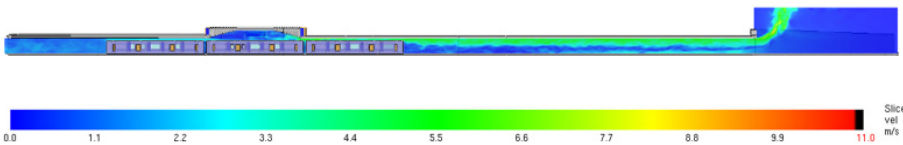
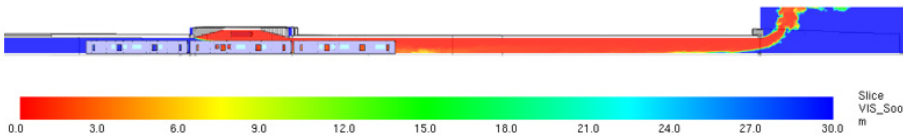


FIGURE 19

Visibility plot in the domain for Case 3



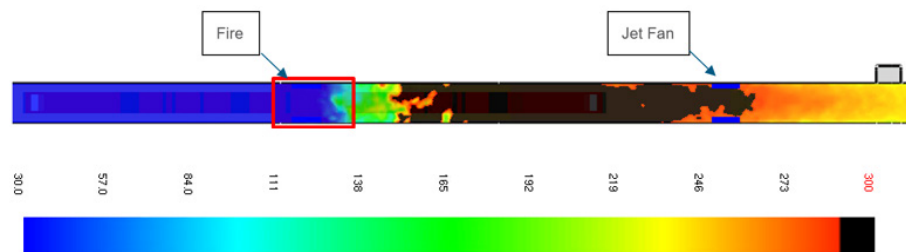
### 3.4 CASE 4: PROJECT B, PEAK HRR 48MW

This simulation is a steady-state simulation with a peak heat release rate of 48MW. In the simulations, temperature results were reported at the inlet and outlet of each jet fan. Using a 60-second average after reaching steady state peak HRR, the maximum temperature reported is 289°C from the jet fan pair downstream from the fire.

Below is a visualisation of the thermal plume generated by the fire, controlled by the jet fans. This steady-state simulation shows the temperature contours through the jet fans. The horizontal slice is 6.2m from the tunnel floor through the jet fan. A localized area above 300°C is noted, but this does not sufficiently impact the fans to exceed the specified operating temperature and for them to be incapacitated. In this simulation, the distance from the fire to the next downwind pair of jet fans is 58m. The jet fans above the fire are considered to have failed although the temperature slices do not show high temperature exceedances of above 300°C. This is considered conservative for evaluating ventilation performance in the event of a fire.

FIGURE 20

Tunnel plan view – 60s  
average temperature



Based on these results, and to maintain a margin of safety, a jet fan temperature rating of 400°C was selected for procurement specifications.



## 4. Conclusions

---

The following conclusions can be drawn based on the results presented in the previous section:

1. The fire size is an important factor in determining the fan temperature rating. Project A had a 13.5MW fire which resulted in maximum and averaged temperatures at the jet fan bank to be lower than 250°C for the cases considered, with Case 1 reporting proximity average temperatures of 201°C. Project B, which used a 48MW pool fire, resulted in average temperatures of 289°C at the inlet of the jet fans located 58m downstream of the fire.
2. In the analyses undertaken for Project A, the studies were performed with the jet fan bank in the proximity of the fire. The active ventilation Case 1 in conjunction with the passive ventilation Case 3 (5% sloped tunnel) show that, in the presence of substantial ventilation flow rates, as would be expected when a mechanical emergency ventilation response is activated, the maximum inlet temperatures for Project A do not exceed the 250°C temperature.
3. The passive ventilation Cases 2 and 3 represent scenarios where ventilation system was not activated. Results demonstrate that, in a proximity train car fire scenario, the jet fans do not necessarily encounter temperatures beyond 250°C where they would be considered to have failed. While further investigation can be carried out, especially for no slope tunnel cases, they are not representative of the active emergency ventilation response generally expected during a train car fire emergency scenario.
4. The jet fans selected for Project A are rated for operation at 300°C for one hour and provide for a safety margin over the predicted temperature results.

5. Case 4 demonstrates that FDS can be used for analysis in the selection of the temperature rating for jet fans. Based on FDS analysis, the jet fans were anticipated to be subject to smoke at maximum temperatures close to 300°C. As a result, the jet fans for Project B were procured to withstand 400°C for one hour to provide a sufficient safety margin over predicted temperatures.
6. It must be noted that while Project A used internal compartment fires for design, Project B used pool fires due to the nature of its rolling stock.

Peak fire heat release rates, flow rates achieved in the tunnel during active ventilation, tunnel slopes, and buoyancy effects, as well as cross-sectional areas are some of the factors identified in this paper that influence the inlet air temperatures at jet fans used for tunnel emergency ventilation. The nature of fire and methods of modelling the fire are also a factor that influence inlet temperatures observed at jet fans in tunnels.





## Acknowledgements

---

The authors acknowledge the contributions of the entire engineering team working on the two projects.

The paper was originally presented and published at Framatome BHR's International Symposium on Ventilation and Fire in Tunnels, Brighton, UK, September 2022.

## References

---

1. ASHRAE, 'Fundamentals', ASHRAE, 2017
2. G Heskestad, 'Fire Plumes, Flame Height, and Air Entrainment', in SFPE Handbook of Fire Protection Engineering, 5th Ed., Springer, 2016
3. H Ingason, YZ Li, A Lonnermark, 'Tunnel Fire Dynamics', Springer, 2015
4. McGrattan et al, 'Fire Dynamics Simulator Technical Reference Guide Volume 2: Verification Guide, NIST, 2018
5. McGrattan et al, 'Fire Dynamics Simulator - User's Guide', NIST, 2018
6. NFPA 92 Standard for Smoke Control Systems, 2019
7. NFPA 130 Standard for Fixed Guideway Transit and Passenger Rail Systems, 2017









**Edward Lupton**  
Engineering Geologist  
Engineering Services – Infrastructure UK  
Cardiff, UK



**Jack Blake**  
Senior Geotechnical Engineer  
Engineering Services – Infrastructure UK  
London, UK



**Stuart Archer**  
Principal Engineering Geologist  
Engineering Services – Infrastructure UK  
Cardiff, UK



**Rebecca Evans**  
Principal Geotechnical Engineer  
Engineering Services – Infrastructure UK  
Cardiff, UK

**Marcus Huband**  
Associate Geomorphologist  
Engineering Services – Infrastructure UK  
Cardiff, UK



**Stuart Mortimore**  
Chief Geotechnical Engineer  
Engineering Services – Infrastructure UK  
London, UK

**Iain McKenzie**  
Principal Geotechnical Engineer  
Welsh Government – Transportation Department  
Wales, UK

## 06. Geotechnical Engineering

# Protecting Critical Infrastructure through Georesilient Design: A Case Study from the A40 near Llanegwad

### Abstract

Critical infrastructure is at greater risk of deterioration and failure under a changing climate. To build resilience into design, a thorough understanding of the role of geomorphological and geological conditions, and climate scenarios is needed. In Carmarthenshire, Wales, rapid lateral erosion rates of the River Towy are threatening the stability of the A40 trunk road, which is estimated to be undercut within 10 to 15 years. A resilient, climate-proof solution was required. This was developed through a phased optioneering exercise to identify constraints, risks, and uncertainties for a range of design options. The most suitable option was considered to be an anchored embedded sheet pile retaining wall set back from the river's edge, which was taken forward to design and construction. The design needed to account for significant constraints such as a very tight working width adjacent to a Special Area of Conservation (SAC), and a large theoretical retained height should worst-case scour events occur in future. Utilising the geomorphological understanding of the site, the required length and alignment of the wall was optimised to maximise the protection afforded to the A40. This case study highlights the multi-disciplinary, risk-based decision-making process that is required to develop resilient solutions.

### KEYWORDS

Highway assets; River erosion; Scour; Geomorphology; Sheet pile retaining wall

## 1. Introduction

---

The River Towy is a large, geomorphologically active river that flows from the Cambrian Mountains in a south-westerly direction through Carmarthenshire to the Bristol Channel. It is one of the longest rivers flowing entirely within Wales at a length of 120km and is of ecological importance due to its native flora and fauna. The banks of the river between Llandovery and Pembrey coast are protected as a Site of Special Scientific Interest (SSSI) and a Special Area of Conservation (SAC). The footprint of these areas is in a constant state of flux as the river erodes and deposits materials over time. The river flows past several key pieces of public transportation infrastructure including the A40, which is a principal trunk road connecting London with Fishguard, and a regionally and nationally important transport corridor.

The A40, which is managed by the South Wales Trunk Road Agent (SWTRA), has been identified as being at risk of undercutting from the River Towy between Llandeilo and Carmarthen specifically at a site located approximately 500m to the east of the village of Llanegwad (Ordnance Survey (OS) Grid Reference 252567, 221432). At this site, the A40 is located along the northern flank of the floodplain, which is also the location of a significant meander in the river.

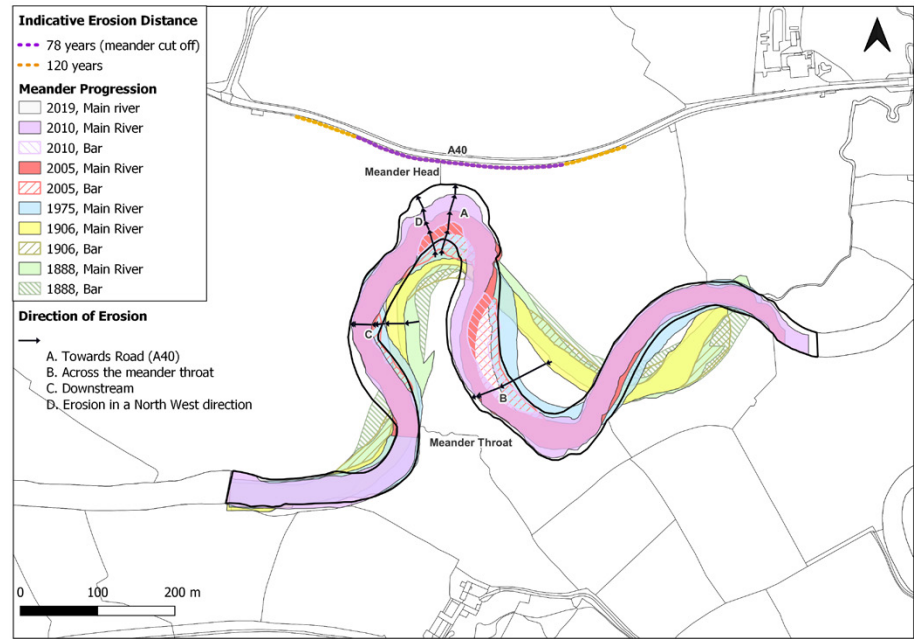
The floodplain width from the toe of the embankment supporting the westbound lane of the A40 to the crest of the riverbank at the point of the meander closest to the road was 24.6m in June 2020. At the site, the river is between 40 and 90m wide, with a typical depth of 2 to 4m under normal flow conditions. It has previously been estimated that the meander has been eroding at an average rate of approximately 0.75m/year between 1888 to 2010, indicating that the A40 would be undercut within 38 years. However, erosion rates have appeared to accelerate recently with an increase to a maximum rate of approximately 4.5m/year between 2005 and 2010. Considering this increased erosion rate, without any preventative measures, the River Towy was projected to erode the embankment supporting the A40 within 10 to 15 years. Atkins were commissioned by SWTRA to assess the risk associated with the River Towy undercutting the A40 and propose a resilient solution to protect this critical section the A40 from river erosion.

## 2. Fluvial Erosion Risk Assessment

The River Towy is a highly active river system, with the river planform in a constant state of flux as it migrates across its floodplain. Analysis of historical OS mapping from 1888 to the present day, and more recent aerial imagery and open-source LiDAR (Natural Resources Wales (NRW), 2022) demonstrated the dynamic nature of the Towy's planform. The analysis indicated that the meander is progressing towards the road at an average rate of 0.75m/year. However, as rivers are complex non-linear systems that are unlikely to respond in a predictable manner (Schumm, 1973), the rates and patterns of river erosion are difficult to forecast. River channels can move hundreds of metres within a few decades and, in some instances, tens of metres or more during a large flood event. Rivers can also scour or fill channels with sediment, commonly to a depth of 1-2m, but sometimes to greater depths (Macklin & Harrison, 2012). In 1888, the distance between the riverbank and the road was 112m; however, by 2019, a topographic survey measured this distance as just over 24m. Analysis showing the dynamic nature of the River Towy is illustrated in **Figure 1**.

**FIGURE 1**

Historical migration  
of the River Towy near  
Llanegwad (1888-2019)





Analysing the past planform migration of the River Towy allowed prediction of future river alignments. These predictions relied on two significant assumptions: a) that the river could move from the current alignment in any direction (upstream or downstream), and b) that the river will continue to move at an average rate of 0.75m/year towards the A40 (see direction of erosion "A" in **Figure 1**). From these assumptions, a buffer of the 2019 alignment of the river was produced for two time periods: a) 78 years and b) 120 years. The 78-year time period is the anticipated timeframe in which the Llanegwad meander will be cut off. This would result in the river shifting away from the A40, therefore removing the risk of undercutting at the northern riverbank. The longer time period of 120 years is the desired design life of an engineering scheme to protect the A40. From the fluvial erosion risk assessment, the predicted length of the A40 at risk of being undercut by the River Towy was determined to be 164m over 78 years and 241m over 120 years (**Figure 1**).



### 3. Informed Optioneering Assessment

---

Following the fluvial erosion risk, a multi-disciplinary optioneering assessment was undertaken to advise on the most appropriate solution considering: a) existing constraints (primarily ecological, environmental, and spatial), b) the inherent uncertainty in the fluvial erosion risk, and c) the ground conditions of the site. Early discussions with Natural Resources Wales (NRW) identified that planning permission would be required for work within 8m of the riverbank due to the SSSI and SAC designations placed upon the site.

The first stage in the optioneering assessment was to undertake a preliminary ground investigation (GI) to characterise the ground conditions. The initial GI phases were completed in 2017 and 2018 and comprised five dynamic sampled boreholes with rotary core follow on to a maximum depth of 17.5m below ground level (bgl). The GI identified cohesive Alluvium (of 1 to 2m typical thickness) overlying granular Alluvium. Mudstone was recorded in only one borehole located within the A40 from 11.90m bgl, indicating that rockhead may drop significantly towards the river channel. Based on the available information on the local ground conditions derived from the GI and existing site constraints, four high-level solutions were considered: 1) working with natural processes, 2) realignment of the highway, 3) a set-back retaining wall, and 4) a buried rock revetment.

#### 3.1 WORKING WITH NATURAL PROCESSES

Accelerated meander cut off was proposed that would increase the rate in which the meander neck is cut off, thereby realigning the flow of the River Towy away from the A40. This was considered a highly uncertain option due to the variability of processes involved. Encouraging meander cut-off was predicted to increase the gradient of the channel bed leading to accelerated local bank and bed erosion to force planform adjustment to recover the natural slope gradient. This could result in loss of agricultural land and habitat types associated with a dynamic river system, thereby threatening the SAC and SSSI designation of the river.

#### 3.2 HIGHWAY REALIGNMENT

The highway realignment option proposed relocating the A40 further north, cutting into an existing slope and on an alignment where the bedrock (Nantmel Mudstones Formation) is shallow enough to limit northward migration of the River Towy. The final alignment of the A40 would be highly dependent on the depth of competent bedrock. This option required the most extensive third-party land purchase.

### 3.3 SET-BACK RETAINING WALL

Various retaining wall solutions were considered with the primary options including: a) a sheet pile wall supported with deadman anchors, b) a sheet pile wall supported with inclined ground anchors, and c) a bored pile wall solution. In these options, the embedded retaining wall would be constructed set-back from the river and would be fully buried post-construction on both the active and passive sides of the wall. As the river erodes and progresses towards the wall, the retained height would be progressively increased, causing differential lateral earth pressure and the initiation of the retaining wall carrying load.

In the proposed sheet pile wall supported with deadman anchors solution, it was determined that the required deadman anchor size would be unfeasibly large in size to provide sufficient resistance and was therefore deemed too difficult to accommodate within the spatial constraints of the site.

In the proposed sheet pile wall supported by inclined ground anchors solution, this option could be set further back from the riverbank with the inclined anchors able to extend towards and beneath the A40. Although the anchor forces would still be significant, the required resistance could be provided from grouted anchors. Compared to other anchorage systems, larger horizontal restraining forces could be generated using the angled anchors in the available space. For construction of the anchor arrangement, excavation and the installation of a suitable working platform would be required in front of the wall. Ongoing maintenance of the anchors would also need to be considered to ensure sufficient design life.

The final proposed bored pile wall option would bore deep enough to work in cantilevers and remove the need for an anchor system entirely, saving construction time and cost, as well as eliminating the need for a maintenance programme for ground anchors. However, it was identified early on that although the wall could satisfy the ultimate limit state of the design retained height, large deflections would likely be experienced in the serviceability limit state consequently deeming it unsuitable without anchorage. On the basis that some form of anchorage would be required, it was decided a sheet pile solution would be a more cost-efficient solution.



### **3.4 BURIED ROCK REVETMENT**

Due to the 8m exclusion zone and spatial constraint of the embankment supporting the A40, there was insufficient space to consider a completely buried rock revetment. However, a revetment could form part of a hybrid design where an anchored sheet pile would be required at the pinch point of the meander head, with a buried rock revetment constructed up and downstream either side. This option required many components and interfaces, large excavations, and the disposal of large volumes of material. It also required a complex maintenance regime and contained uncertainties on the dynamic operation of the apron in response the river.

### **3.5 CONCLUSIONS OF THE OPTIONEERING EXERCISE**

The optioneering exercise identified the optimum solution by balancing cost, risk, and programme. This concluded a) realignment of the A40, b) an embedded sheet pile wall with inclined ground anchors, and c) hybrid buried rock revetment and embedded sheet pile wall with inclined ground anchors were preferred choices in the absence of more detailed GI information. The A40 realignment solution was heavily dependent on the presence of bedrock being encountered at shallower depths, which required confirmation by further GI. In contrast, the embedded sheet pile wall solutions (including buried revetment) required bedrock to be confirmed as sufficiently deep so as not impact the driveability of the sheets.

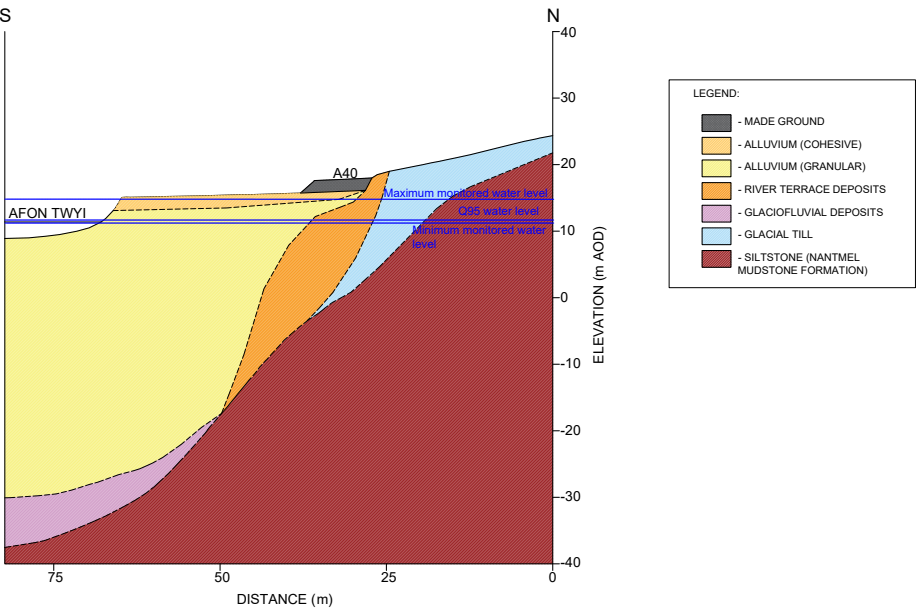
## 4. Detailed Development of Resilient Geotechnical Solution

### 4.1 GROUND MODEL

Following the completion of the informed optioneering assessment, a third phase of targeted GI was specified and completed in March 2021. This comprised seven dynamic sampled boreholes with rotary core follow on to a maximum depth of 30m bgl and a seismic refraction tomography and electrical resistivity tomography geophysical survey. The geophysical survey was deemed critical for confirming the depth to bedrock across the site, as it was not consistently encountered in the earlier phases of intrusive-only GI. From GI information from all phases, a ground model was developed (Figure 2).


FIGURE 2

A40 Interpreted  
Ground Model



Ground conditions generally comprised 2m of cohesive Alluvium, overlying thick deposits of granular Alluvium. These were underlain by Glaciofluvial Deposits and Siltstone of the Nantmel Mudstones Formation. River Terrace deposits were recorded beneath the A40, and Glacial Till was anticipated to be present to the north.





Siltstone of the Nantmel Mudstones Formation was recorded at 17m bgl beneath the A40; however, bedrock was not encountered in any of the boreholes located in the flood plain. Continuous cross-sections from the seismic refraction tomography and electrical resistivity tomography survey confirmed the presence of bedrock at approximately 17m bgl beneath the A40 and also identified a steep increase in depth to bedrock towards the river, imaging bedrock depth >30m bgl beneath the flood plain.

#### **4.2 DETERMINATION OF SINGLE OPTION DEVELOPMENT**

The additional GI information confirmed that realignment of the A40 could not be developed any further due to the significant depth to bedrock, coupled with potential land take issues. Both the embedded sheet pile option with inclined ground anchors and the hybrid rock revetment option with a sheet pile wall supported by inclined ground anchors were plausible based on the encountered ground conditions. However, the hybrid rock revetment option was considered to carry greater technical risk associated with the dynamic behaviours of the river channel and potential variability of the solutions' response to the erosion and therefore protection offered to the A40. Furthermore, it would require a more demanding maintenance regime and was anticipated to have similar construction costs to the sheet pile wall with inclined ground anchor support. Consequently, it was determined that a sole sheet pile wall with inclined ground anchors was the optimal solution to provide long-term resilience to the operation and usage of the A40.

#### **4.3 GEOMORPHOLOGICAL ASSESSMENT**

With the proposed protection measure confirmed, a detailed assessment of the extent of A40 at risk from erosion was undertaken to determine the length of wall needed to protect the road. Identifying the at-risk section was largely determined by predictions of how the River Towy could migrate over the operational life of the structure, taking into consideration factors such as climate change, wall effect, and erosion trajectory.

The assessment considered three assumption-based scenarios of the length of road at risk. These scenarios were determined from a buffer distance which was estimated using *erosion rate, period of operation, a wall effect factor, an erosion trajectory factor, and a climate change factor*. Separate estimates were undertaken to determine the upstream and downstream buffer zone distances.

The buffer zone was the distance applied as an offset to the right bank edge of the River Towy to predict the wall length required to protect an equivalent section of A40 carriageway associated with each scenario, with the transition between upstream and downstream progression taken as the apex of the bend.

*Erosion rate* is defined as the rate at which the River Towy erodes towards the A40. Three rates, based on analysis of historical rates of erosion, have been used in the scenario analysis.

*Period of operation* is defined as the number of years the wall will need to function. Two shorter periods (71 and 78 years) were based on trajectories leading to meander cut-offs. The longer period assumed the wall must continue to function for 120 years (the optimum structure design life).

A *wall effect factor* has been considered for the analysis depending on different scenarios, which considers how the introduction of a smooth hard surface, such as the proposed sheet pile wall, into a fluvial system can reduce friction associated with erosion. In turn, this can result in an acceleration in erosion rates adjacent to and downstream of the hard surface.

The *erosion trajectory factor* considered the future impact of meanders. Meanders commonly migrate in a down-valley direction. However, occasionally, and particularly in the presence of hard irregularities in the valley floor, meanders can (unexpectedly) migrate upstream.

The *climate change factor* assumed that erosion rates of the River Towy will increase over time and in proportion with an increase in river flows in west Wales as a consequence of climate change. Based on guidance provided by the Welsh Government, an allowance for an increase in peak flow of 30% was applied (Welsh Government, 2021). A summary of the variables used for the estimation and buffer distances estimated is shown in **Table 1**.

**TABLE 1**

Variables used to  
determine buffer distance

Estimated length of road at risk	Erosion rate (m/yr)	Period of operation (yrs)	Wall effect factor	Erosion trajectory factor	Climate Change factor	Total Buffer distance (m)	Proposed wall length (m)
Longest	2.95	120	1.50	1.00 (downstream) 0.75 (upstream)	1.30	1208	1321
Medium	0.75	78	1.25	1.00 (downstream) 0.50 (upstream)	1.30	143	228
Shortest	0.67	71	1.00	1.00 (downstream) 0.75 (upstream)	1.30	77	128

Each buffer distance was then applied to the existing river course to determine the length of wall required for each scenario using a GIS analysis. This concluded that the longest section road at-risk scenario required a 1,321m wall, the medium section scenario required a 228m wall, and the short section scenario required a 128m wall. The results of this assessment were integrated with a review of the historic planform migration, which determined that a 228m long wall length (medium length of road at risk scenario) was most appropriate. This was increased slightly in the final length to allow angled wall ends away from the road, directing the river's future erosional pattern towards an identified palaeochannel and guiding towards a more natural taper.

A separate assessment was undertaken to assess the maximum height of the retaining wall, to the base of the River Towy and any additional erosion associated with short term scour events. The assessment follows the United States Department of Agriculture (USDA) approach which considers total scour as a series of components that can be broadly grouped into event scour and long-term bed elevation change. The gravel riverbed at the site meant that bedform scour was not considered (as this is a sand bed river phenomenon), and the planform configuration and bed material at the meander preclude use of the USDA bend scour equation. Therefore, the event scour assessment at Llanegwad was limited to an empirical determination of general scour combined with an adjustment based on professional judgement for other scour processes including scour associated with a tight river bend and scour amplification due to the retaining wall. The empirical general scour equations of Lacey, Blench, and Blodgett (USDA, 2007).

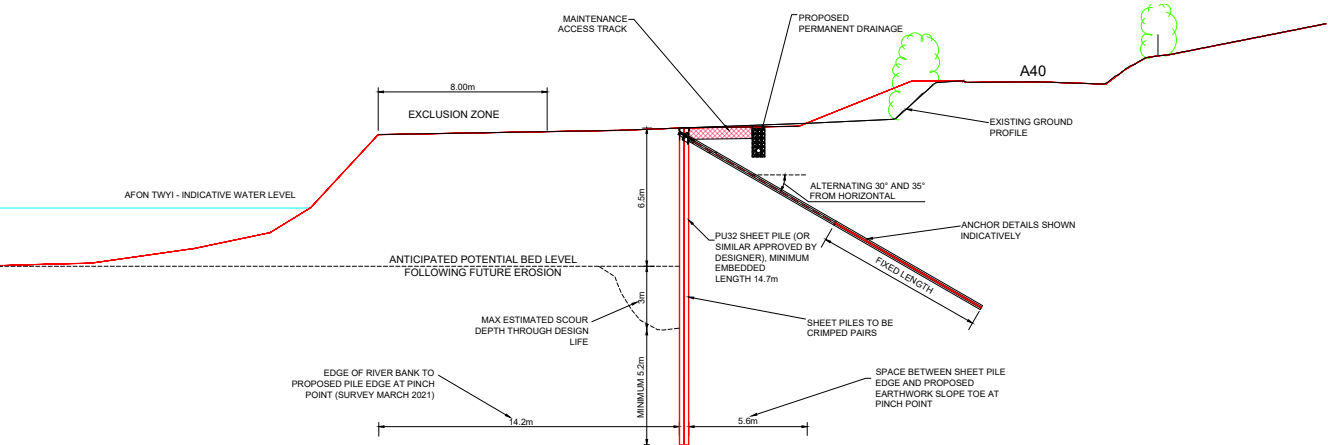
A maximum scour depth of 2.69m was established the equation by Blodgett's method (USDA, 2007). From this, a total scour allowance up to 3m was determined. This accounts primarily for event scour, but also recognises the risk of long-term change in bed elevation during the lifetime of the scheme. Following the scour assessment, a maximum retaining wall height of 9.7m was determined, comprising 6.7m to the base of the riverbed and an additional 3m below riverbed during scouring events.

4.4 PROPOSED DESIGN

From assessing the risk the River Towy poses, and how these will evolve over time, a detailed design for the embedded sheet pile wall with ground anchor support could now be undertaken. The final design comprised a 240m long anchored sheet pile wall with a minimum embedment length of 14.7m (Figure 3). 16m long ground anchors which had an 8m fixed bond length were installed at alternating 30° to 35° angles from horizontal, with a 1.2m spacing along the sheet pile wall.

FIGURE 3

Anchored sheet pile wall arrangement





The construction of the sheet pile wall was completed Summer 2022 without any significant issues. The benefit of the structure being a singular design (as opposed to a hybrid solution) allowed for a greater ease of construction and enabled the Contractor to quickly become familiar with the installation methodology and adapt it to suit the site conditions. This relatively simple method of construction also limited the impact to the surrounding landscape and the adjacent SSSI and SAC sites. Furthermore, this removed the potential complexity associated with the integration of the different design elements and likely associated delays, and construction was completed within the anticipated programme timescale. In the as-built design, the retaining wall was fully embedded with no visible signs of hard engineering except for the pile cap. The double corrosion protected anchors, in combination with the use of an inert backfill in front of the sheet piles in the zone of the anchor heads, allowed for a reduced maintenance frequency during the early years of the scheme. The material used in the construction and operation of the temporary piling platform was reclaimed post-construction and subsequently reused as fill to the A40 shoulder widening, allowing the area to be returned to grassland.



## **5. Conclusion**

---

The constructed anchored sheet pile wall solution was identified as the optimal river erosion mitigation measure, providing a resilient design against future behaviours of the River Towy and taking into account a changing climate. This design was based on an intensive geomorphological assessment, which proved critical in determining the level of required resilience and spatial extent of the protection to the A40. The alignment of the wall was designed so that the flow of the River Towy would be redirected into existing palaeochannels, encouraging the river to flow in the path of least resistance away from the critical A40. By gaining an understanding of the past movements of the River Towy and anticipating how future changes in climate will influence the planform migration, an appropriate solution was determined to build resilience into the asset.



## **Acknowledgements**

---

This paper was originally presented at the British Geotechnical Association (BGA) Geo-Resilience 2023 conference that took place in Cardiff on March 28-29th, 2023.

## References

---

- › Macklin, M., & Harrison, S. (2012). Geomorphology and Changing Flood Risk in the UK.
- › Natural Resources Wales (NRW). (2022). Lle, A Geo-portal for Wales; LiDAR Composite Dataset. (Welsh Government) Retrieved 2022, from <http://lle.gov.wales/Catalogue/Item/LidarCompositeDataset/?lang=en>
- › Schumm, S. (1973). Geomorphic thresholds and complex response of drainage systems. In *Fluvial Geomorphology* (pp. 69-85).
- › USDA. (2007). Stream Restoration Design (National Engineering Handbook 654) Technical Supplement 14b Scour Calculations. [online] USDA. Available at: <Stream Restoration Design (National Engineering Handbook 654) | NRCS ([usda.gov](https://www.nrcs.usda.gov))> [Accessed 09 June 2021].
- › Welsh Government. (2021). Flood Consequence Assessments: Climate change.













**Jim Whiteley**

Principal Engineering Geophysicist  
Engineering Services – Infrastructure UK  
Birmingham, UK



**Edward Cox**

Senior Geophysicist  
Engineering Services – Infrastructure UK  
London, UK



**Ady Koe**

Chief Geotechnical Engineer  
Engineering Services – Infrastructure UK  
Bristol, UK

## 07. Geotechnical Engineering

# Perspectives on Practical Tools, Best Practice, and Emerging Technologies in the Application of Geophysics for Enhancing Resilience to Geohazards

### Abstract

Geophysical methods contribute to improved georesilience by providing high-resolution and multi-dimensional subsurface information using non-invasive approaches. Emulating these attributes over the same spatial extent using intrusive methods can be expensive, time consuming, and can carry a higher carbon footprint. The use of geophysics in ground engineering is well established, particularly as part of ground investigation. However, recent technological developments in the field stand to deepen the integration of geophysics and intrusive investigation to improve georesilience, particularly in the context of geohazards. These technological developments include: i) the maturation of 3D geophysical imaging techniques to solve 3D geotechnical problems; ii) better integration of data using multi-method geophysical surveys and/or field-estimated or laboratory-measured geotechnical properties; and, iii) improved data inversion, integration, interpretation, and visualisation using open-source, community-supported software packages.

In this paper, we aim to contextualise these technical developments within the cultural change that is taking place across the ground engineering community with regards to how we gather, manipulate, and present geohazards data. This change has seen an increasing recognition for the need to investigate, model, and interpret ground conditions using multi-dimensional, high-resolution digital data.

We present an example of a 3D electrical resistivity tomography survey to characterise potential karst features, and the role this data plays in increasing georesilience by contributing high-resolution, spatially continuous data to improve our understanding of geohazards.

**KEYWORDS**

Geophysics; Geohazards; Ground engineering; 3D



## 1. Introduction: Engineering Geophysics in the Digital Era

---

There has been a paradigm shift in the use of digital geoscientific data in ground investigation in the last 50 years. Discussion around the relative importance and systemic benefits and challenges posed by new technologies is active (e.g., Griffiths, 2019, Hearn, 2019). However, recent innovations in cost-effective and user-friendly digital technologies, coupled with dramatic increases in computing power and affordability, have permanently changed the way that geoscientific data are acquired, analysed, stored, and shared for the purposes of ground engineering (McCaffrey et al., 2005). As geoscientific datasets increase in coverage, resolution, accuracy, and diversity of application, new analytical solutions are being sought from the fields of data science to help analyse increasing volumes of data (Bergen et al., 2019).

Fortunately, the engineering geology and geotechnical communities have largely embraced digital geoscience. Consequently, the concept of the 3D engineering geological model and its function in storing and understanding the spatial distribution of subsurface discontinuities, engineering properties and their changes over time is one that has evolved alongside technological developments in recent years (Culshaw, 2005, Fookes, 1997). Geophysical investigation has always played a niche but important role in ground investigation. It is interesting to note that the Engineering Geology Unit of the British Geological Survey (BGS), first started in the 1960s, included the use of geophysics as a core part of its activities from its creation (for a history of engineering geology within the BGS, see the summary by Culshaw et al., 2019), and was an early adopter of the term “engineering geophysics” within the context of UK engineering geology practice (Hooper, 1983).

However, despite geophysics embracing and benefitting from many leaps in digital technologies in recent decades (e.g., hardware miniaturisation, better battery and data storage, wireless telecommunications, increased computing power and affordability, open-source software development), the way in which geophysics is applied to site investigation has changed little in recent decades, typically either being employed to screen sites prior to intrusive investigation, or to delineate unexpected features arising during intrusive works that might prove problematic or hazardous to further ground investigation. In the experience of the authors, geophysical survey deliverables still typically comprise 2D graphical representations of data rather than digital models that can be visualised and analysed in a 3D environment.

More widely, the challenges faced by geophysicists operating in the ground engineering sphere as summarised by Annan (1997) over two decades ago could still apply in some cases today. These challenges include understanding the requirements of engineers and communicating geophysical results in an understandable format, quantifying cost benefits, and maintaining professional standards of practice.

In this paper, we highlight three major developments that stand to improve the usefulness and integration of geophysical investigations within ground engineering, particularly within the context of ground investigation for hazard identification. These developments include i) the maturation of 3D geophysical imaging techniques to solve 3D geotechnical problems; ii) better integration of data using multi-method geophysical surveys and/or field-estimated or laboratory-measured geotechnical properties and relationships; and, iii) improved data inversion, integration, interpretation, and visualisation using open-source, community-supported software packages. We suggest these points as key areas as they align with trends in how 3D digital datasets for ground modelling (outside of geophysics) are obtained, analysed, and visualised.

To demonstrate these developments in practice, we present the results of a 3D electrical resistivity tomography (ERT) survey used to investigate the ground for areas of variable lithology and strength, including the presence of potential sinkholes and karst features, in the East Midlands, England. ERT has been used in many previous studies to delineate subsurface karstic features (see examples by Cheng et al., 2019, Nyquist et al., 2007, Zhu et al., 2011). Although using 3D ERT is not a novel approach to mapping subsurface karstic features, its use beyond academic studies as part of a commercial ground investigation is still relatively uncommon. Hence, in addition to demonstrating the technical benefits of 3D ERT, we highlight the novel and integrated phased approach to both the intrusive and geophysical investigations of the site.



## 2. Methods and Materials

---

### 2.1 ELECTRICAL RESISTIVITY TOMOGRAPHY

In a typical ERT survey, tens of electrodes are placed at shallow depths (10 – 20cm) in a linear array along the ground surface. A resistivity meter connected to the electrode array via multi-core cables collects a pseudo-section of apparent resistivity measurements. Measurements are made by injecting DC current across a pair of (current) electrodes, and the potential is measured over a second pair of (potential) electrodes. From this, the bulk apparent resistivity of the ground at a point relative to the geometry of the surface electrodes is measured (Loke et al., 2013).

Depth of the apparent resistivity measurement is proportional to the spacing between the electrodes used for the measurement, with lateral position controlled by which electrodes are used along the profile. The depth of the shallowest and deepest reading is governed by the minimum spacing between electrodes and total number of electrodes used, respectively. Hence, there is a trade-off between resolution and depth of investigation that needs to be balanced for the survey aims. In any case, there will always be a decrease in resolution with depth relative to near-surface measurements, which is a consideration in all geophysical methods. A measurement of resistivity is influenced by several factors in the ground, primarily the presence and conductivity of pore fluids (the presence of which will reduce resistivity), lithology (resistivity of rocks and soils varies over 20 orders of magnitude), the clay content of the material (the presence of clay reduces resistivity), and the porosity of the medium (with increased porosity tending to increase resistivity if pores are air-filled).

Field ERT data are inverted to produce modelled cross-sections of resistivity. Inversion can broadly be regarded as the opposite of forward modelling. In a forward model, the model is known and data are predicted (e.g., calculating the magnetic field lines of a bar magnet with known dimensions and magnetic strength). The opposite is true for an ERT survey; the data (e.g., the magnetic field lines) are known, but the model (the dimensions and strength of the bar magnet) is not, and so data inversion iteratively minimises (through repeated inversion and forward modelling) the misfit between observed data and a modelled solution.



Different models can produce the same data, a concept known as “non-uniqueness” (e.g., a large, weakly magnetic bar magnet can produce a similar magnetic field to a small, strongly magnetic bar magnet). It is therefore pertinent to keep in mind that the outputs of geophysical inversion are modelled solutions and not direct measurements of the ground conditions; the map is not the territory.

Where there are localised variations in ground conditions adjacent to an ERT profile, the injected current can be distorted by these off-line features (particularly where conductive features are present, through which current might preferentially flow). These off-profile distortions can create data artefacts in 2D models and are commonly referred to as “3D effects” (Dahlin et al., 2007). Data artefacts from 3D effects can be mitigated by using multiple 2D profiles to acquire parallel profiles of data at regular intervals and then inverting the data from all profiles using a 3D inversion algorithm, as opposed to inverting individual profiles using a 2D algorithm (Dahlin and Loke, 1997). The specification for a successful 3D survey is more intensive than a 2D survey due to the higher density of data coverage required, and the inversion of data is far more computationally expensive. However, the result of this process is a single 3D volume of data. In heterogeneous environments, this approach can provide far more insight into ground conditions than by using sparsely separated 2D profiles, which i) may also suffer from 3D effects not accounted for in the inversion process, and ii) may still not capture small-scale heterogeneity in ground conditions in the spaces between individual profiles.



### 3. Welby Overflow Site Investigation

---

#### 3.1 PROJECT RATIONALE AND SITE DESCRIPTION

The Welby Overflow (WO) site comprises the northern parts of two arable fields (eastern and western fields) located approximately 6.6km east of Grantham and 1.3km south of the village of Welby in Lincolnshire, England (**Figure 1**). The site is being developed as part of Anglian Water's Strategic Pipeline Alliance (SPA), which will construct hundreds of kilometres of interconnected water mains across the east of England to build resilience across the network. A tank, lagoon, and pumping station are planned for construction at the WO site.

A potential risk to this development is the presence of karst and eroded surfaces at the upper boundary of the Upper Lincolnshire Limestone Member (ULLM). The ULLM is described as an ooidal and shell fragmented grainstone. Superficial deposits comprising mid-Pleistocene glaciofluvial deposits of sands and gravels are mapped across parts of the site, which may infill topographic incisions and depressions of the upper surface of the ULLM. This presents several risks including differential settlement, channelised drainage of subsurface water, and associated washout (Waltham and Fookes, 2003). Mapping the scale and location of these features allows for risks to be minimised in design, enhancing long-term resilience of the planned structures.

A historic borehole (BGS Reference: SK93NE18) is located in the north-eastern corner of the eastern field. This borehole indicates a 0.76m thick cover of superficial deposits overlying oolitic limestone extending to 24.72m bgl. A 0.3m band of clay is identified at the base of this oolitic limestone and is underlain by limestone to a depth of ~28m bgl, at which point a transition zone of sandy clay and ironstone is identified above the blue clays of the Upper Lias Formation at ~29m bgl.

#### 3.2 INITIAL GEOPHYSICAL AND GROUND INVESTIGATION

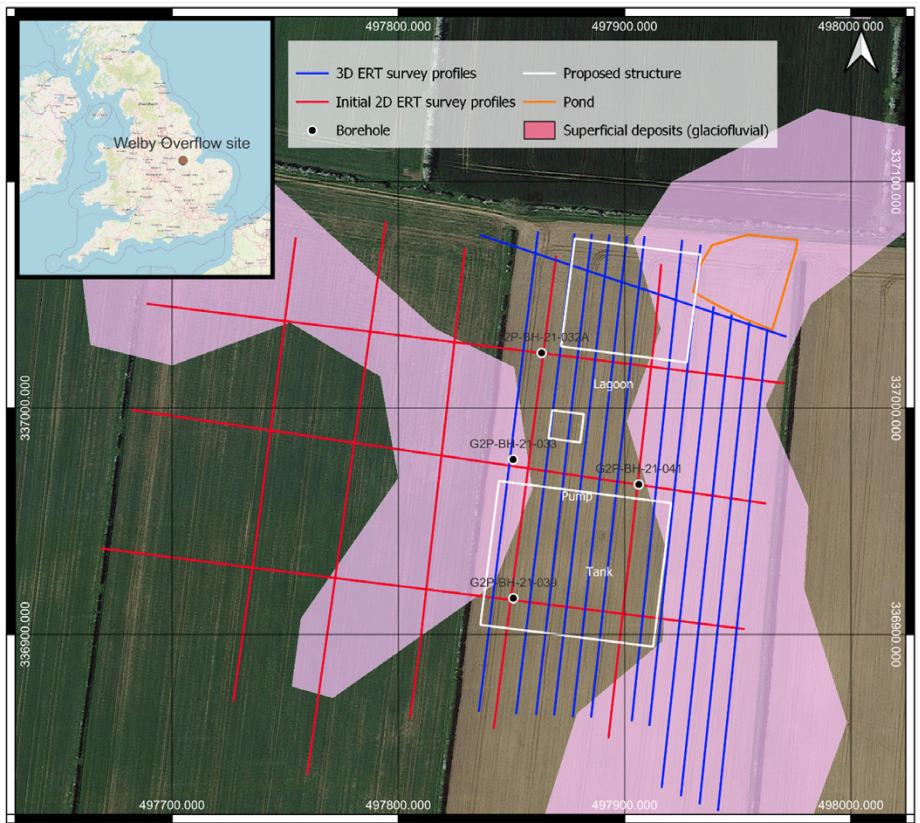
To identify areas of superficial deposits and strength variations in the ULLM, SPA commissioned a geophysical survey of parts of the eastern and western fields at the WO site. This survey was undertaken by TerraDat in December 2021 and March 2022 (the second phase of geophysics taking place after initial intrusive ground investigation, which was undertaken in February 2022). The initial geophysical survey used electromagnetic (EM) surveying and 2D ERT profiles to map the glaciofluvial deposits at the WO site.

The EM survey mapped the lateral extents of the glaciofluvial deposits (which are markedly more conductive than the ULLM due to their increased clay content), and several ERT profiles indicated variations in the 2D resistivity profile of the ULLM interpreted as potential clay-rich infill material. Furthermore, deeper conductive features in the ERT profiles were interpreted as geological boundaries, potential solution features or fracture zones.

The initial phase of ground investigation confirmed the variable thickness of glaciofluvial sands, clays, and gravels across the WO site. The western field was shown to have significantly increased thicknesses of glaciofluvial deposits in areas corresponding to increased conductivity in the EM survey and decreased resistivity (the inverse measurement of conductivity) in the ERT sections. For this reason, the locations of the proposed tanks were moved to the eastern field. However, the TerraDat EM survey was not specified to completely cover the eastern section of this field and the ERT profiles provided only sparse coverage in the east. Furthermore, BGS mapping indicates further glaciofluvial deposits in the eastern part of the field. Hence, SPA commissioned a follow-up geophysical survey by Atkins to extend the footprint of the original survey undertaken by TerraDat, and to provide high-resolution 3D data to identify variability of the ULLM and thickness of overlying glaciofluvial materials.

FIGURE 1

Map of the Welby  
Overflow site





### 3.3 3D ERT SURVEY ACQUISITION

Atkins designed the 3D survey to incorporate previous profiles acquired by TerraDat, reducing the need for acquiring additional data on site by ~15%. We acquired 13 additional ERT profiles at regular intervals (~8m apart) situated between the existing north-south orientated TerraDat profiles (located ~50m apart). The data acquisition files for the Syscal Pro resistivity meter were designed to the same specification as the TerraDat surveys, using a Wenner-Schlumberger configuration set to investigate up to 20m bgl. The survey was completed in November 2022, and to complete the survey in four days, electrodes were deployed at 3m spacing (the TerraDat survey used 2m spacing). A pond located in the north-eastern corner of the field was identified during the pre-survey walkover, and the four eastern profiles had to be moved south to accommodate this feature. Field quality control and assessment showed the data quality to be high, with all individual model 2D inversions converging with root-mean square (RMS) errors of less than 5% after three inversion iterations.

We processed the 15 ERT profiles (2 profiles from the TerraDat survey and 13 from the Atkins survey) using two inversion algorithms; firstly using the open-source, Python-based ERT inversion software ResIPy (Blanchy et al., 2020), and secondly the licensed inversion software Res3DInv (Loke and Barker, 1996). Both inversions used an estimated error model, as field error data from reciprocal measurements were unavailable. Nevertheless, the ResIPy model converged after three inversions with an RMS error of ~1% and the Res3DInv model converged with an RMS error of 1.82% after 7 iterations. Both models showed good agreement on the 3D distributions of resistivity values across the area surveyed. Due to the spacing between profiles being slightly larger than optimal (profile spacings should typically approximately double the electrode spacing), some data artefacts are present in the near surface (top 2m) of both models, which present as linear extents of marginally lower resistivity between the surveyed profiles. However, these artefacts are minor and are not present at the depths under investigation. The results of the Res3DInv model are presented in this study, as the model provides better resolution at depth and smoother resistivity distributions. However, the ResIPy model would still lead to the same conclusions being drawn in the following analysis.

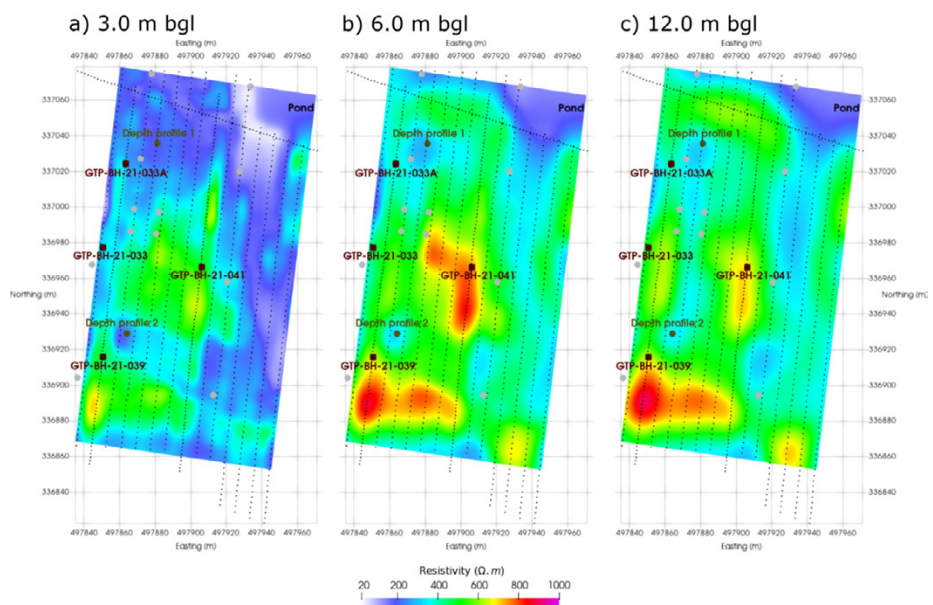
## 4. Results and Discussion

### 4.1 3D ERT SURVEY RESULTS

We trimmed the extents of the 3D block to remove areas of poor coverage due to profile displacements (except the north-eastern corner where the pond was located, which is disregarded in the model analysis). The model resistivity ranges from 20 – 1,000 $\Omega$ .m, with deeper parts of the model showing higher resistivity values (**Figure 2**). The hypothesis for interpreting the data is that stronger limestone should present as area of increased resistivity, as dissolution, fracturing (especially where fractures show clay infill), and increased saturation (which should lower bulk resistivity) will weaken the ULLM rock mass and reduce resistivity.

**FIGURE 2**

Depth slices at a) 3m, b) 6m, and c) 12m bgl through the 3D electrical resistivity tomography model. Electrode positions indicated by black dots, corners of proposed structures indicated by grey dots.



We interpret the area of low resistivity ( $\sim 20\Omega$ .m) in the north-eastern corner (**Figure 2a**) as shallow seepage of surface water from the surface pond. At 6m and 12m bgl (**Figures 2b** and **2c** respectively), north-south trending zones of lower resistivity are observed, interspersed with zones of higher resistivity values. We interpret these features as areas of glacial scouring, potentially infilled by glaciofluvial sediments. The widest of these features, to the east of the survey area, corresponds to a mapped deposit of glaciofluvial deposits (**Figure 1**), and the resistivity of this features may be reduced by seepage of surface water from the pond at the surface.

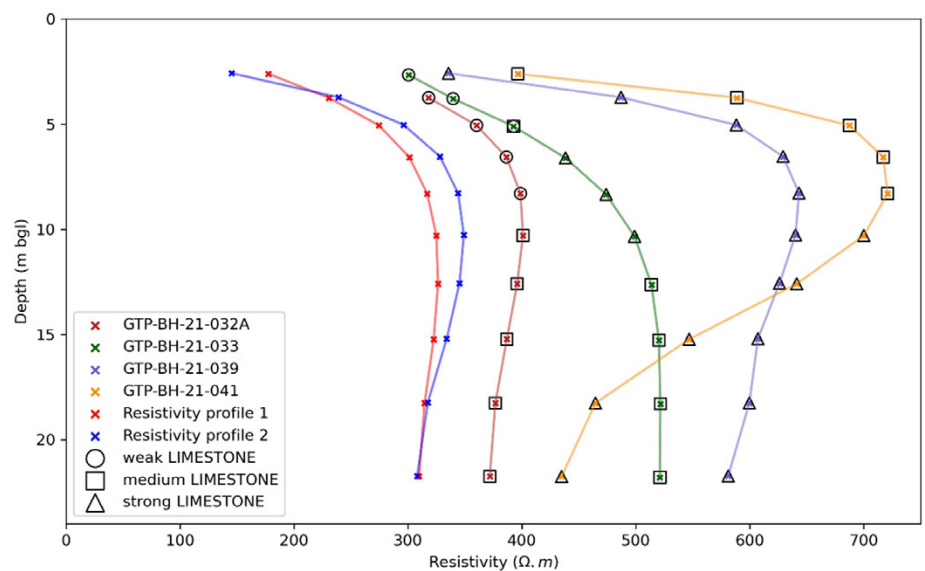


#### 4.2 INTEGRATION OF GEOPHYSICAL RESULTS WITH BOREHOLE DATA

The four boreholes drilled within the area of the 3D ERT survey identify the upper boundary of the ULLM between 1.7 and 2.8m bgl. The engineering logs described the ULLM in three states: weak, medium, and strong. Fractures are identified across all logs, with fracture indices ranging from 2 to 18. To identify zones of potential weaker ULLM, or zones of infill with glaciofluvial material, we extract the modelled resistivity values from each borehole location for depths at which limestone is recorded (**Figure 3**). From the four resistivity depth profiles, we indicate where weak, medium, and strong limestones are recorded. Although there is significant variability in the resistivity of strong limestones (~350 - ~720 $\Omega$ .m) and medium limestone (~380 - ~720 $\Omega$ .m), all recorded instances of weak limestone show resistivity values of less than 400 $\Omega$ .m. A key assumption is that there is statistical correlation between the one borehole showing both weak limestone and low resistivity, and that this correlation can be extended across the entire model. However, previous studies show that karstic features tend to manifest as areas of lower resistivity (e.g., Nyquist et al., 2007). It is worth noting that large volumes of the 3D ERT model show resistivity values <400 $\Omega$ .m (**Figure 2**), although this should not be taken as a definitive threshold at which weaker limestones are present.

**FIGURE 3**

Resistivity-depth profiles from the four boreholes drilled within the 3D ERT survey area, and two locations of low resistivity within the bounds of proposed structures. Strength of limestone from engineering logs of the borehole resistivity-depth profiles.



Although a direct relationship between resistivity and strength of the ULLM is unlikely to exist, we extract two resistivity profiles from the 3D models to investigate the resistivity-depth relationship of two low resistivity zones within the footprint of the lagoon and tank structures (see "Depth profiles" locations, **Figure 2**).

These locations both show resistivity values lower than those points recorded as weak limestone in the boreholes, suggesting the presence of weak limestone and/or increased clay content in these zones. Hence, these areas have been marked for follow-up drilling to investigate the cause of these low resistivities.



## 5. Conclusions

---

This study highlights that the product of a 3D geophysical survey is a multi-dimensional, high-resolution digital model that provides extensive insight into the distribution of engineering properties. The heterogeneity of some environments, such as karst settings, can vary significantly across small distances, and can be difficult to capture using intrusive methods alone. In this study, three of the four boreholes encountered strong ULLM. However, the ERT survey suggests that the proportion of strong limestone may be much lower across the site, and large volumes of the 3D model showing resistivity values lower than that of intact limestone. At the time of writing, further boreholes are being planned to investigate the low-resistivity features identified in the 3D ERT model. It will be interesting to integrate this data further into the analysis undertaken in this paper and explore the use of automatic classification techniques to identify geophysical-geotechnical relationships (e.g., Whiteley et al., 2021).

Geophysical surveys, particularly when undertaken in 3D, are uniquely placed to fill an important knowledge gap that sits between the high-resolution, but surface-only, observations gleaned from remote sensing, and the detailed but extremely localised data from intrusive ground investigation. In this sense, geophysical surveys can be considered a vital source of information with which to supplement 3D model development, particularly in the context of identifying geohazards associated with heterogeneous ground conditions.

## **Acknowledgements**

---

The authors present with the permission of SPA and acknowledge V. Tibra, M. Edmondson, L. Henriques, I. Griffiths, and C. Tan for their input, and especially thank Chloe Rushworth (Atkins) for her efforts in the field. This paper was first published at the British Geotechnical Association's Geo-Resilience conference in the UK. The paper is reproduced here with permission of the British Geotechnical Association.



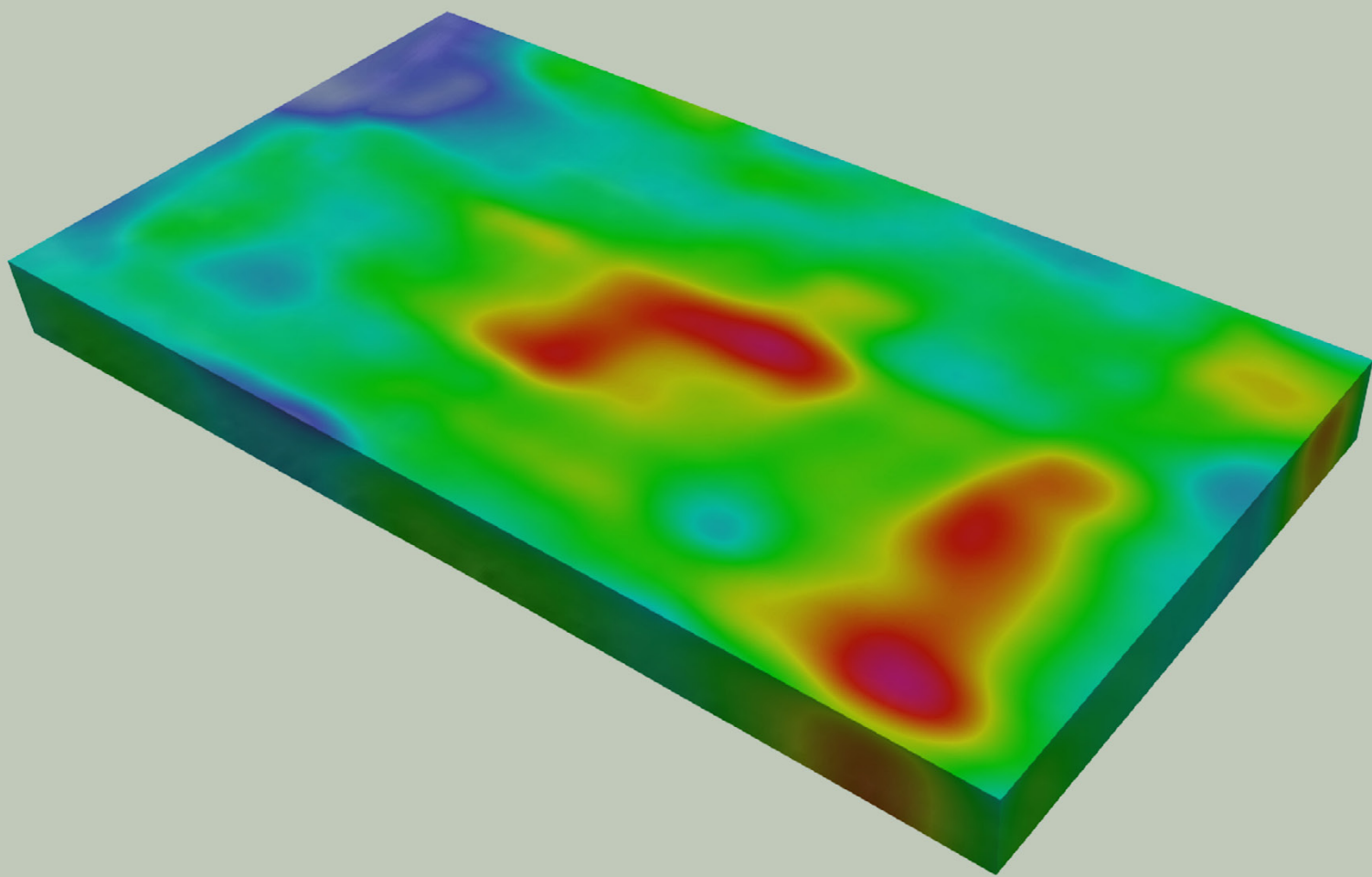
## References

---

- › Annan, A. P. (1997). Engineering and environmental geophysics: the future. 12, 419-426.
- › Bergen, K. J., Johnson, P. A., De Hoop, M. V. & Beroza, G. C. (2019). Machine learning for data-driven discovery in solid Earth geoscience. *Science*, 363, 0323.
- › Blanchy, G., Saneiyan, S., Boyd, J., McLachlan, P. and Binley, A. (2020). ResIPy, an Intuitive Open Source Software for Complex Geoelectrical Inversion/Modeling. *Computers & Geosciences*, February, 104423. <https://doi.org/10.1016/j.cageo.2020.104423>.
- › Cheng, Q., Chen, X., Tao, M. & Binley, A. (2019). Characterization of karst structures using quasi-3D electrical resistivity tomography. *Environmental Earth Sciences*, 78, 285.
- › Culshaw, M. G. (2005). From concept towards reality: developing the attributed 3D geological model of the shallow subsurface. *Quarterly Journal of Engineering Geology and Hydrogeology*, 38, 231-284.
- › Culshaw, M. G., Northmore, K. J. & McCann, D. M. (2019). A Short History of Engineering Geology and Geophysics at the British Geological Survey—Part 2: Engineering Geological Mapping. Cham. Springer International Publishing, 45-52.
- › Dahlin, T. & H. Loke, M. (1997). Quasi-3D resistivity imaging - mapping of three dimensional structures using two dimensional DC resistivity techniques.
- › Dahlin, T., Wisén, R. & Zhang, D. (2007). 3D Effects on 2D Resistivity Imaging – Modelling and Field Surveying Results.
- › Fookes, P. G. (1997). Geology for Engineers: the Geological Model, Prediction and Performance. *Quarterly Journal of Engineering Geology and Hydrogeology*, 30, 293-424.
- › Griffiths, J. S. (2019). Advances in engineering geology in the UK 1950–2018. *Quarterly Journal of Engineering Geology and Hydrogeology*, 52, 401-413.
- › Hearn, G. J. (2019). Discussion on 'Advances in engineering geology in the UK 1950–2018', *Quarterly Journal of Engineering Geology and Hydrogeology*, 52, 563-568.



- › Hooper, J. W. (1983). Engineering geophysics. *Quarterly Journal of Engineering Geology and Hydrogeology*, 16, 247-249.
- › Loke, M. H. & Barker, R. D. (1996). Rapid least-squares inversion of apparent resistivity pseudosections by a quasi-Newton method 1. *Geophysical prospecting*, 44, 131-152.
- › Loke, M. H., Chambers, J. E., Rucker, D. F., Kuras, O. & Wilkinson, P. B. (2013). Recent developments in the direct-current geoelectrical imaging method. *Journal of Applied Geophysics*, 95, 135-156.
- › Mccaffrey, K. J. W., Jones, R. R., Holdsworth, R. E., Wilson, R. W., Clegg, P., Imber, J., Holliman, N. & Trinks, I. (2005). Unlocking the spatial dimension: digital technologies and the future of geoscience fieldwork. *Journal of the Geological Society*, 162, 927-938.
- › Nyquist, J. E., Peake, J. S. & Roth, M. J. S. (2007). Comparison of an optimized resistivity array with dipole-dipole soundings in karst terrain. *GEOPHYSICS*, 72, F139-F144.
- › Waltham, A. C. & Fookes, P. G. (2003). Engineering classification of karst ground conditions. *Quarterly Journal of Engineering Geology and Hydrogeology*, 36, 101-118.
- › Whiteley, J., Watlet, A., Uhlemann, S., Wilkinson, P., Boyd, J. P., Jordan, C., Kendall, J. M. & Chambers, J. E. (2021). Rapid characterisation of landslide heterogeneity using unsupervised classification of electrical resistivity and seismic refraction surveys. *Engineering Geology*, 290, 106189.
- › Zhu, J., Currens, J. C. & Dinger, J. S. (2011). Challenges of using electrical resistivity method to locate karst conduits—A field case in the Inner Bluegrass Region, Kentucky. *Journal of Applied Geophysics*, 75, 523-530.











**Dr. Dena Servatian**

Engineer II

Engineering Services – Transportation UK  
Birmingham, UK



**Richard Bryn Williams**

Senior Engineer

Engineering Services – Transportation UK  
York, UK

## 08. Rail Engineering

# Electromagnetic Compatibility Integration on Major Railway Projects

### Abstract

In recent years, Electromagnetic Compatibility (EMC) assurance within the rail sector has become more formalised and procedural in response to proving compliance against a range of different standards and legislative requirements. This paper explores this assurance process in the context of major rail projects; detailing the activities, deliverables and best practices employed when providing evidence of EMC during a typical project lifecycle. Additionally, the report also looks at the application of Atkins' Traction Modelling Simulator (ATMS) and how simulation plays a key role in the design and development of a safe, reliable and efficient railway.

### KEYWORDS

ATMS; Electromagnetic Compatibility; Electrical systems assurance; GRIP; Modelling; Network Rail; PACE; Railway

## 1. Introduction

---

Progressive Electromagnetic Compatibility (EMC) assurance forms a vital part of any project life cycle. Documentation may be used to establish a variety of technical requirements, define the legal responsibilities as well as identify general best practices for those involved, thus evidencing that EMC has been considered and implemented where applicable.

When considering the challenges of a complex major railway project, the level of EMC assurance required can increase substantially. Stakeholders, operators, designers and contractors must all be able to clearly understand and execute their duties, from effective coordination during the design and construction phases, right through to maintaining the safe and effective operation of any systems. For complex projects, electrical systems modelling can act as a key element in ensuring the adequacy of EMC controls for the railway; providing designers with a range of design parameters and operational constraints that are necessary to ensure EMC of the final system.

This paper will focus on how EMC is controlled, managed and executed within the context of major rail electrification projects, and highlight how EMC assurance has evolved in line with recent changes to the rail delivery framework process. It defines the various documents and activities which are mandated throughout the project life cycle to achieve EMC assurance under the relevant legislations and standards.





## 2. History of Assurance

---

To meet the requirements of previous legislation; including the EMC Directive 89/336/EEC [1] and the UK regulations SI 1992/2372 [2], projects would previously have mandated the standards and processes relevant to EMC assurance as contractual, rather than legal requirements. This enabled projects and companies to have a degree of flexibility in providing the necessary conformance evidence against the relevant standards but did not provide a consistent or effective overarching process for EMC assurance across projects of different sizes and complexities.

In the early years of the new millennium, both the EU EMC Directive and subsequently the UK EMC Regulations were updated (in 2004 [3] and 2006 [4] respectively). One of the most significant changes following these revisions was that the concept of fixed installations now fell within the scope of EMC assurance. A fixed installation is defined as a particular combination of different apparatus that is assembled, installed and operational at a specific location. When applying this description to the context of a railway system, this covered a significant degree of the infrastructure.

To comply with the new regulations and reduce the level of regulatory burden placed on manufacturers, Network Rail (NR) and others in the rail industry were therefore required to define and maintain a clear and coordinated approach to EMC assurance throughout the entire lifecycle of their projects. The principal basis of any such methodology provides a project with a comprehensive set of verifiable evidence and traceable activities to satisfy that all applicable EMC requirements and specifications have been met.

Over time, different organisations developed different company standards outlining their EMC assurance; notable examples within the UK include the EMC Strategy and EMC Assurance Process for Network Rail (NR/L1/RSE/30040 [5] and NR/L2/RSE/30041 [6] respectively), London Underground's Electromagnetic Compatibility Standard (LUL S1222 [7]) and the Docklands Light Railway EMC standard (DLR-ENG-STD-ES102 [9]).

The Regulations also required the companies to identify an EMC Responsible Person for the various installations. This individual was tasked with the legal duty to provide the necessary evidence that any new or modified installation was compliant with the requirements of the Regulations. Although the responsible person did not themselves have to be competent in EMC engineering, the role required them to ensure the project had access to such skills so this responsibility could be delegated as required during the project lifecycle.

Whilst the various group standards, national regulations and international legislation have all gone through several updates over the years (notable recent changes include updates to the EU legislation; 2014/30/EU [10], the UK EMC Regulations; SI 2016/1091 [11], and more recently the changes arising from the United Kingdom's departure from the European Union which includes the transition from equipment CE marking to UKCA, and the role of UK Conformity Assessment Bodies), the underlying concept for all these standards remains predominantly the same; EMC engineering and assurance in the railway has to be documented and auditable, with the evidence readily available for the duration of the installation's lifecycle.



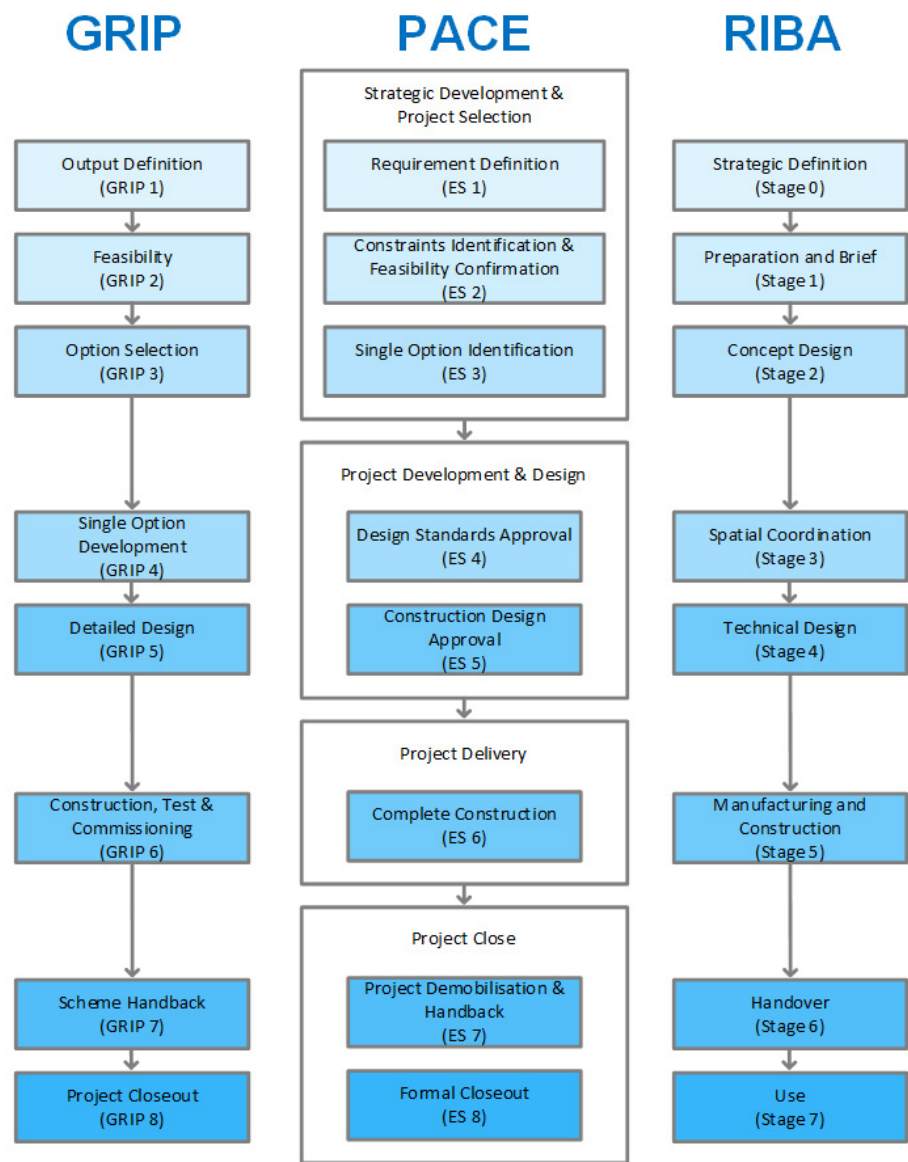
### 3. Business as Usual


---

In the UK, railway projects that are managed and controlled under Network Rail's authority typically followed the Governance for Railway Investment Projects (GRIP) procedure. In December 2010, NR/L1/INI/PM/GRIP/100 (NR policy manual for GRIP) [12] was issued which detailed a simplified approach to manage projects with the aim of minimisation and mitigation of the risks associated with delivering the projects. GRIP was normally used in the projects that involve enhancement or renewal of the operational railway or high street environment works. The GRIP approach defined eight key stages which correlated against various phases of a project lifecycle. The various EMC assurance activities were aligned against each of the GRIP Stages, inherently creating a systematic process to obtain the appropriate levels of evidence for each phase, and confidence that EMC was being considered throughout.

In March 2021, Network Rail proposed a new method of managing and controlling railway projects; Project Acceleration in a Controlled Environment (PACE) [13]. The nature of GRIP and PACE methods are the same, but the main difference between these two methods is that PACE can provide a more flexible control structure which enables sponsors and project managers to adapt the controls to meet the project requirements in a more efficient way. PACE includes four phases with milestones in each phase. There are eight milestones in total for the whole project lifecycle and each milestone corresponds to a legacy GRIP Stage. Although the four PACE phases need to be followed sequentially (like GRIP Stages), there is a flexibility in milestones in each specific phase; for example, stages may run concurrently, in different sequences or even omitted entirely for smaller, less complex projects.

FIGURE 1  
Comparison of GRIP, RIBA  
and PACE methods





The eight key stages of NR project governance (for both GRIP and PACE) as shown in **Figure 1** may broadly be identified by the following descriptions:

1. **Output Definition:** At this early stage, the overall project requirements and aims of any works are clearly defined, typically following a period of stakeholder consultation.
2. **Feasibility:** The scope of investment as well as any constraints or project limitations is defined at this stage. In addition, the project team looks to seek confirmation that the outputs and project requirements defined in Stage 1 are economically viable and aligned to the organisational strategy. As per the NR EMC Assurance Process (NR/L2/RSE/30041 [6]), it is at this stage that EMC should start to be considered by the project.
3. **Option Selection:** Once the feasibility is confirmed, this is essentially the first stage of design. One or more design solutions for achieving the project requirements are developed and then assessed for viability to determine the most appropriate option for progression.
4. **Single Option Development:** Also known as outline design, the agreed solution from Stage 3 is developed to the point where the stakeholders may grant an Approval in Principle (AiP) to the design (note: an AiP may also be granted at Stage 3 of the design lifecycle, depending on the nature and complexity of the project). At this stage, whilst specific equipment and design details may not be finalised, there are several EMC assurance activities which can take place; including design reviews and Hazard Identification (HazID) assessments (see Sections 4.4 and 4.3 respectively).
5. **Detailed Design:** The output of this stage of works is essentially the fully approved and construction ready design to which the project will be built. All EMC evidence pertaining to design assurance shall be collated, assessed and verified ready to progress to the construction phase of the project.



6. **Construction, Test and Commissioning:** The project is physically built to the specifications and requirements stipulated within the approved design. For EMC, this means procuring and installing the appropriate equipment, and ensuring that the systems are tested and commissioned in accordance with the design.
7. **Handback:** The project team transfers asset responsibility back to the operator and maintainer team at this stage.
8. **Closeout:** Finally, the project is formally closed out and project support systems are formally closed. At this stage, all remaining EMC responsibilities are typically relinquished back to the maintainer and stakeholder.

In addition to GRIP and PACE, some projects may also adopt the Royal Institute of British Architects (RIBA) Plan of Work (PoW) [14]. The PoW is largely analogous to the NR delivery stages; with projects delivered across the eight key stages across the entire project lifecycle.

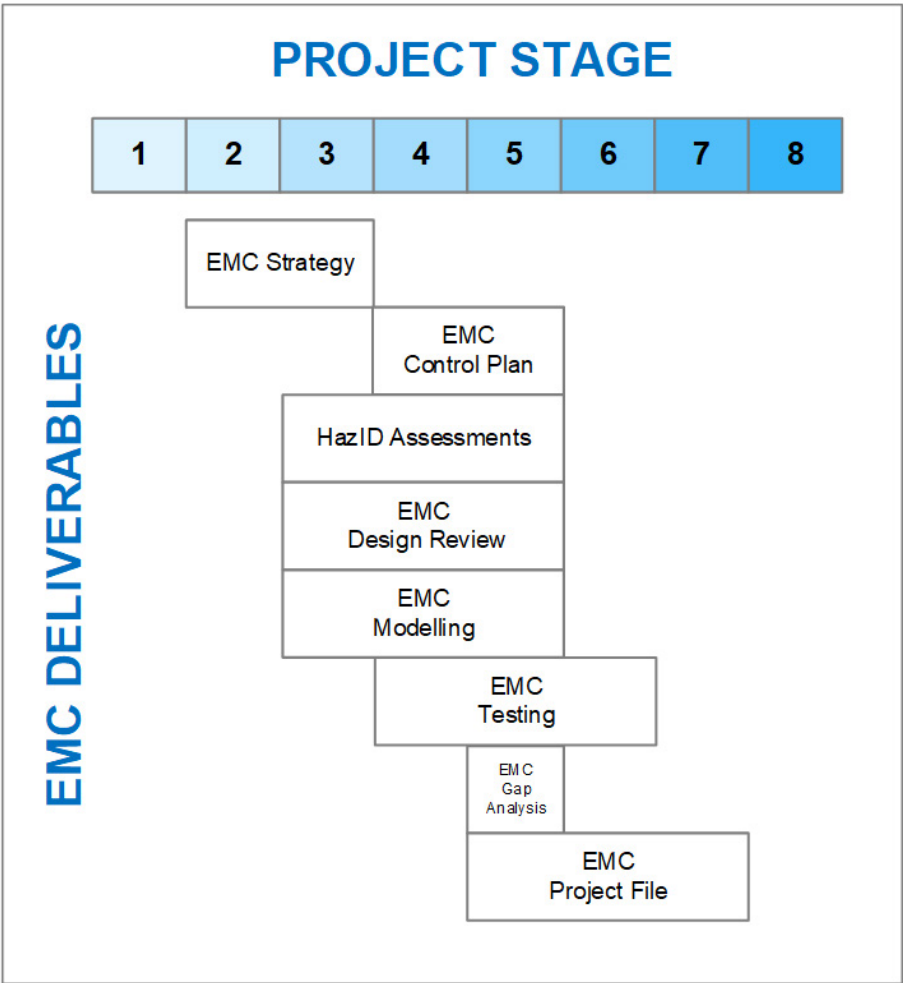
## 4. Deliverables

Irrespective of the agreed method of project management and delivery, there exists a need to develop a suite of formal documentation and assurance activities which ultimately govern the level of EMC evidence required for any project. As noted in Section 2, the compilation of this documentation will provide the infrastructure manager with the confidence that EMC has been considered throughout all aspects of a project's lifecycle.

When considering how progressive EMC assurance is managed on NR projects, it is noted that their EMC Strategy and EMC Assurance Process have not yet been updated to include reference and applicability to PACE. The industry has therefore had to interpret how the existing methods of EMC assurance align with projects adopting the new PACE Engineering Stages. This generalisation has been highlighted in **Figure 2**; but it is noted that until this alignment has been formalised by NR, it may be subject to change.

FIGURE 2

Typical EMC Deliverables



Whilst Figure 2 shows the full suite of assurance that may be applied to a project, it is correctly noted that not all the deliverables may be required to provide sufficient levels of EMC evidence. During mobilisation, the level of significance of any project with respect to EMC shall be agreed upon. This level of significance is based on several key project criteria, including (but not limited to); the anticipated complexity, if the installation is considered standard or novel (as per Section 12 of NR/L2/RSE/30041 [6]), the overall perceived level of risk as well as the agreed Level of Control (LoC) on NR projects employing PACE. By adopting a proportionate and practical approach to EMC assurance, projects can see significant benefits; including improvements to programme delivery, reduced costs and a decrease in errors that may be introduced by overcomplication.

The following subsections outline the key EMC assurance activities. On completion, each activity provides the project with specific assurance information which will contribute to the overall package of evidence that can be used by the project.

#### 4.1. EMC STRATEGY

An EMC Strategy identifies and defines the various assurance processes necessary for the project to evidence suitable compliance against the relevant product and company standards, as well as to legal obligations within the EMC Regulations S.I. No. 2016/1091 [11].

As a minimum, the EMC Strategy shall be developed to include the following information applicable to a project:

- › Defining the overall installation as well as any project and/or work package specific requirements;
- › Identifying applicable design standards and legislation;
- › Defining EMC responsibilities and activities to be co-ordinated between individual disciplines as well as other third-party entities throughout the project life cycle; and,
- › Defining how EMC risk assessments and multi-disciplinary hazard identification shall be co-ordinated and carried out during subsequent GRIP Stages.



#### 4.2. EMC CONTROL PLAN

The development and scope of an EMC Control Plan is dictated by the complexity of the overall project; one is required where novel equipment or non-standard installations form part of the design (as per NR/L2/RSE/30041 [6]), or where the project may be categorised as medium risk or above (as per NR/CRT/M2/EP/06 [15]).

The aim of the Control Plan is to build and enhance the information presented within the Strategy. This may include providing additional details on EMC hazard management and mitigation, as well as the identification and provision of discipline specific design requirements.

The Control Plan is typically updated as required throughout the remaining design phases of a project lifecycle.

#### 4.3. HAZARD IDENTIFICATION

EU regulation 402/2013 [16] on the “adoption of a common safety method on risk evaluation and assessment” (referred to as the ‘CSM’), sets out a risk management process that applies to all significant technical, organisational and operational changes which may impact on the operating conditions of the railway system.

The CSM framework describes a common mandatory European risk management process for the rail industry and does not advise specific tools or techniques to be used. In addition, CSM is only applied to mainline rail projects and has not been adopted by other metro or light rail systems; like for example, London Underground. The framework of the CSM is based on the analysis and evaluation of hazards using one or more of the following risk acceptance principles:

- › Application of codes of practice;
- › Comparison with reference systems; and/or,
- › Explicit risk estimation.

A HazID workshop serves to identify risks associated with systems or actions (either planned or unplanned) that fall within the whole life cycle of the project; including the scope of design, construction or operation of the project. In doing so, the HazID will generate project-specific requirements for consideration and management.

For any identified hazards, effective mitigation measures shall be decided upon such that they can be eliminated by way of design changes or mitigated to levels deemed acceptable and managed. The identified hazards and associated mitigation strategies shall then be cascaded to the relevant design teams to aid in the development of the designs, and ensure they meet all requirements.

#### **4.4. DESIGN REVIEWS**

Design Reviews ensure that EMC has been managed and controlled correctly by all stakeholders, disciplines and responsible parties throughout the course of the design. This method of progressive assurance ensures that everyone is aware of their responsibilities and can help the project to appraise ongoing designs; by allowing for comments, recommendations and mitigations related to EMC to be captured and actioned as required.

Design reviews may be managed by way of informal discipline coordination, or through more formalised channels; for example, as part of project stage Interdisciplinary Reviews/Check activities.

#### **4.5. GAP ANALYSIS**

An EMC Gap Analysis (sometimes termed a Qualification Assessment) is an activity which looks to formally assess and verify the compliance of each individual piece of equipment being installed on the project against the relevant EMC standards and requirements.

The assessment and approval of each component is made via the review of several pieces of documentation and design information; including (but not limited to) manufacturer(s) Declaration(s) of Conformity, product datasheets and available test documentation, as well as consideration for the location of the installed equipment in the network and any interfacing systems.

Where information is unavailable, further investigations and design reviews may be required to provide the necessary qualification and technical justifications for a particular piece of equipment to be safely used within the project. Ultimately, if an assessment determines that a piece of equipment is non-compliant, then steps can be implemented by the EMC design team to ensure a suitable alternative is identified or mitigation measures are agreed and implemented.





#### **4.6. EMC PROJECT FILE**

At the end of the design stage, an EMC Project File (or Technical Assurance File) is developed. This document provides the project with formal evidence that the approved, construction-ready design complies with all the applicable statutory, group and company EMC standards.

The EMC Project File itself can be considered as an amalgamation of the previous EMC assurance activities, and will collate information from the Design Reviews, Gap Analysis and HazID activities, as well as any modelling results (if available), equipment assurance evidence (certificates/test reports etc.) and the output of any EMC studies undertaken. Also captured in the Project File is the EMC Statement of Conformity; a declaration by the EMC assurance team that will ultimately support the Project Completion Certificate by demonstrating that EMC has been achieved, any outstanding actions or maintenance requirements are clearly communicated, and that all associated hazards have been eliminated or mitigated to agreed levels of risk so far as is reasonably practicable.

#### **4.7. TEST SPECIFICATIONS**

There are several EMC specific tests which may be mandated or proposed throughout the design lifecycle. The level of testing must be proportional to the complexity of the project as well as any identified hazards. Testing may include undertaking baseline radiated emissions measurements (in line with BS EN 50121-2) to determine the ambient electromagnetic field and allow for comparisons to identify what (if any) impact the project has had on the existing environment. Additionally, longitudinal and transverse voltage testing (known as  $V_L/V_T$  tests) is something that forms part of common suite of tests for the commissioning of signalling and telecommunication systems.

These types of tests become increasingly important for major electrification projects when considering the effects of energised overhead line equipment and high voltage distribution networks in the vicinity of sensitive and third-party systems, as well as their potential impact on human health and safety.

#### **4.8. MODELLING AND SIMULATION**

Modelling plays an important role in achieving EMC assurance and helping designers in choosing the most appropriate option according to EMC standards and requirements. Modelling (and subsequent qualification) may be conducted throughout a project, but typically it is completed early in the design lifecycle.

The processes and activities associated with EMC Modelling are discussed in further detail within Section 5.

## 5. Modelling on Major Railway Projects

---

In the past decades, railway systems and their subsystems have become more complex. Due to the emerging complexity of power supplies, signalling, timetable and operation in railway networks, carrying out a further analysis of different characteristics of the network has played a key role in rail market. Electrification system simulation is an essential aspect of the design of an energy efficient, reliable and safe railway system. Modelling increases adaptability and enhancements remarkably through the project life cycle, from design stage to validation, verification (V&V) and commissioning. Some of the key characteristics of rail systems, where modelling can be used to provide an assessment of are touch and induced voltages, magnetic fields, harmonics distortion, personnel safety (EMF), equipment compatibility and EMC [17].

There are a wide range of modelling tools available to evaluate EMC in railway networks; however most do not provide a complete package requiring multiple models to be constructed. Atkins has developed their own bespoke software, known as the Atkins Traction Modelling Simulator (ATMS) to provide EMC analysis by postprocessing traction power load flow simulations.

ATMS originally started development back in April 2020. Used to support smaller and simpler projects (for example, only having one feeding section and two track), the advancement of ATMS was principally driven by adapting the software to manage the modelling requirements of major rail electrification projects – including High Speed 2 (HS2). The system was required to incorporate a significant increase in architecture – in the case of HS2, this included four feeding stations, various traction power and overhead line configurations, and also the assessment of several internal and external interfaces. Tunnelled sections, viaducts, stations, as well as adjacent rail and non-rail interfaces; including East West Rail, or the proposed telecommunications systems as part of the M6 Motorway upgrade, all needed to be modelled in some form.

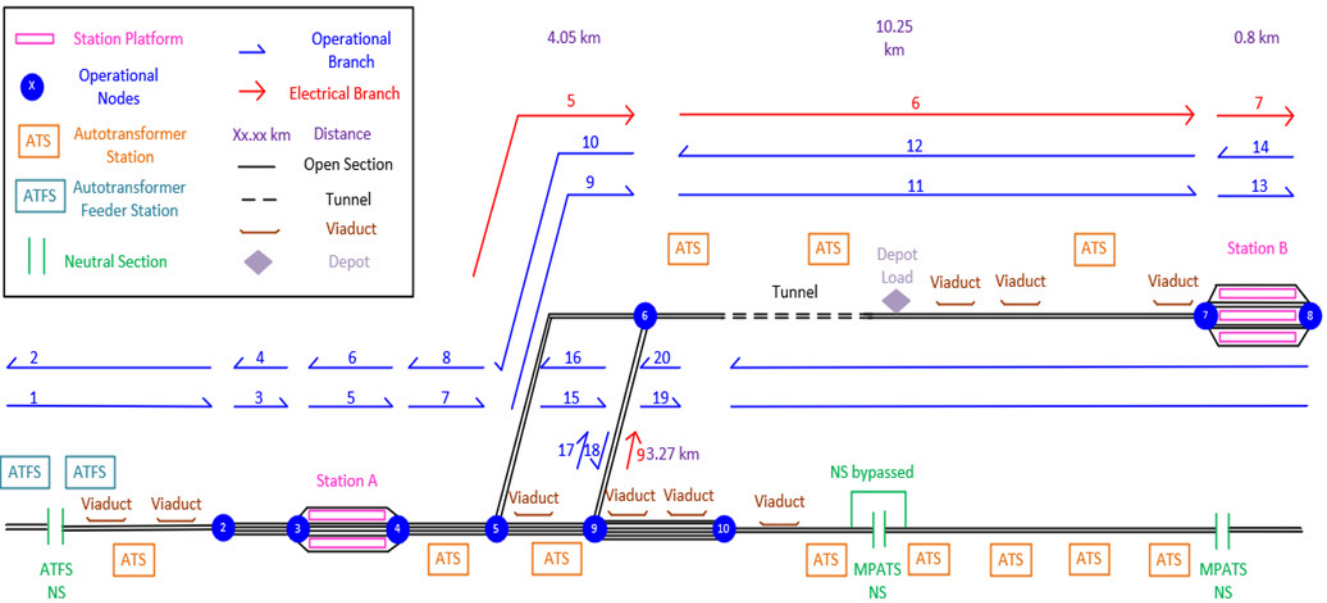
In addition to HS2, the software has since been deployed and developed on a wide variety of different project types – including 25kV mainline electrification, 1500V DC overhead metro systems (proving existing infrastructure has sufficient immunity when assess against new rolling stock being deployed), and also overseas rail projects (assessing the traction power loading requirements as part of a project wide upgrade to an existing metro system).

When considering the benefits of ATMS over its competitors, as the models are built using MATLAB code, this provides significant improvements in the ease and flexibility to modify or develop the model as required, subject to a rigorous source control and Validation and Verification process. These modifications are typically based on criteria such as emerging project scope or client requirements, and the MATLAB functionality helps streamline efficiencies in delivery. The software also combines the functionality of several existing industry wide applications (for example, Network Rail's VisionOSLO, ELSSA and FREDs tools) into one integrated package. This provides a modern single-build digital twin approach to electrification system modelling. ATMS can run several different post processing studies for project specific EMC and E&B information; see **Figure 4** for more information.

**Figure 3** shows an indicative schematic of a system model using ATMS.

**FIGURE 3**

Part of an example system  
model schematic




This tool, which is implemented in MATLAB, includes modelling and analytical procedures conforming to Euronorms and BSI standards as well as the Energy and Rolling Stock Technical Specifications for Interoperability (TSIs). ATMS can be applied to complex railway infrastructures that incorporate multiple tracks, routes and branches with different characteristics.

The key features of the ATMS are:

- › Modelling of both DC and AC systems, including DC/AC co-simulation of the HV network of DC systems;
- › Power system architectures including feeder station grid connections, autotransformers, booster transformers, static frequency converters, static loads and other onboard and lineside power equipment;
- › Arbitrary longitudinal conductors, line cross-sectional geometries including system earthing and bonding designs;
- › Generic rolling stock models or characteristic curves provided by the manufacturers including mixed mode operation;
- › Dynamic load according to simple headways or detailed operator provided timetables; and,
- › Analysis of discontinuous electrification supplemented by onboard energy storage solutions.

ATMS is continually developed and currently has the capabilities listed below:

- › Load-flow analysis of the traction power supply including transformer and cable ratings, energy consumption, mean useful voltage and train performance (BS EN 50641, BS EN 50388);
- › EMC assessment of the traction power supply with signalling, telecoms and third-party communication systems (EMC Regulations, BS EN 50121);
- › Touch voltages in both normal and short circuit (fault) conditions for railway and third-party infrastructure including rail to local earth voltage, induced cable screen voltages and transferred voltages according to ground conditions (BS EN 50122-1);
- › Transient assessments, including swept short circuit fault current, inrush current, and direct lightning strikes;

- 
- › Electric and magnetic field calculations for human exposure compliance assessment (Control of Electromagnetic Fields at Work Regulations, GL/GN1620, ICNIRP);
  - › Harmonics distortion assessment, including resonance and harmonic current penetration in the high voltage grid, and compliance with (BS EN 50388, ENA G5/5); and,
  - › Systems impedances and protection calculations.

This tool has been applied to different AC and DC projects to carry out detailed EMC assurance analysis. Key projects both past and present where ATMS has been adopted include:

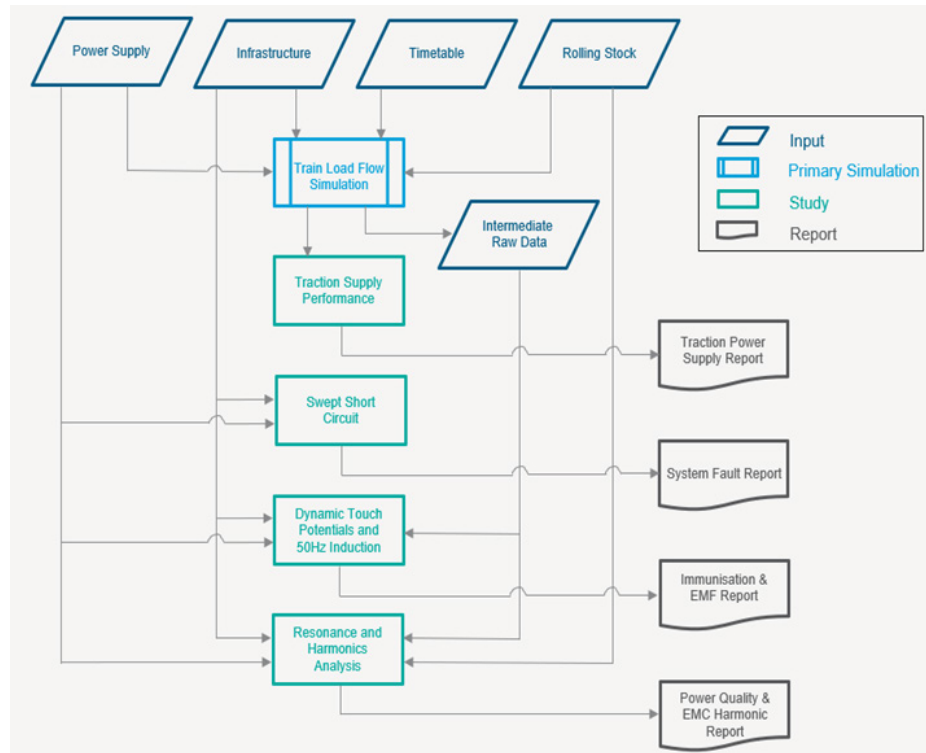
- › High Speed 2 – United Kingdom
- › Regional Express Rail – Canada
- › Wigan to Bolton – United Kingdom
- › Tyne and Wear Metro – United Kingdom

**Figure 4** indicates the structure of the ATMS, including required inputs, primary simulations, studies and produced reports. The input data includes four subsystems: Power Supply, Infrastructure, Timetable and Rolling Stock. After a primary train load flow simulation, ATMS is able to carry out four different studies and produce reports for each of them. The studies are Traction Supply Performance leading to the production of Traction Power Support Report. The next study is Swept Short Circuit analysis from which System Fault Report can be achieved, Dynamic Touch Potential and 50Hz Induction is another study to analyse immunisation and EMF, and the last study is Resonance and Harmonics Analysis, where Power Quality and EMC Harmonic assessment can be obtained.



FIGURE 4

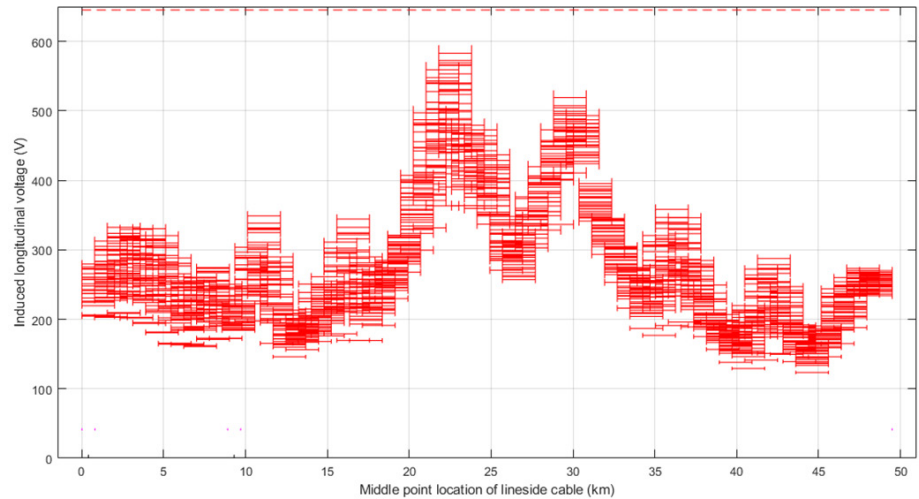
Structure of the ATMS



1. **Traction Supply Performance:** This study demonstrates whether the proposed supply can meet the train demand and analyses load flow of the traction power supply including transformer and cable ratings, energy consumption, mean useful voltage and train performance.
2. **Swept Short Circuit:** In this study, a zero impedance short-circuit (fault) is imposed between the contact wire and traction return system and swept along the whole alignment. This study evaluates the touch and induced voltages on all conductors in different parts of the railway network. **Figure 5** indicates one of the main results achieved from this study, which is the 50Hz longitudinal voltage induced on CCS and Telecoms cables under short circuits condition. From the Option Selection Stage to the Detailed Design Stage, this part of the Swept Short Circuits Study results gives designers the opportunity to determine the most optimal location and the maximum allowed length of any lineside cable under fault, to maintain personnel safety and safe operation of the trains [17], [18].

FIGURE 5

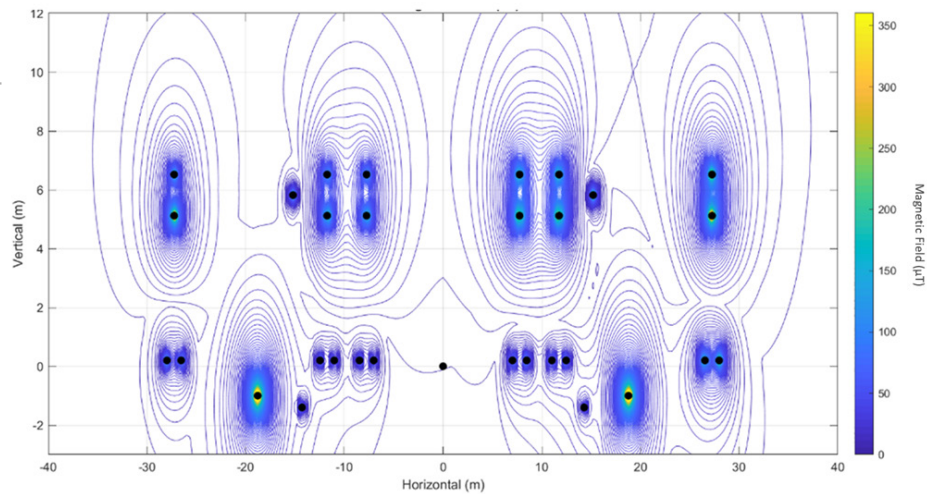
Induced longitudinal voltage on CCS and Telecoms cables under short circuit condition



3. **Dynamic Touch Potential and 50Hz Induction:** The power frequency (50Hz) load flow simulation of track operations is performed in this study to understand touch and induced voltages on conductors as well as magnetic and electric fields in different parts of the railway network. In **Figure 6**, the maximum magnetic field for all conductors can be seen at a station. This result helps to figure out the EMF exposed to trackside equipment and public and it forms EMC requirements to protect them. The same as the Short Circuits Study, the Dynamics Study can be used from Option Selection Stage to the Detailed Design Stage.

FIGURE 6

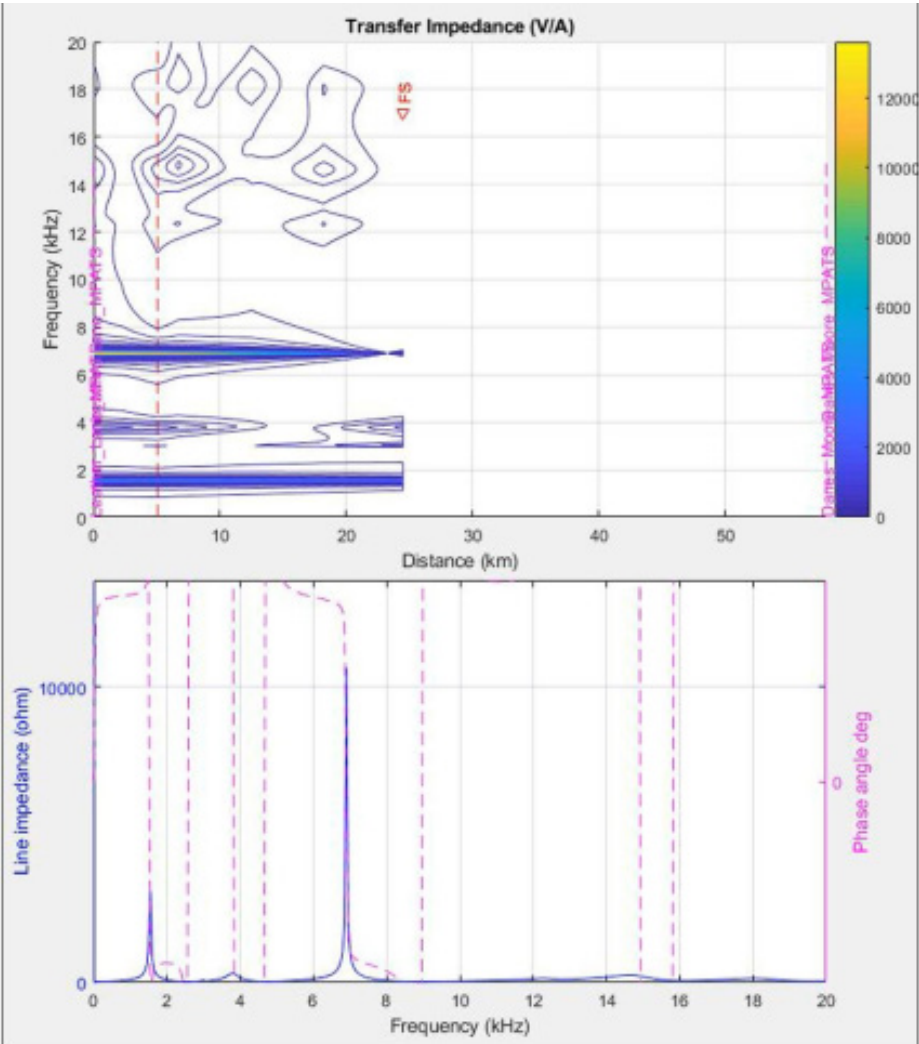
Maximum magnetic field at mid platform longitudinal distance of a station



4. **Resonance and Harmonics Analysis:** The harmonics transfer impedance of the power supply and the harmonic currents produced by the trains are calculated in this study to quantify the effects of harmonic distortion. This study analyses Rolling Stock emissions and predicts the interference levels on lineside cables and equipment as well as parallel running railways to assess whether the touch potential and EMI are within acceptable limits. Employing this study leads to forming the immunisation of the system [17], [18]. Harmonic transfer impedance produced by the train is shown in **Figure 7**.

FIGURE 7

Harmonic transfer impedance produced by the train





## **6. Conclusion**

---

Progressive EMC assurance is vital to the successful design, construction and operation of any major rail infrastructure project. Whilst the fundamental processes and project activities may seem cumbersome, the level of effort required by all parties can be carefully managed and simplified through early engagement, effective coordination and the adoption of a robust assurance methodology.

Recent advances in modelling and simulation tools; specifically with the use of ATMS, can provide projects with the necessary EMC evidence and requirements to implement a safe, compliant and reliable railway system.

## **Acknowledgements**

---

This paper was first presented at the EMC & Compliance International Symposium, Newbury, UK, May 2022.





## References

---

1. EMC Directive 89/336/EEC
2. SI 1992/2372 – UK EMC Regulations
3. 2004/108/EC – European Union Directive on EMC
4. SI 2006/3418 – The Electromagnetic Compatibility Regulations 2006
5. NR/L1/RSE/30040 – EMC Strategy for Network Rail
6. NR/L2/RSE/30041 – Electromagnetic Compatibility Assurance Process
7. LUL S1222 – Electromagnetic Compatibility (EMC)
8. LUL G222 – EMC Best Practice
9. DLR-ENG-STD-ES102 – Engineering EMC
10. 2014/30/EU – European Union Directive on EMC
11. SI 2016/1091 – The Electromagnetic Compatibility Regulations 2016
12. NR NR/L1/INI/PM/GRIP/100 ISSUE 1 - Governance for Railway Investment Projects (GRIP) - Policy Manual - Compliance Date: 5 March 2011
13. NR/L2/P3M/201 – Project Acceleration in a Controlled Environment (PACE)
14. RIBA Plan of Work Overview. 2020.
15. [NR/CRT/M2/EP/06 – Network Rail Contract Requirements – Electromagnetic Compatibility
16. EU Reg. 402/2013 – EU Regulation on the Common Safety Method for Risk Evaluation and Assessment
17. R. Kadhim, P. Fayat and R. R. Hamed, Integrated Approach for Compatibility Assessment Between Traction Power Supply and Rolling Stock, 8<sup>th</sup> International Conference on Railway Engineering (ICRE 2018), London: 16-17 May 2018
18. R. D. White, Electrification Traction and Signalling Compatibility, the 11<sup>th</sup> IET Professional Development Course on Railway Signalling and Control Systems, London: 5-9 June 2006.



**SNC • LAVALIN**

   [snclavalin.com](http://snclavalin.com)

**Contact Information**

Dorothy Gartner  
Librarian, Knowledge Management  
[dorothy.gartner@snclavalin.com](mailto:dorothy.gartner@snclavalin.com)

© SNC-Lavalin except where stated otherwise

